

Spring 2000

Multipoint measurements of large electric fields and shears in the Auroral zone

David Pietrowski

University of New Hampshire, Durham

Follow this and additional works at: <https://scholars.unh.edu/dissertation>

Recommended Citation

Pietrowski, David, "Multipoint measurements of large electric fields and shears in the Auroral zone" (2000). *Doctoral Dissertations*. 2126.

<https://scholars.unh.edu/dissertation/2126>

This Dissertation is brought to you for free and open access by the Student Scholarship at University of New Hampshire Scholars' Repository. It has been accepted for inclusion in Doctoral Dissertations by an authorized administrator of University of New Hampshire Scholars' Repository. For more information, please contact nicole.hentz@unh.edu.

INFORMATION TO USERS

This manuscript has been reproduced from the microfilm master. UMI films the text directly from the original or copy submitted. Thus, some thesis and dissertation copies are in typewriter face, while others may be from any type of computer printer.

The quality of this reproduction is dependent upon the quality of the copy submitted. Broken or indistinct print, colored or poor quality illustrations and photographs, print bleedthrough, substandard margins, and improper alignment can adversely affect reproduction.

In the unlikely event that the author did not send UMI a complete manuscript and there are missing pages, these will be noted. Also, if unauthorized copyright material had to be removed, a note will indicate the deletion.

Oversize materials (e.g., maps, drawings, charts) are reproduced by sectioning the original, beginning at the upper left-hand corner and continuing from left to right in equal sections with small overlaps.

Photographs included in the original manuscript have been reproduced xerographically in this copy. Higher quality 6" x 9" black and white photographic prints are available for any photographs or illustrations appearing in this copy for an additional charge. Contact UMI directly to order.

**Bell & Howell Information and Learning
300 North Zeeb Road, Ann Arbor, MI 48106-1346 USA
800-521-0600**

UMI[®]

**Multipoint Measurements of Large Electric Fields and
Shears in the Auroral Zone**

BY

David Pietrowski

(B.S.), Rochester Institute of Technology (1994)
(M.S.), University of New Hampshire (1997)

DISSERTATION

Submitted to the University of New Hampshire
in partial fulfillment of
the requirements for the degree of

Doctor of Philosophy

in

Physics

May 2000

UMI Number: 9969211

**Copyright 2000 by
Pietrowski, David**

All rights reserved.

UMI[®]

UMI Microform 9969211

Copyright 2000 by Bell & Howell Information and Learning Company.

**All rights reserved. This microform edition is protected against
unauthorized copying under Title 17, United States Code.**

**Bell & Howell Information and Learning Company
300 North Zeeb Road
P.O. Box 1346
Ann Arbor, MI 48106-1346**

ALL RIGHTS RESERVED

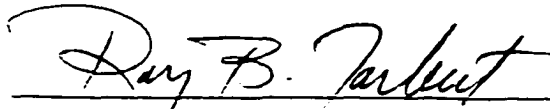
©2000

David Pietrowski

This dissertation has been examined and approved.



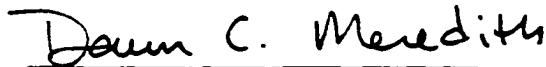
Dissertation Director, Kristina A. Lynch
Research Associate Professor of Physics and Earth,
Oceans, and Space



Roy B. Torbert
Professor of Physics and Earth, Oceans, and Space



Roger L. Arnoldy
Professor of Physics and Earth, Oceans, and Space



Dawn C. Meredith
Associate Professor of Physics



Michael C. Kelley
Professor of Electrical Engineering
Cornell University

4/21/2000

Date

Dedication

*To my family for showing me the path and to my wife
for following it with me.*

Acknowledgments

I would like to take this opportunity to thank my advisor, Kristina Lynch, for not only guiding me along throughout my work, but making me a better rocket scientist, a better researcher, a better teacher, and a better person in the process. Without her as my advisor, not only would I have not finished in the time that I did, but I would have missed having one of the best advisors on this campus, and for that I will be forever grateful. I would also like to thank the members of my thesis committee, Roger Arnoldy, Mike Kelley, Dawn Meredith, and Roy Torbert who have helped me to forge this lengthy work and whose enthusiasm for science have helped me stay motivated.

I also extend sincere appreciation to everyone who helped in making the Auroral Turbulence II launch a success. John Levasseur, Art Anderson, and Phil DeMaine produced fantastic pieces in the machine shop, and their skill once again helped to ensure the success of the mission. Eric Dors made calibrating the detectors a painless experience, albeit a late night one. John Googins did a great job with the electronics, and Steve Longworth not only did wonders with the correlator, but told me about the many wonders of Portugal. I would like to especially thank David Rau for not only his expertise and patience while allowing a green kid to help build a rocket payload, but for the rest of the “knowledge” that we have found along the way.

In completing this thesis, I had tremendous help from Mark Chutter, who helped me with countless computer problems. Pete Schuck, Bill Amatucci, and Joe Peñano really helped me understand shears and the IEDDI process. I also would like to thank Lynette Gelinis for her aid with IDL, LaTeX, and turning me on to falafels and Irish pubs. Cristian Cochei and Brett Austin have not only been great colleagues and helped me with so much,

but have also been great friends, even if they make fun of my golf game.

To list all of my other colleagues and friends would not only take up too much room, but might bore the reader, so I thank them all with a broad stroke. However, I would like to specifically thank my friends in the incoming graduate class of 1995 : Trisha Tynan, Chris Siren, Crystle Zanes, Joel Shaw, and especially Kriss Hunold. We all came in together, struggled together, and even though many of us have gone in different directions, I still feel like we're in this together, and I am glad to have finished my dissertation with your help. I never will underestimate the power of the friendship we all have.

Finally, I would like to thank my family. I almost feel this is the hardest thing to write, since it will look so insignificant in comparison to all you have done for me. I only want my parents, Joseph and Mary Lou, and my sister, Elizabeth, to know that no matter how proud they are of me, I am probably more proud of them. And to my best friend, greatest supporter, and wife, Michelle, I hope someday you can realize how much of this thesis you are a part of, and how fortunate I have been to have had you with me throughout this entire process. Lastly, I thank you, the reader, for allowing me the time to share with you my work, or at least for politely suffering through it.

TABLE OF CONTENTS

Dedication	iv
Acknowledgments	v
List of Tables	ix
List of Figures	xii
Abstract	xiii
1 Introduction	1
1.1 Ionospheric Processes	2
1.1.1 The Aurora and Particle Precipitation	2
1.1.2 DC Electric Fields	5
1.1.3 Ionospheric Shears, Dynamics, and Inhomogeneities	9
1.2 Motivation for Auroral Turbulence II	12
1.3 Thesis Statement	13
2 Auroral Turbulence II Instrumentation	15
2.1 Particle Detectors	15
2.2 Magnetometers and Other Instrumentation	17
2.3 Electric Field Experiment	18
2.3.1 Preparation	18
2.3.2 Calibration and Extraction of Data	20
3 Data Presentation	21
3.1 Auroral Environment	21
3.1.1 Ground Based Imagery	21
3.1.2 Ground Based Magnetometer Data	25
3.1.3 WIND, GOES, and POLAR Data	31
3.2 Launch Details	34
3.2.1 Launch Specifics	34
3.2.2 Payload Trajectory	36
3.2.3 Vehicle and Instrument Performance	39
3.3 Measurements	41
3.3.1 Particle Data	41
3.3.2 HF Data	46
3.3.3 Magnetometer Data	47
3.3.4 Electric Field Data	48
3.3.5 LF Wave Data	59
4 Science Discussion	64
4.1 Implication of Electric Field Magnitudes	64
4.2 Temporal and Spatial Considerations	74
4.3 Electric Field Shear and Waves	86
4.3.1 Brief Description of the IEDD mechanism	87

4.3.2	AT II Electrostatic Wave Observations and Discussion	89
5	Conclusions	106
	Bibliography	109
	Appendices	116
A	Electric Field Despinning and Rotation	117
A.1	Raw Data	117
A.2	Gains, Offsets, and Despinning	118
A.2.1	Gains and Offsets	118
A.2.2	Despinning	120
A.3	Rotation Into Specified Coordinate Systems	121
B	Payload Shadow Model	126
B.1	Model Framework	126
B.2	Model Approximations	129
B.3	Model Results	133
C	Number Density Calculations	141
C.1	Calculation of Number Density	141
C.2	Estimated Densities	142

List of Tables

A.1	Components of $\frac{\vec{L}}{L}$ for subpayloads	123
B.1	Payload Dimensions.	129
B.2	Integration Limits.	130
B.3	Maximum Electric Potential Difference as a Function of Shadow Dimensions (mV/m) with $n = 5 \times 10^6$ for the North Payload.	131
C.1	Portion of the number density measured as a function of peak beam energy for particle detectors.	143

List of Figures

1-1	View of the Earth, sunward convection flow, and resulting perpendicular electric fields and parallel currents (as from <i>Kelley, [1989]</i>).	3
2-1	AT II Payload Diagrams.	16
2-2	Electric field experiment hardware schematic.	19
3-1	All-sky image from Kaktovik during the flight (T+365 seconds). The bright dot in the image is an enhanced pixel representing the location of the three payloads.	22
3-2	Poker Flat meridional scanning photometer data from February 11, 1997 (courtesy Poker Flat Research Range). Each panel is a different atomic spectral line emission with a color bar brightness index.	24
3-3	Poker Flat three axis magnetometer data (courtesy PFRR).	25
3-4	Map of CANOPUS chain magnetometers (courtesy Canadian Space Agency).	27
3-5	Stack plot of x-component magnetometer chain data (courtesy CSA).	28
3-6	Stack plot of y-component magnetometer chain data (courtesy CSA).	29
3-7	Stack plot of z-component magnetometer chain data (courtesy CSA).	30
3-8	WIND solar proton monitor data from February, 1997 (courtesy University of Maryland).	32
3-9	GOES-8 magnetometer data (courtesy NOAA/NGDC).	33
3-10	Composite of POLAR Ultraviolet Imager during AT II launch (courtesy MSFC/NASA/M. Brittnacher, UW).	35
3-11	AT II Main payload geographic footprint trajectory.	36
3-12	AT II payload trajectories.	37
3-13	AT II payload orientation.	38
3-14	Survey plot of East payload electron data.	42
3-15	Survey plot of Main payload HF data (from [<i>McAdams, et al., 1997</i>]).	42
3-16	Survey plot of dc electric field from the North payload.	42
3-17	North and East payload electron data from T+300 seconds to T+355 seconds.	44
3-18	North and East payload electron data from T+355 seconds to T+410 seconds.	45
3-19	Magnetometer data during the dispersed electron event (from <i>Ivchenko, et al., [1999]</i>).	47
3-20	Northward component of the Main payload electric field.	50
3-21	Components of the North (black) and East (red) payload electric fields.	50
3-22	Northward electric field component of the subpayloads from T+200 to T+600 seconds (North - black, East - red).	52
3-23	Westward electric field component of the subpayloads from T+200 to T+600 seconds (North - black, East - red).	53
3-24	Arc aligned electric field components of the subpayloads (North - black, East - red).	55
3-25	Electron spectrogram from the North payload.	55
3-26	Oscillations in the magnetometer data (from <i>Ivchenko, et al., [1999]</i>).	57

3-27	Oscillations in the electric field data and the calculated Poynting flux from $\delta\vec{E} \times \delta\vec{B}$	57
3-28	Arc aligned electric field components of the subpayloads (North - black, East - red).	58
3-29	Survey plot of low frequency data from the North payload.	61
3-30	Survey plot of low frequency data from the East payload.	61
3-31	Plot of low frequency data from the North payload.	62
3-32	Plot of low frequency data from the East payload.	62
3-33	Average wave intensity from T+385 to T+386 from the East payload.	63
4-1	Inferred conductivities from electron precipitation.	68
4-2	Calculated field aligned current from East payload data.	69
4-3	Possible potential lines during arc crossing. Geographic north is to the left of the figure, altitude increases vertically.	73
4-4	Correlation between the North and East Payload dc electric fields from T+368 to T+385 seconds.	77
4-5	Correlation between the North and East Payload dc electric fields from T+385 to T+392 seconds.	77
4-6	Northward electric field from the Main payload.	78
4-7	Arc aligned electric field components of the subpayloads (North - black, East - red).	78
4-8	Possible scenario of a region of high electric field moving along the arc. The grey region represents a region of low electric field, the pink region is a region of fast plasma flow.	80
4-9	Modeled electric field measurement of three payloads moving northward as a region of fast moving plasma moves westward, followed by a temporal decrease in the plasma velocity. The North payload is in black, the East in red, and the Main in Blue, as in Figure 4-8.	80
4-10	Digitized all-sky images for successive flight times during the main arc fly-through.	83
4-11	Dispersion surfaces from the WHAMP code. Note that each panel has a different vertical scale. Some frequency values have been superimposed on each plot for identification.	92
4-12	Dc electric arc-normal fields (top panel) from the North (blue) and East (red) payloads and the dc shear (bottom panel) calculated from the top panel.	94
4-13	Top panel: dc electric arc-normal fields from the North (black) and East (red) payloads. The North panel has been normalized to the East payload. Middle panel: recalculated shear using the normalized data set. Bottom panel: dc shear calculated from the arc-normal spatial derivative of the East payload.	96
4-14	Top panel: North and East dc electric fields. Bottom panel: Correlation between East payload dc electric field and the North payload electric field from T+372 to T+397 seconds.	98
4-15	Top panel: North payload wave power at 42 Hz and 680 Hz. Bottom panel: Correlation between wave power at 42 Hz and at 680 Hz on the North payload from T+372 to T+397 seconds.	99

4-16	Top panel: East payload wave power at 42 Hz and 680 Hz. Bottom panel: Correlation between wave power at 42 Hz and at 680 Hz on the East payload from T+372 to T+397 seconds.	99
4-17	Top panel: North and East payload electric field wave power at 42 Hz. Bottom panel: Correlation between wave power at 42 Hz on the East payload and wave power at 42 Hz on the North payload from T+372 to T+397 seconds.	101
4-18	Top panel: dc electric field shear and East payload electric field wave power at 42 Hz. Bottom panel: Correlation between dc shear and the East payload wave power at 42 Hz from T+372 to T+397 seconds.	101
4-19	Top panel: North payload dc electric field and East payload electric field wave power at 42 Hz. Bottom panel: Correlation between the North dc electric field and the East wave power at 42 Hz from T+372 to T+397 seconds.	102
4-20	Top panel: East payload dc electric field and East payload electric field wave power at 42 Hz. Bottom panel: Correlation between the East dc electric field and the East wave power at 42 Hz from T+372 to T+397 seconds.	102
A-1	The \vec{B} , \vec{L} , $\vec{\omega}$, spherical triangle.	120
B-1	Schematic of the payload and shadow. The magnetic field is parallel to the x-axis in the figure.	127
B-2	Potential difference resulting from shadow region as would measured by the North payload.	134
B-3	Potential difference resulting from shadow region as would measured by the East payload.	134
B-4	Potential difference of North payload shadow region. The dashed line shows a perfect sinusoidal signal.	135
B-5	Potential difference of East payload shadow region. The dashed line shows a perfect sinusoidal signal.	135
B-6	Addition of shadow potential with the equal magnitude potential due to an ambient electric field with a phase of (a) 0° , (b) 45° , (c) 90° , (d) 140° , (e) 225° .	137
B-7	Raw electric potential difference as a function of flight time for the North payload.	139
B-8	Raw electric potential difference as a function of flight time for the East payload.	139

ABSTRACT

Multipoint Measurements of Large Electric Fields and Shears in the Auroral Zone

by

David Pietrowski
University of New Hampshire, May, 2000

This work presents results from the Auroral Turbulence II (AT II) sounding rocket launched from the Poker Flat Research Range, near Fairbanks, Alaska, on February 11, 1997. The rocket consisted of three identically instrumented payloads that reached an apogee of 550 km and flew through several arc structures in a pre-midnight auroral breakup. Three payload measurements were desired to separate the temporal from spatial aspects of auroral forms, and to investigate three dimensional flows and fields that cannot be resolved using traditional single point measurements. The focus of this study has been in the structure and changes in the dc electric field.

Although the AT II payloads traversed many auroral arc structures, most of the forms had negligible electric fields associated with them. The one exception was when the payloads crossed a large, stable arc at nearly 500 km altitude. In the middle region of the arc, and near the poleward boundary, the payloads measured significant electric fields, as much as 450 mV/m in the poleward region of the arc. The payloads also measured different electric field structures, while approximately three kilometers apart, indicating a gradient in the field between measurements. Spectral analysis of the ac electric field data show broadband electrostatic waves in the regions of enhanced dc electric field.

The multiple measurements indicate a region of spatially localized electric field, electric

field shear and wave activity that both drifts in space and changes amplitude temporally. In-situ changes in the electric field are examined in parallel with all-sky imagery obtained near the footpoint of the payload trajectories. We have determined that there are errors in the dc electric field measurements that are most likely explained by a shadowing of the potential spheres by the payload. Despite the uncertainty in absolute magnitudes of the dc field, there are clear differences in the field signatures between payload measurements that can be shown to be spatial shears. The shear in the localized electric field, the observed broadband electrostatic waves, and the low field aligned currents measured by the magnetometers indicate an instability mechanism responsible for the wave growth. The most likely candidate, given the environment, is the inhomogeneous energy density driven instability (IEDDI), which we believe to be responsible for the observed electrostatic waves observed near the oxygen cyclotron frequency.

Chapter 1

Introduction

As young boys in central New York, my friends and I would play out in the yard all day and often well into the night. One night in particular, one of my friends peered into the horizon and saw a faint glow of light. He proceeded to tell me that it was the *aurora borealis*, but he had no idea what caused it. Years later, on a plane to Alaska for the Auroral Turbulence II rocket launch, I then knew the cause of the aurora, and thought I knew what to expect when I saw it up close. After two weeks in Fairbanks, I realized how a naive ten year old could mistake reflections of city lights from low clouds for the aurora if he had not seen the spectacular sights that I saw in Alaska. There were rays of shimmering curtains floating in the air with a soft whitish-green glow. One night a thin band of green oscillated back and forth like a plucked guitar string. Curls and folds danced in the sky almost nightly. It is truly a beautiful consequence of the Sun's interaction with the Earth, and there is little wonder why it continues to fascinate today's scientist as much as it did Aristotle in his work, *Metegorogika*.

While Aristotle described the aurora in term of the flames of a burning gas, scientists today have a much more technical description available to them, and have a good understanding of several basic auroral processes. The auroral environment is an excellent laboratory for studying the interaction of particles in a large scale plasma, and for better understanding the dynamic relationships between the planets, the Sun, and the plasma media in between. The use of balloons, rockets, and satellites in this laboratory have increased

our knowledge and also increased our questions. This dissertation is about one such rocket experiment and its attempt to resolve some of the newer questions about the aurora.

1.1 Ionospheric Processes

1.1.1 The Aurora and Particle Precipitation

We briefly outline the general physics behind particle precipitation and the creation of the aurora [Akasofu, 1981]. The visible aurora is produced by the collisions of energetic particles with the atoms in the lower ionosphere, near 100 to 200 km altitude. These particles within the near-Earth environment constitute some of the field aligned currents by which momentum is transferred. The compression of the Earth's magnetosphere by the supersonic solar wind creates an elongated magnetotail stretching tens of R_E antisunward. A schematic of the Earth's magnetic and electric environment, taken from Kelley, [1989], is shown in Figure 1-1. A cross-tail electric field, from dawn to dusk, results from a $\vec{v} \times \vec{B}$ drift of plasma sunward in the tail. This is often called the convection electric field since it is associated with a recognizable plasma flow pattern. The convection electric field in the magnetosphere maps down flux tubes into the conductive region of the ionosphere. The plasma flow in these flux tubes encounters no difficulty in moving sunward in the magnetosphere and outer ionosphere. However, at lower altitudes, neutral particles inhibit the plasma motion. In particular in the lower ionosphere, a current flows parallel to the convective electric field and here $\vec{J} \cdot \vec{E} > 0$. This indicates that the ionosphere acts as a load in the system and electrical energy is dissipated. The magnetospheric electric field generator is capable of supplying the energy to maintain the electric field in the conducting portion of

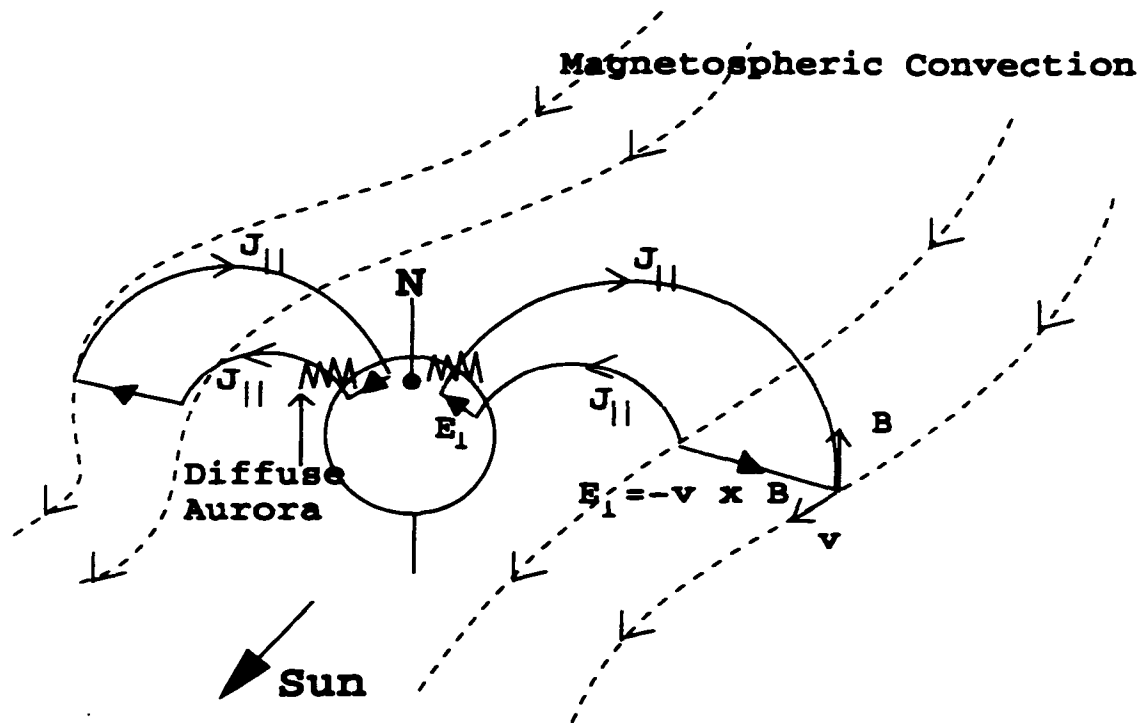


Figure 1-1: View of the Earth, sunward convection flow, and resulting perpendicular electric fields and parallel currents (as from Kelley, [1989]).

the ionosphere. The motion of plasma in the equatorial plane is itself driven by a $\vec{j} \times \vec{B}$ force that directs plasma Earthward. On the dusk side, the divergence of this current creates a field aligned current which enters the ionosphere at low latitudes and returns from higher latitudes to the equatorial plane. These currents, called the Region I and II currents, close the current between the magnetosphere and collisional ionosphere. During magnetic storms, these current systems are very well developed. The generation of field aligned currents can also occur in the tail region when the phenomenon called a substorm occurs which collapses the tail magnetic field and large field aligned currents flow to complete closure of the tail currents.

Field aligned currents are carried by both magnetospheric and ionospheric ions and

electrons [Birkeland, 1908, Carlson, et al., 1998a]. The energetic component of these currents is sometimes limited by the number of current carriers and the magnetic mirror force. created by the Earth's converging magnetic field near the poles, which prevents electrons from reaching the ionosphere and closing the current loop [Lysak, 1990]. This limitation is overridden by the creation of a potential structure parallel to the magnetic field that allows for the acceleration of particles to higher energies, and thus lower reflection heights [Evans, 1974, Chiu and Schultz, 1978, Chiu and Cornwall, 1980, Lyons, 1980]. Such parallel potentials are now known to accompany the most ubiquitous auroral form, the arc. There may be a host of processes that create this type of potential, including the "inverted-V" potential, which is characterized by a V-shape in the peak energy of the precipitating beam as an arc is traversed poleward [Swift, et al., 1976, Mozer, 1981].

The electrons that can reach low altitudes collide with atoms and molecules in the upper atmosphere. The excitation of the atoms/molecules results in a release of radiation in the visible, ultraviolet, and infrared regions. These light displays can show intricate complexity and motion. Entire arcs may move poleward or equatorward, while within the arcs there may flickering rays and swirling vortices. Often, electrostatic and electromagnetic waves are simultaneously detected in and near auroral forms. The causes of these motions, formations, and waves are at the root of many questions about the aurora and its behavior. In determining partial answers to these questions, efforts have focused on the role of dc electric fields.

1.1.2 DC Electric Fields

Dc electric fields are a critical element in determining auroral dynamics. We have already seen the role in electric fields in the transport of plasma from the tail and in closing the Region I and II currents. The presence of a parallel potential drop also shows the influence of electric fields in the acceleration of particles. The electric fields in the ionosphere and magnetosphere give us important information concerning the transport and acceleration of plasma, both parallel and perpendicular to the ambient magnetic field.

The importance of measuring auroral electric fields is complemented by the various ways which have been developed either to directly measure or to infer the dc electric fields [Mozer, 1973]. These methods include measuring the potential difference between two probes in-situ, observing plasma flows by tracking barium ions released into the ionosphere, using plasma drift meters on satellites, and by radar scattering techniques. A large electric field data set under numerous conditions now exists. These data can then be used to create a classification scheme based on the magnitude and direction of the electric field in and around auroral forms which can yield clues as to their generation mechanisms [Marklund, 1984]. This classification scheme is based on comparing the observed currents and electric fields to theoretical values based on different current closure requirements. When an insignificant Birkeland current is measured, there is no divergence of the perpendicular current in the highly conductive arc and a polarization electric field must set up across the arc. If the polarization field is much smaller than the observed field, then $\vec{\nabla} \cdot \vec{J} > 0$ and Birkeland currents have a strong role in the physics. The relation of the electric field to field aligned currents again shows the importance in determining electric fields in the ionosphere.

The dc electric fields in the outer magnetosphere may be determined by using the dc electric fields observed in the ionosphere. Since the conductivity parallel to the magnetic field is very high, there is nominally an extremely low parallel field component, so magnetic field lines act as equipotentials [Kelley, 1989]. This allows the electric field in the magnetosphere to map directly into the ionosphere. Thus the dynamics can be studied through measurements in only one region. At low altitudes, the electric field is generated at ionospheric heights and the mapping is reversed.

The coupling of the magnetosphere with the ionosphere is performed through field aligned currents. At ionospheric heights, the interplay between the electric field and parallel currents can be described by the following equations from Kelley, [1989] :

$$\vec{\nabla} \cdot \vec{J} = \vec{\nabla}_{\perp} \cdot \vec{J}_{\perp} + \partial J_{\parallel} / \partial s = 0 \quad (1.1.1)$$

$$J_{\parallel} = \int_{\Delta s} (\vec{\nabla}_{\perp} \cdot \vec{J}_{\perp}) ds \quad (1.1.2)$$

$$J_{\parallel} = \vec{\nabla}_{\perp} \cdot (\Sigma_{\perp} \cdot \vec{E}_{\perp}) \quad (1.1.3)$$

$$J_{\parallel} = \Sigma_P (\vec{\nabla}_{\perp} \cdot \vec{E}) + \vec{E} \cdot \vec{\nabla}_{\perp} \Sigma_P + (\vec{E} \times \hat{s}) \cdot \vec{\nabla}_{\perp} \Sigma_H \quad (1.1.4)$$

where J_{\parallel} is the parallel current, Σ_P and Σ_H are the height integrated Pedersen (conductivity parallel to \vec{E}) and Hall (conductivity parallel to $\vec{E} \times \vec{B}$) conductivities, respectively, \vec{E} is the convection electric field, and \hat{s} is the unit vector along the magnetic field line. Spatial derivatives are taken perpendicular to the magnetic field. If the conductivities are known, or can be inferred from the precipitation [Reiff, 1984], and the electric field is also known, Equation 1.1.4 yields the field aligned current needed to support that electric field in the ionosphere.

Parallel electric fields in collisionless plasmas are usually negligible, due to the high parallel conductivity given the ability of mobile electrons to short out such fields. The parallel fields associated with modest parallel currents thus need not be very large in most of the auroral zone. The magnetospheric convection electric field is such that there are natural gradients in the electric field [*Lyons, 1980*]. On the dusk side, a buildup of negative space charge separates sunward and antisunward flow and a converging electric field pattern exists. Parallel currents flow upward out of the ionosphere toward such a region. The diverging electric field on the dawn side will create an inward field aligned current. A portion of these currents close across the polar cap in the ionosphere and a portion close in the auroral oval. All of this occurs without the need for a parallel electric field. This scenario breaks down however in the particle acceleration region above 2500 km [*Carlson, et al., 1998b, Mozer, 1981*] where large parallel fields appear to be integral to particle acceleration. The energy range and pitch angle distributions of observed electrons are easily explained if we accept that the particles have fallen through a parallel potential drop, which is strong evidence for a parallel electric field. Numerous experiments have measured the presence of parallel fields and some optical observations of upward accelerated barium tracer ions are difficult to explain without invoking substantial parallel electric fields [*Stenbaek-Nielsen and Hallinan, 1979*].

There are many theories for parallel electric field generation, such as the magnetic mirror force [*Chiu and Schultz, 1978*], solitary waves [*Ergun, et al., 1998*], double layers and anomalous resistivity [*Hudson and Mozer, 1978, Tetreault, 1991*]. This debate is very important because of the role that the parallel fields play in particle energization and current closure. Observations of field aligned currents clearly show that high altitude electrons must overcome the mirror force, since current cannot be maintained between the ionosphere and

magnetosphere by small upward ionospheric ion currents. The hot electrons must contribute to the current and must be accelerated so they can penetrate far enough in to the ionosphere to complete the current loop.

Particle energization by electric fields need not only be confined to directions parallel to the magnetic field. Transverse ion acceleration due to perpendicular electric fields has been observed in the auroral zone on several early satellite flights [*Sharp, et al.*, 1977, *Klumpar*, 1979, *Yau, et al.*, 1983]. The experiments have shown a preference in heating perpendicular to \vec{B} , and a perpendicular wave electric field is then an obvious possibility. These ions, after heating, are forced out of the ionosphere by the mirror force and can account for the hot ions found in the magnetosphere. This is yet another instance of how ionospheric electric fields can have effects throughout the Earth's magnetosphere.

The very nature of electric fields in plasmas requires the discussion to include inhomogeneities. This is evident in the equation for current continuity and Poisson's equation,

$$\vec{\nabla} \cdot \vec{J} = -\partial\rho/\partial t \quad (1.1.5)$$

$$\vec{\nabla} \cdot \vec{E} = \rho/\epsilon_0 \quad (1.1.6)$$

which show the origin of electric fields in the ionosphere. Divergence in the current due from gravity, pressure gradients, or some other means, establishes a charge density. The resulting charge density will cause an electric field to be formed to force the divergence of the current to zero. The existence of electric fields is the single most salient parameter in the Earth's magnetosphere. Their highly variable time/space behavior describes the complex system.

Looking at the aurora, the above statement would seem obvious, and even incomplete. There are swirls and curls in the middle and at the edges of arcs. Visible "blobs" of

light pulse along the arcs with varying speeds and intensities. These irregularities are the essence of structure in the ionosphere. To understand this structure, we must understand the inhomogeneities in the electric field. It comes as no surprise that the terminologies of fluid mechanics are often used in considering electric fields in the ionosphere. The idea that electric fields can also be one to one related to plasma flows begs comparison to the characteristics of fluid flows. The stunning irregularities found in wind chambers and fluid cylinders offer direct comparisons with features in the aurora. The end visual result is perhaps due to different circumstances, but the similarity is too close to be ignored. Events of shearing and turbulence are common in fluid flows, and the ionosphere and magnetosphere are not immune to those same effects. Our efforts to understand these phenomenon must ultimately be based on understanding the generation and consequences of inhomogeneous electric fields.

1.1.3 Ionospheric Shears, Dynamics, and Inhomogeneities

In early work on turbulence in plasmas, *Kindel and Kennel [1971]* found that sufficiently large field aligned currents could drive the plasma into turbulence. The current driven electrostatic ion cyclotron (CDEIC) instability resulted in anomalous resistance, parallel electric fields, turbulent heating, and runaway particles. For $T_e \gg T_i$, the ion cyclotron mode was found to be unstable over a wide range of ionospheric parameters. When compared to the ion acoustic mode, the ion cyclotron mode was unstable for lower field aligned current values. The critical drift threshold required for wave generation increase in multicomponent plasmas [*Kindel and Kennel, 1971*]. Given these characteristics, the CDEIC instability was thought to be a likely source of turbulence and parallel fields in the ionosphere. S3-3

satellite measurements and laboratory experiments indeed showed that this instability is an important mechanism for creating resistance along field lines [Mozer, *et al.*, 1979]. However, CDEIC has since been rejected as a source of parallel electric fields for a number of reasons, but it cannot be ruled out as a source of small scale ionospheric structure.

As the pursuit to better understand turbulence in the laboratory and in the aurora began to develop, it was also seen that there were many examples of turbulent plasma behavior well below the threshold field aligned currents needed by CDEIC, indicating that perhaps other mechanisms might lead to turbulent flows. The free energy to support destabilization must come from somewhere, and the idea was proposed that perhaps transverse plasma shear could be responsible for plasma turbulence [Ganguli, *et al.*, 1985]. Shearing of plasma flows is common because of the multicomponent nature of the ionosphere where velocities are controlled by the mass of the species. Velocity shear as a means of generating turbulence is now an integral part of auroral physics, and has been used to explain many observed ionospheric and magnetospheric phenomenon, including transverse heating of heavy ions and ion conics [Klumppar, 1979]. Velocity shear has also been applied as a means of stabilizing certain instabilities under appropriate conditions [Perkins and Doles, 1975].

There have been numerous theoretical studies involving the generation of both electrostatic and electromagnetic waves from velocity shear [Ganguli, *et al.*, 1988, Pritchett, 1993, Gavrishchaka, *et al.*, 1997, Peñano and Ganguli, 1999b], experiments with laboratory plasmas [Walker, *et al.*, 1997, Amatucci, *et al.*, 1998], and experiments in the Earth's ionosphere [Kintner, 1976, Kelley and Carlson, 1977, Earle, *et al.*, 1989, Moore, *et al.*, 1996, Bonnell, 1997]. Inhomogeneities in the density and electric field caused by velocity shear have been addressed by Basu, *et al.*, [1998]. The role of perpendicular shear flow that

generates the Kelvin-Helmholtz instability [Kintner and Seyler, 1995] has been studied in regards to the boundary of the magnetosphere [Miura, 1987], undulations in diffuse aurora [Yamamoto, et al., 1994, Kelley, 1989], auroral breakup [Kinney, et al., 1999], and the evolution of the instability with respect to ionospheric parameters [Keskinen, et al., 1988]. Most of the investigations have centered around the Kelvin-Helmholtz instability and the combination of velocity shear and the CDEIC instability, where there is ample data from both the laboratories and rocket/satellite experiments.

There have been problems, however, in applying the laboratory and theoretical results to space experiment results. The main difficulty is that the laboratory and theoretical methods have excellent resolution to map out the three dimensional flow fields and to distinguish temporal events from spatial structures, while the space experiments are generally single point measurements of a field quantity with no definitive means of separating space and time. Another problem was found through laboratory results which have identified onsets of turbulence in regions where both field aligned currents are much less than the thresholds given by Kindel and Kennel [1971] and the observed turbulent waves have very different characteristics than those of either the CDEIC or the Kelvin-Helmholtz instability [Amatucci, et al., 1994].

Recent theoretical studies and laboratory experiments have investigated an instability where a nonuniform dc perpendicular electric field can destabilize ion-cyclotron waves [Ganguli, et al., 1985, Amatucci, et al., 1998, Gavrishchaka, et al., 1996]. The free energy needed for the destabilization comes from the nonuniformity in the electric field, which creates a region of negative energy density. A more detailed description of this instability, termed the inhomogeneous energy density driven instability, or IEDDI, will be given in

Chapter 4. The essential characteristics of the IEDDI mechanism is that the instability sharply lowers the threshold current levels required for onset of wave generation and the resulting waves are broadband near the relevant cyclotron frequency.

The nonuniformity of the electric field is important for creating the free energy necessary for wave growth in the IEDD instability. The nonuniformity also implies a velocity shear. In order to better compare the laboratory with the rocket and satellite results, a shear frequency, ω_s , has been defined [Ganguli, *et al.*, 1994] as

$$\omega_s = \left| \frac{dV}{dx} \right|_{max} \approx \frac{V^0}{L} \quad (1.1.7)$$

where V^0 is the peak of the flow velocity and L is the scale size of the flow region. After dividing by the ion gyrofrequency, a non-dimensional measure of the shear can be defined. This allows us to categorize the shear strength. Each category has its own characteristics and implications for wave growth. Lower frequency waves can evolve in a self-consistent manner into regions with larger shear frequencies [Ganguli, *et al.*, 1994]. This method of categorization has had limited usefulness in the compendium of satellite and sounding rocket data, since single point measurements are unable to yield scale size information and the only way to associate a shear frequency with a data set is to make severe assumptions about the relation between time and space.

1.2 Motivation for Auroral Turbulence II

The efforts to distinguish spatial and temporal effects was one of the motivations behind the Auroral Turbulence II (AT II) sounding rocket mission. The AT II mission consisted of three nearly identically instrumented payloads that would slowly separate from each other with

each payload's position and velocity well known. Auroral Turbulence, originally proposed over ten years ago and launched in 1993, was not successful since the nose-cone/subpayloads did not correctly deploy from the main payload and therefore three point measurements were not made. The need for multipoint measurements in the auroral zone was sufficient to motivate another rocket flight, and so a second Auroral Turbulence rocket was constructed.

The AT II mission was to be the first sounding rocket mission to fly a cluster of three spacecraft with a full complement of particle, electric, and magnetic field measurements. The measurements were designed to provide detailed spatial and temporal correlations between electric and magnetic fluctuations, wave activity, particle precipitation, and current signatures [Torbert, 1990]. The three payloads would be able to investigate the full vector electric and magnetic fields and determine their vorticity.

1.3 Thesis Statement

In this thesis we shall present multi-point observations of a highly localized, sheared plasma flow and the simultaneous observation of electrostatic waves. We shall use the multiple payload configuration to show that the region of high shear and wave activity is both spatially confined and temporally changing. We investigate several reasons for the large dc electric field we encountered. Finally, we show that the characteristics of the shear, along with the observed electrostatic waves and low field aligned current, are in excellent agreement with the inhomogeneous energy density driven instability (IEDDI) that has been proposed by Ganguli, *et al.* [1985] and observed in the laboratory by Amatucci, *et al.* [1994].

In Chapter 2, we give an overview of the AT II instrumentation. Chapter 3 presents the local and global launch conditions and details the vehicle and instrument performance. The

flight data is also presented in this chapter. In Chapter 4, we discuss temporal events, spatial structures, high electric fields, and broadband electrostatic wave power in the context of velocity shear theory. In the final chapter we summarize and reflect upon our findings. In Appendix A we show the methods used in converting the potential differences between the spherical sensors to Earth-frame electric fields including despinning, applying the proper offsets and gains to the electric field data, and rotating the data into an appropriate coordinate system. Appendix B gives the model used to describe how a payload shadows a region of space from precipitating electrons and how that can produce an adverse effect on the electric field measurement. Appendix C shows how the peak energy of an electron beam is determined from electron detectors with a finite energy threshold.

Chapter 2

Auroral Turbulence II Instrumentation

The Auroral Turbulence II rocket consisted of three payloads that carried identical instrumentation, with additional instrumentation on the Main payload. A schematic of the three payload system and the instrumentation flown on each is presented in Figure 2-1. We present here an overview of the various detectors and probes that were flown on the payloads.

2.1 Particle Detectors

The particle detectors used were ion electrostatic analyzers (ESAs) and electron medium-sized electrostatic analyzers (MESAs). The ESA and MESA are symmetric, hemispherical detectors with concentric hemispherical plates at variable potentials in a now standard “top-hat” design [Carlson, *et al.*, 1983]. The ESA detectors are designed so each look-direction bin has a geometric factor approximately $5 \times 10^{-3} \text{ cm}^2 \text{ sr eV/eV}$, while the MESAs are designed for a geometry factor near $5 \times 10^{-4} \text{ cm}^2 \text{ sr eV/eV}$. All like detectors were identically designed, manufactured, assembled, and cross-calibrated. Calibration was carried out in a small vacuum chamber. An electron/ion gun provided input to each detector as a rotating platform moved each detector through all available values of yaw, pitch, and roll. The electron detector high voltage supplies allowed measurement of particle energies from 9 eV to 12.2 keV. Each electron detector had the capability of simultaneously measuring 14 pitch angle directions. The allowed energy range of the ion detectors was 6 eV to 9.8 keV,

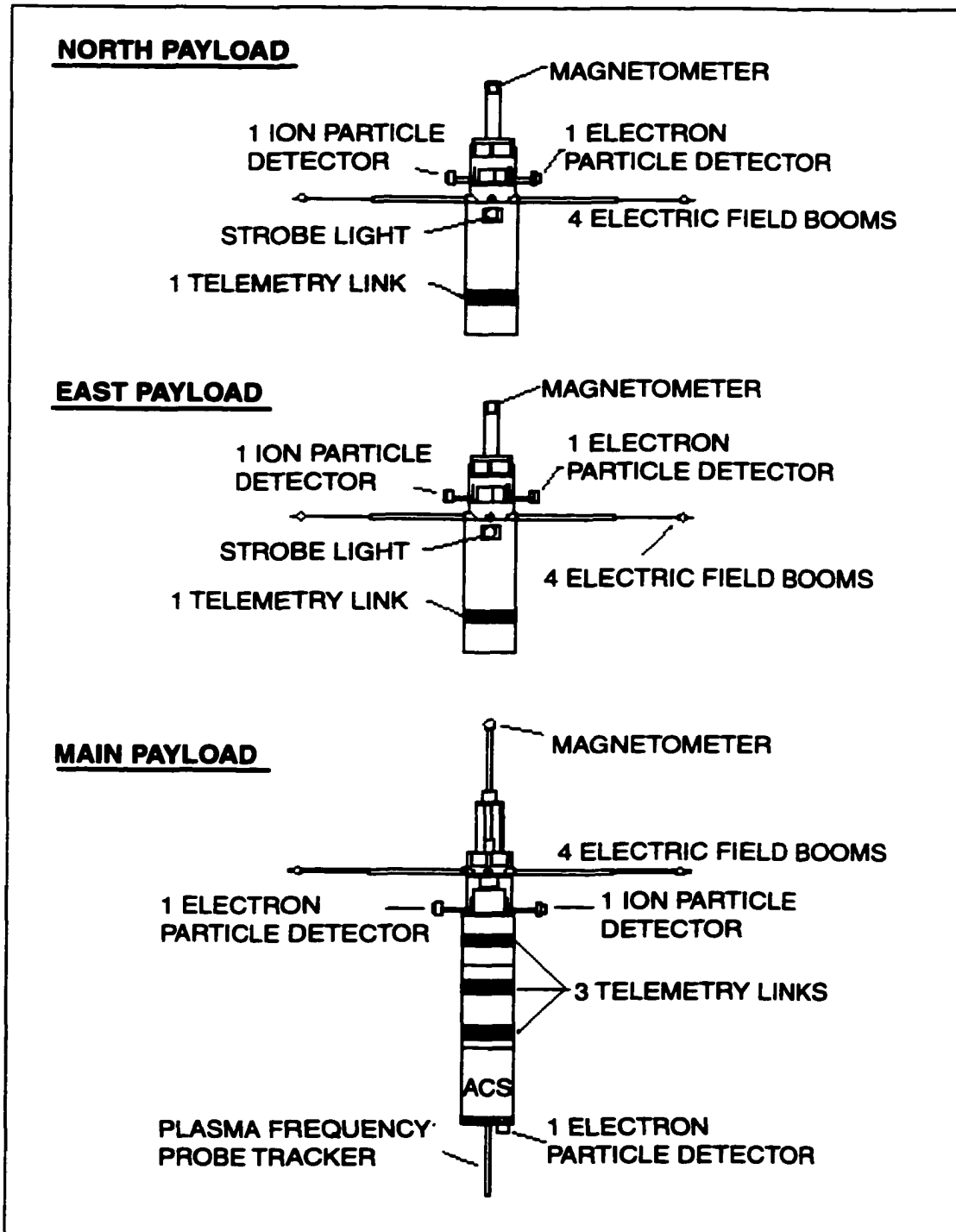


Figure 2-1: AT II Payload Diagrams.

and these detectors could sample over ten pitch angle directions. Each payload carried one of each kind of detector and each detector was mounted opposite the other on the payload body.

The Main payload was also equipped with an electron detector coined the BAGEL. This electron detector was fixed at the end of the Main payload such that after subpayload deployments, the BAGEL look directions would always be antiparallel to the magnetic field. Each bin in this toroidal electron detector had a large geometric factor of $3.82 \times 10^{-4} \text{ cm}^2 \text{ sr eV/eV}$, and allowed electron energies in the range of 11 eV to 4.4 keV.

2.2 Magnetometers and Other Instrumentation

Each payload carried a three axis digital fluxgate vector magnetometer in the fore of the spacecraft, constructed and tested by the Technical University of Denmark and the Sodankyla Geophysical Institute, which sampled the magnetic environment at 2 kHz. Each payload was also fitted with a Swept Frequency Analyzer (SFA) box that analyzed the signal from the potential spheres to focus on the high frequency regime. A strobe light was also mounted on each of the payloads. Camera stations at Deadhorse, AK, located under apogee, could use their narrow-field cameras to view the auroral fine structure while using the strobe lights to locate the payload positions within the aurora, although cloud cover over Deadhorse on the night of the launch prohibited their use.

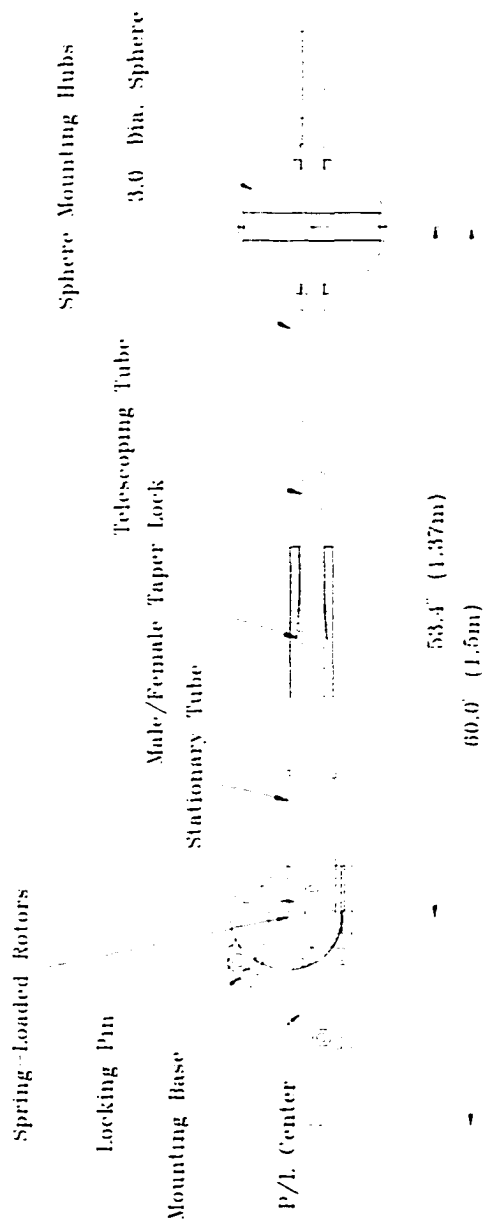
Although the three payload system was designed to be identically equipped, there were several instruments placed on the Main payload only. Utah State University provided a Plasma Frequency Probe (PFP), which consisted of a long tubular instrument containing several rings held at various potentials that would be used to determine the local plasma

frequency. Also solely on the Main payload was the Plasma Frequency Tracker, provided by Dartmouth College, designed to measure high frequencies up to 5 MHz with a resolution of 8000 samples per second. Finally, NASA equipped the Main payload with an Attitude Control System (ACS) that fired argon gas from small jets around the payload to maneuver the Main payload through the rotations needed to properly deploy the subpayloads. The ACS system was also then used to keep the spin axis of the payload parallel with the magnetic field for the remainder of the flight, but unfortunately interfered with the electric field experiment. We shall address this complication in the next chapter.

2.3 Electric Field Experiment

2.3.1 Preparation

The electric potential spheres are three inch aluminum spheres that are placed upon two section, 1.5 m telescoping booms made from G-10, a fiberglass composite. Each boom also had two commercial microswitches: one was attached at the base of the boom and configured to activate when the boom had correctly flopped down, and the other was attached near the end of the boom to detect when the inner section of boom had fully telescoped out of the outer portion. All of the preamplifier electronics to be used by the spheres were fabricated at Cornell University, while the spheres themselves, the booms, and the deployment systems were manufactured and assembled at UNH. Consult Figure 2-2 for the mechanical drawing of the components.



Auroral Turbulence 2 "Minnesota Type" Telescoping E-Field Booms

Figure 2-2: Electric field experiment hardware schematic.

2.3.2 Calibration and Extraction of Data

Calibrations of the electric potential spheres were performed at Cornell University. Each sphere pair was loaded with their corresponding preamplifiers. A single-ended test signal was used as input to one of the spheres, while the other was maintained at ground. This calibration provided the response of the sphere/preamp system and an appropriate gain for the system over the required frequency range. This was carried out for all possible sphere pairs that could be used in determining potential difference. A detailed description of the conversion of the digitized data words from the preamplifiers of the potential spheres to electric fields is given in Appendix A.

Chapter 3

Data Presentation

We now present the data from the Auroral Turbulence II sounding rocket mission. These data consist of the auroral environment at the time of the launch, including ground based and satellite measurements of key parameters, actual launch parameters, vehicle performance, and the science experiment data from the various instruments. We begin with an overview of the global and local auroral conditions near the time of the rocket launch, the night of February 11, 1997 at 0836 UT.

3.1 Auroral Environment

At the Poker Flat Research Range, a new Science Center was constructed to aid mission investigators in determining optimal launch conditions. The Principal Investigator no longer needs to go outside and look up at the sky to decide on an appropriate launch time. Now, with the aid of the Internet, a variety of real-time information on the local and global environment can be used to make the decision to launch. All of the following environment data were available to us in either real time or near real time. We present both snapshots and continuous time series of these data.

3.1.1 Ground Based Imagery

Three all-sky cameras, located at Poker Flat, Fort Yukon, and Kaktovik, were used to help determine the auroral conditions in the flight trajectory. Their locations can be found on



Figure 3-1: All-sky image from Kaktovik during the flight (T+365 seconds). The bright dot in the image is an enhanced pixel representing the location of the three payloads.

the trajectory map in Figure 3-11. At the launch site, separate monitors gave continuous coverage from Poker Flat and 5 second updates from the other locations. Each location also recorded the all-sky camera data. Figure 3-1 shows a still image from the Kaktovik all-sky camera. The universal date and time, as well as the camera location, are displayed in the upper left corner. The top of the figure is south, the bottom is north, left is west, and right is east. This frame of the all-sky camera data is very representative of the environment at the payload apogee. The large arc is in existence for minutes, drifting slowly to the north. Later images show spirals moving rapidly along the poleward edge of this arc. Further north, this particular image shows the residues of some amorphous patches of aurora that vary in intensity, size, and location directly at the Kaktovik zenith. Before launch, this region was broader and much more intense, but its dimensions and brightness diminished from the time of the launch until the loss of signal from the telemetry unit. In the top section of the image there is a rather bright dot in the middle of the large arc. The dot is a digitally enhanced pixel representing the position of the Main payload. The subpayloads, on the scale of the image, would lie inside the bright pixel.

A Meridional Scanning Photometer (MSP) was also in use at Poker Flat. Figure 3-2 shows the MSP data taken during the night of the launch. The plot shows intensity in kiloRayleighs for different optical emissions, as a function of universal time. The four panels, from top to bottom, show emissions at the 6300 nm atomic oxygen red line, the 4861 nm hydrogen line, the 4278 nm nitrogen line, and the 5577 nm atomic oxygen green line. The auroral activity overhead Poker Flat is not a direct indicator of activity at all locations along the payload trajectory, but it shows that there was good auroral activity at and to the north of the launch facility.

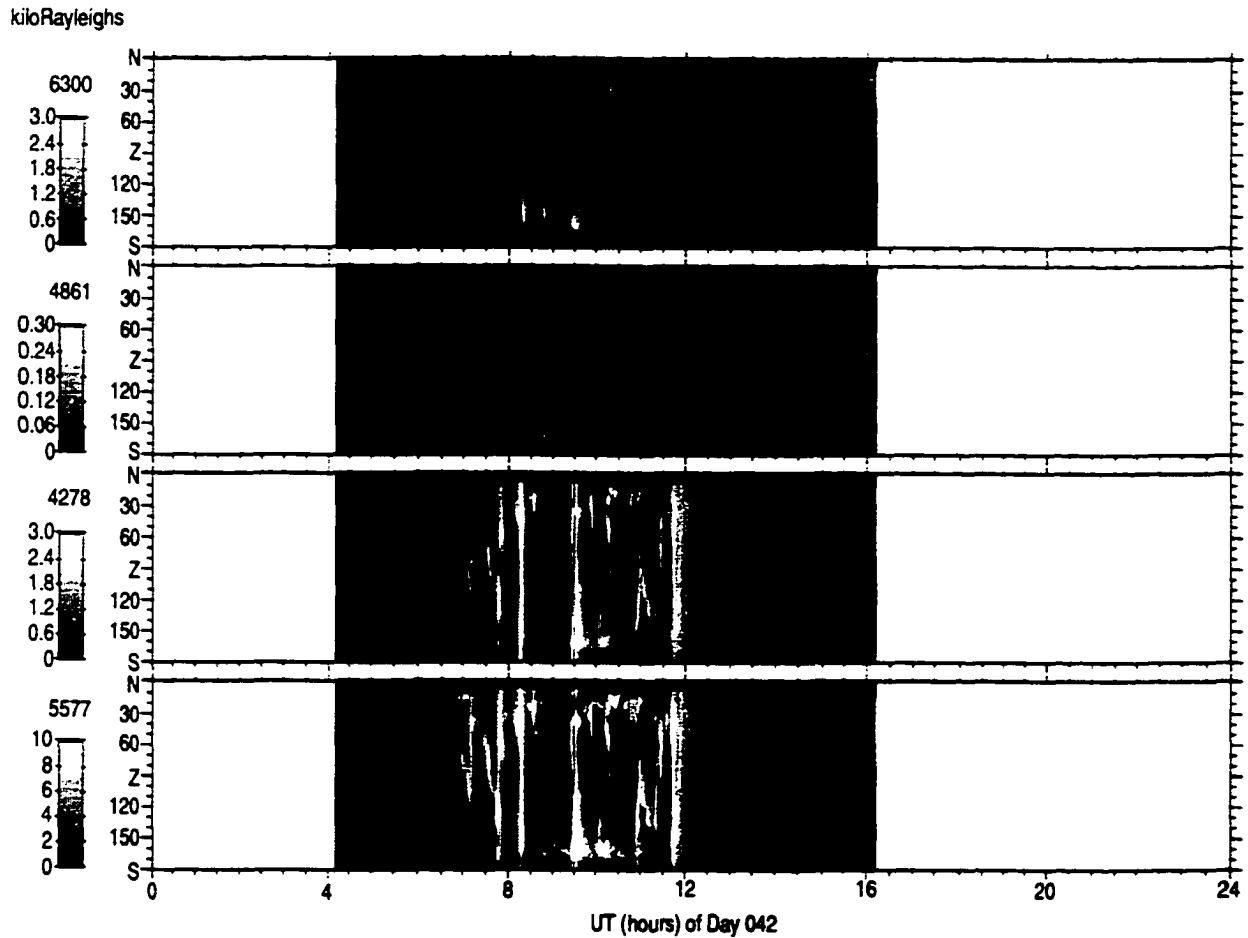


Figure 3-2: Poker Flat meridional scanning photometer data from February 11, 1997 (courtesy Poker Flat Research Range). Each panel is a different atomic spectral line emission with a color bar brightness index.

3.1.2 Ground Based Magnetometer Data

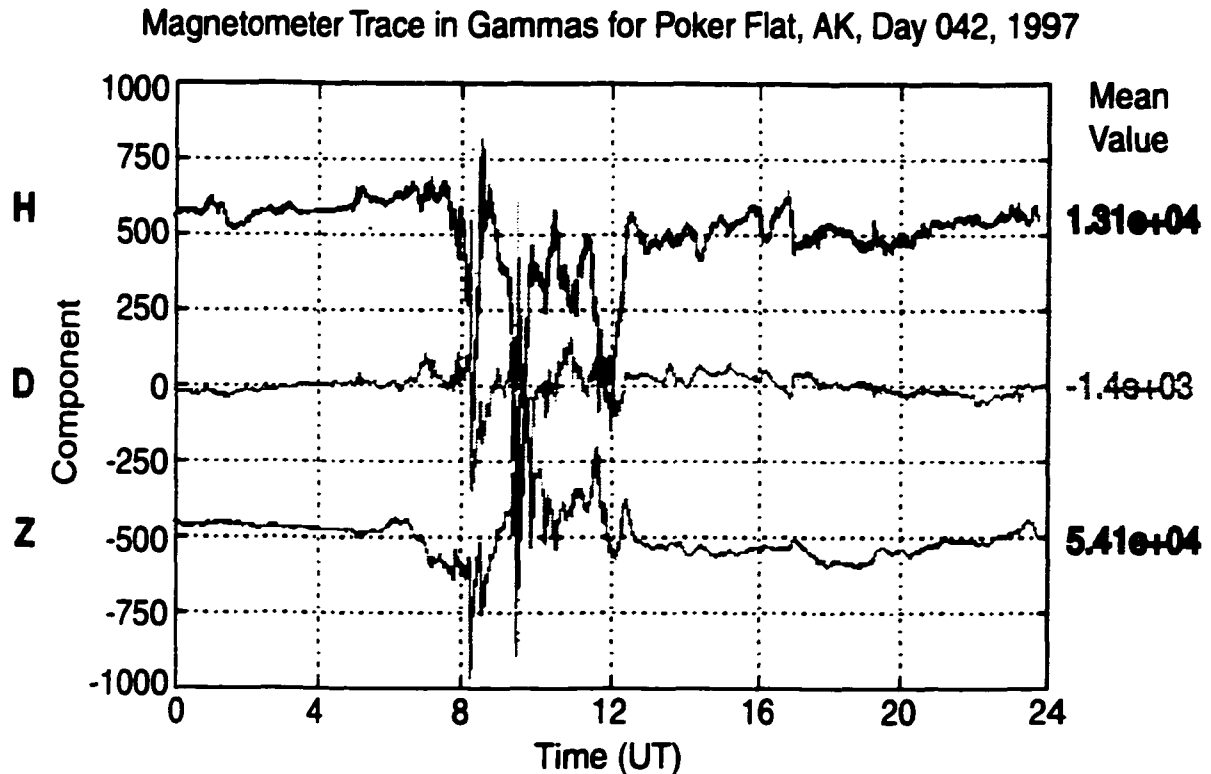


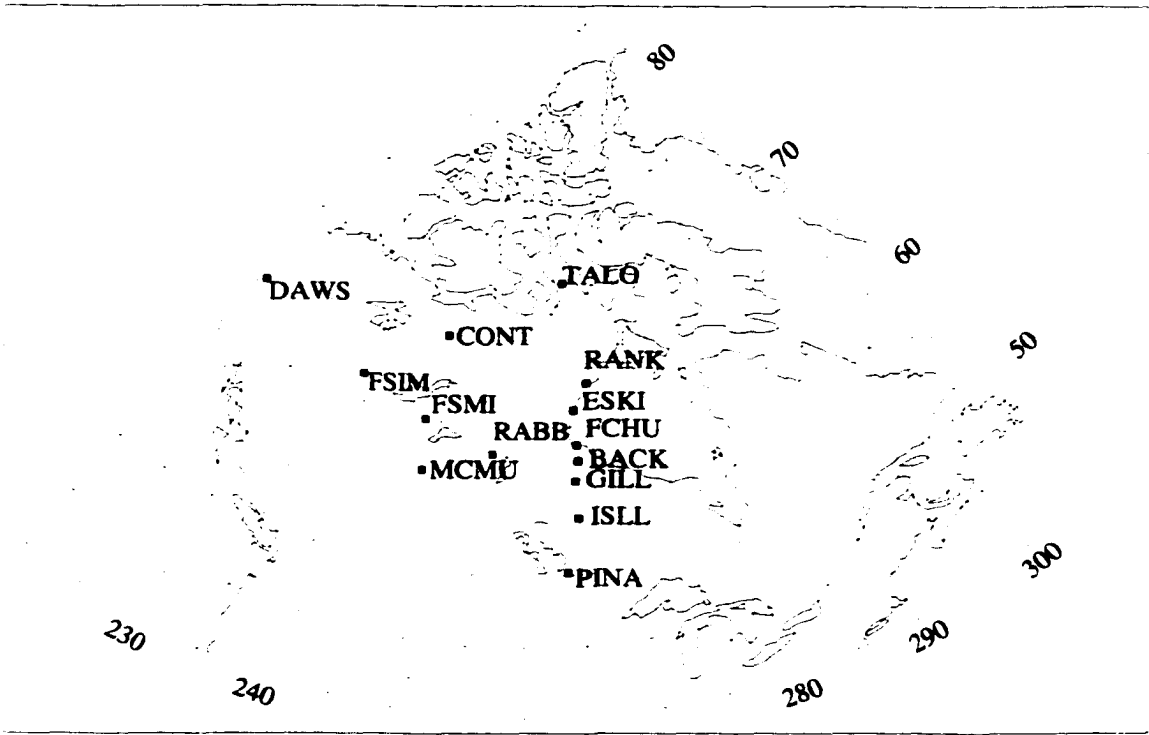
Figure 3-3: Poker Flat three axis magnetometer data (courtesy PFRR).

Real time ground based magnetometer data is also important for determining appropriate launch conditions. Auroral electrojet currents cause large magnetic disturbances measurable on the ground. Figure 3-3 shows the three components of the magnetic field, measured in Gammas (1 Gamma = 1 nT), from the Poker Flat magnetometer, as a function of time. The H component is the north component, Z is the up component, and D completes the right handed system in the western direction. Note that the H and Z components are offset by 500 Gammas in order to better view the data. Large disturbances in all of the field values begin at roughly 0700 UT. Comparisons with the scanning photometer data in Figure 3-2 show excellent correlation between magnetic disturbances and observed auroral

forms.

Data recorded at the launch facility is not useful for the prediction of when auroral forms may be entering the flight trajectory region. This prediction is done by looking at magnetometers to the east of the launch site. A magnetic substorm triggers a westward traveling surge that can be detected by magnetometers in succession, from east to west. Figure 3-4 is a geographic map of northern Canada showing the locations of the magnetometer sites making up the CANOPUS magnetometer chain. The table below the figure gives the exact coordinates of each site. The series of sites from Pinawa to Taloyoak lie on the same line of longitude, which does not make them useful for our predictions of westward motion. However, the sites of Fort Churchill, Rabbit Lake, Fort Smith, and Dawson provide good longitudinal coverage of the auroral oval. At the launch site, we observed real time data from these magnetometers. Figure 3-5, Figure 3-6, and Figure 3-7 show the time history on the 42nd day of the year (Feb. 11) of the x, y, and z components, respectively, of the CANOPUS chain magnetometers, excluding the Back station. The y axis scale is shown to the left of the bottom panel, and each panel has its own horizontal dashed line representing the zero level for that site. The x, y, z system of the three plots is the right-handed north, east, down coordinate system, just like the system in Figure 3-3. All three plots show magnetic disturbances after 0600 UT. To observe the westward traveling auroral activity, consider Figure 3-5. Here, Fort Churchill measures a decrease in the northward magnetic component near 0615. Rabbit Lake observes the same decrease at 0630, Fort Smith at 0640, and Dawson at 0730. This clear evidence of westward progressing currents is used to predict the onset of auroral activity in the flight path.

These ground based measurements provide a good forecast of when we could expect



Magnetometer Site Coordinates

LOCATION	SITE CODE	GEODETIC LAT	GEODETIC LONG	CANOPUS LAT	EDFL LONG	L	INVLAT
Back	BACK	57.72	265.83	65.229	336.671	7.47	68.53
Contwoyto Lake	CONT	65.75	248.75	72.394	311.295	12.36	73.47
Dawson	DAWS	64.05	220.89	67.323	277.477	5.89	65.67
Eskimo Point	ESKI	61.11	265.95	68.621	336.465	10.20	71.75
Fort Churchill	FCHU	58.76	265.92	66.268	336.682	8.18	69.53
Fort McMurray	MCMU	56.66	248.79	63.233	315.304	5.49	64.74
Fort Simpson	FSIM	61.76	238.77	67.396	300.580	6.84	67.52
Fort Smith	FSMI	60.02	248.05	66.556	313.205	7.05	67.88
Gillam	GILL	56.38	265.36	63.883	336.205	6.66	67.20
Island Lake	ISLL	53.86	265.34	61.385	336.419	5.49	64.74
Pinawa	PINA	50.20	263.96	57.732	335.079	4.25	60.98
Rabbit Lake	RABB	58.22	256.32	65.333	324.380	6.94	67.69
Rankin Inlet	RANK	62.82	267.89	70.374	338.923	12.44	73.53
Taloyoak	TALO	69.54	266.45	77.145	335.856	29.96	79.47

'EDFL ==> Eccentric Dipole Field Line traced coordinates.

Figure 3-4: Map of CANOPUS chain magnetometers (courtesy Canadian Space Agency).

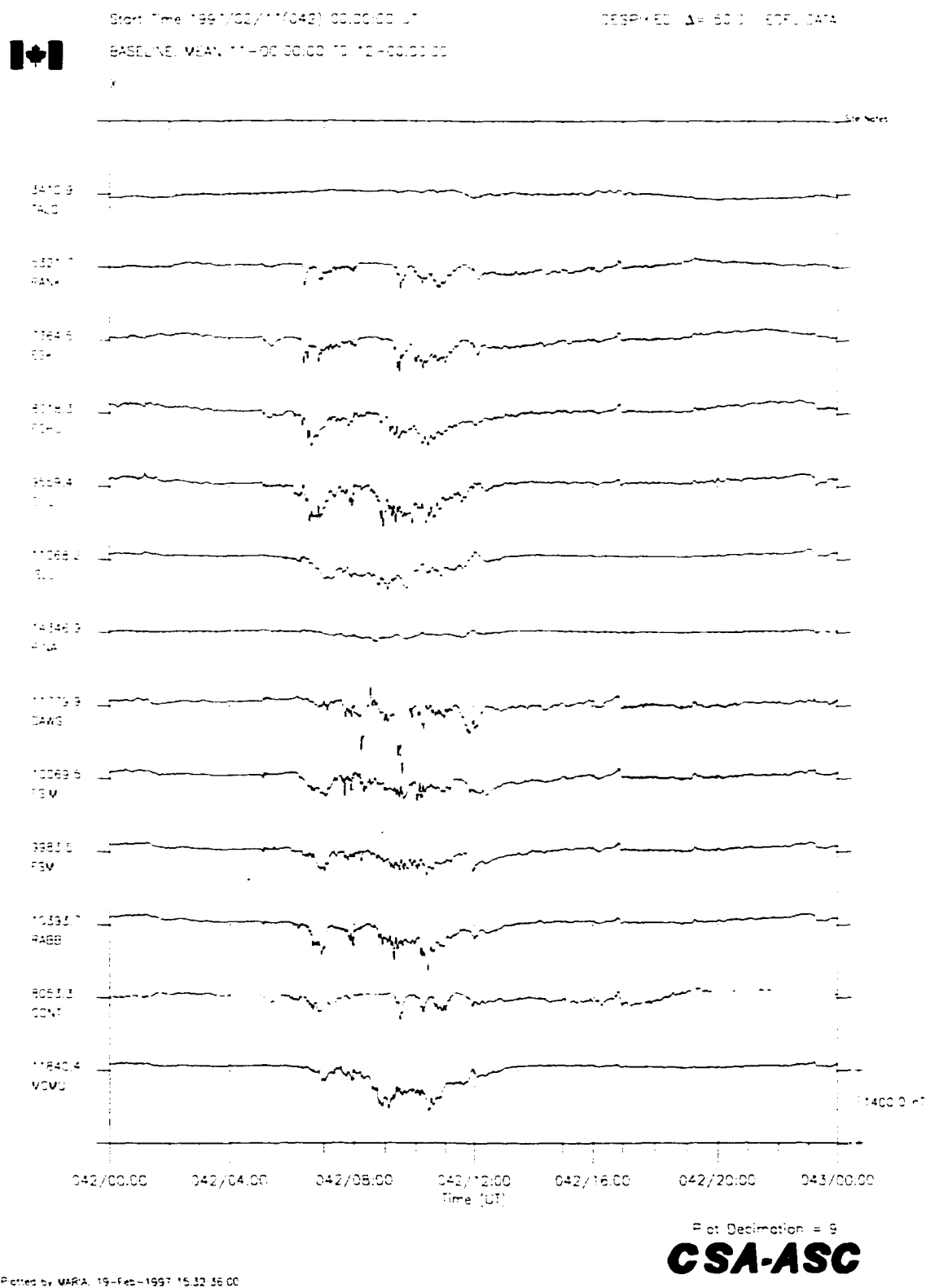


Figure 3-5: Stack plot of x-component magnetometer chain data (courtesy CSA).

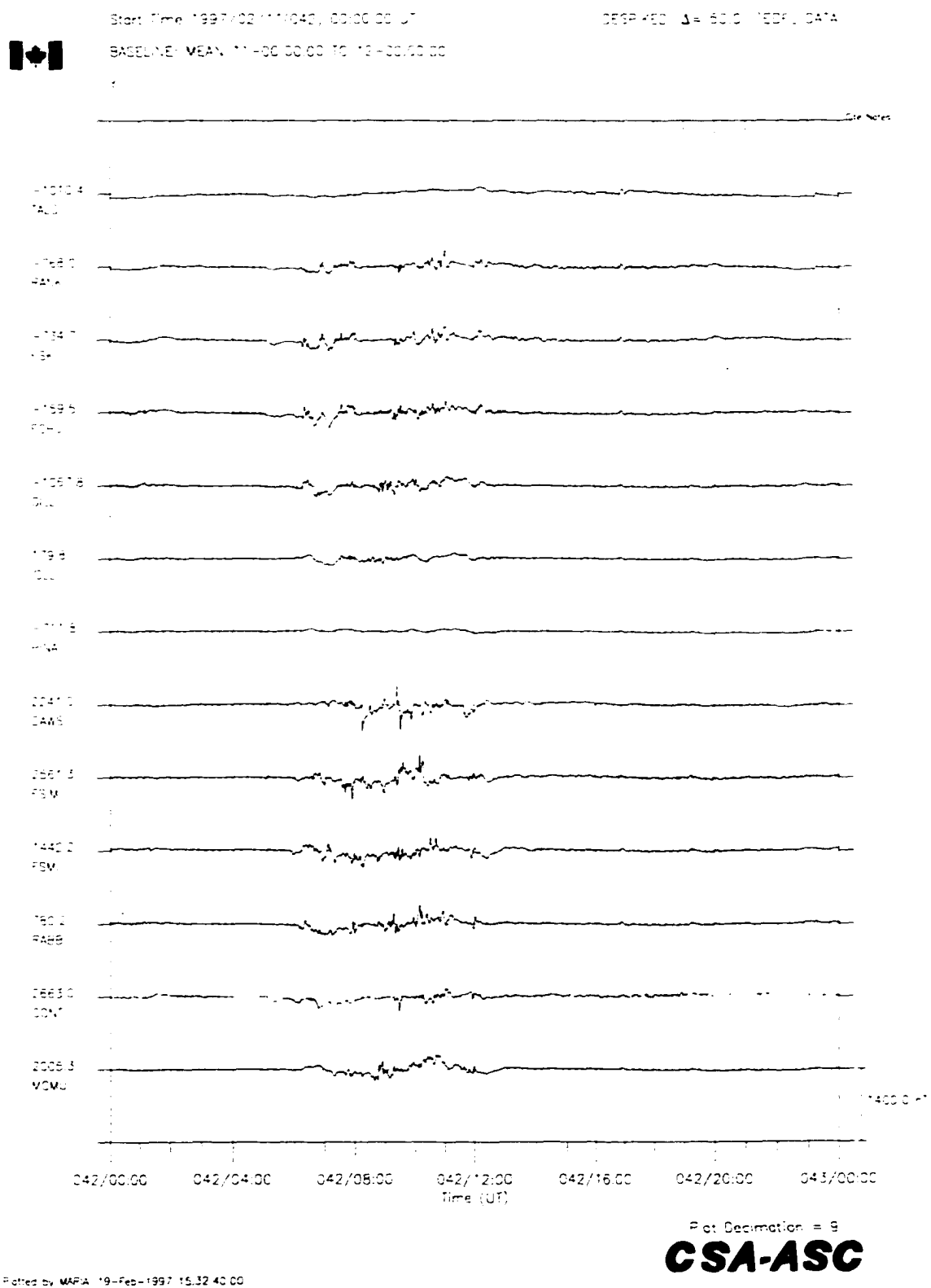
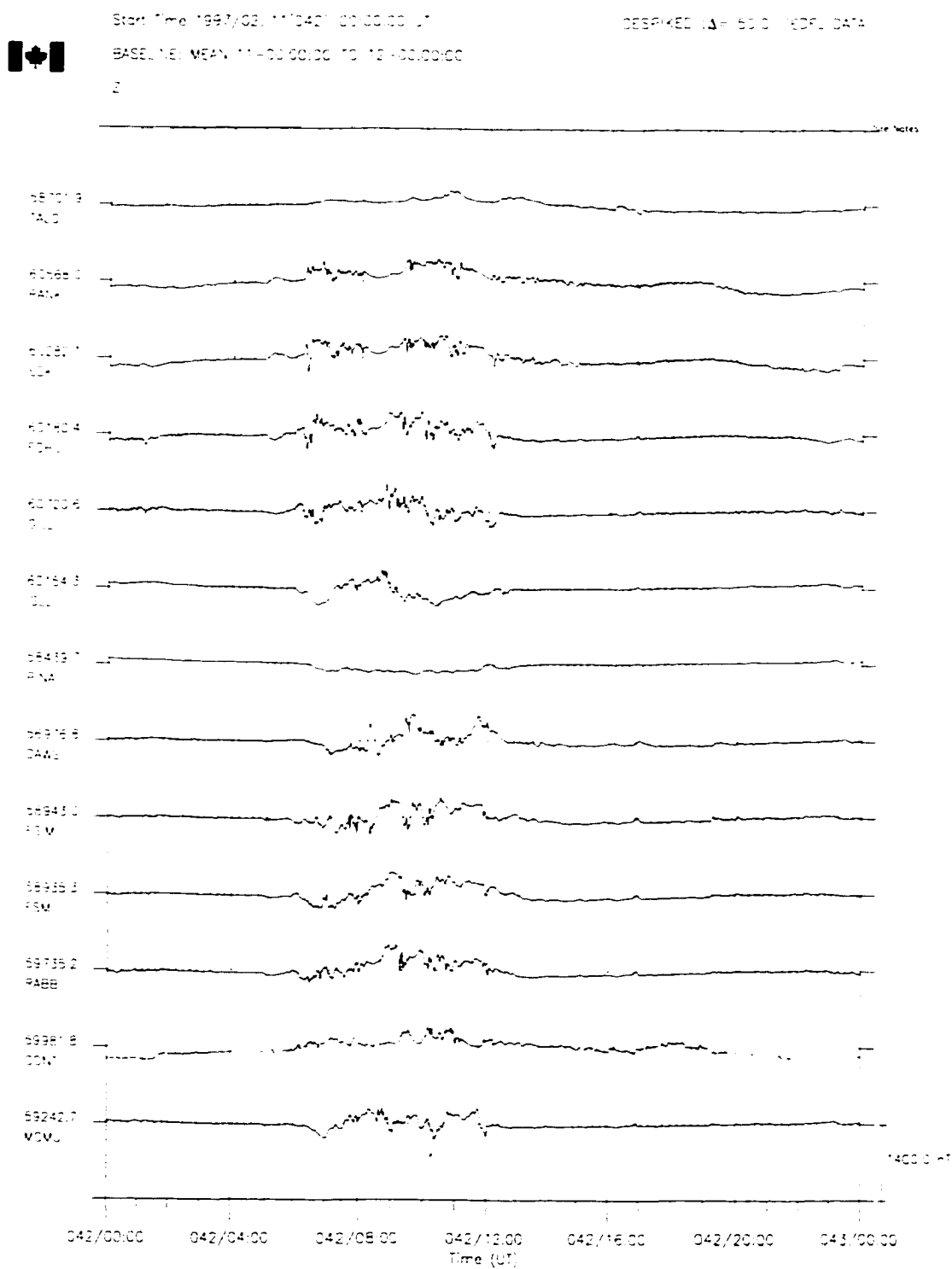


Figure 3-6: Stack plot of y-component magnetometer chain data (courtesy CSA).



Plot Decimation = 9
CSA-ASC

Plotted by MARIA 19-Feb-1997 15:32:43.00

Figure 3-7: Stack plot of z-component magnetometer chain data (courtesy CSA).

strong auroral activity in the trajectory range. The lead times from these data are anywhere from zero to tens of minutes. Longer lead times, and a more global picture of the auroral environment, come from satellite data, presented next.

3.1.3 WIND, GOES, and POLAR Data

The WIND satellite provides information on the characteristics of the solar wind. Figure 3-8 shows, from top to bottom, the solar wind velocity, density, thermal speed, and angle with respect with the spacecraft, from the Mass-Time-Of-Flight (MTOF) proton monitor.

The geosynchronous GOES satellites measure X-rays, energetic particles and magnetic field. Figure 3-9 shows two days of magnetometer data from the GOES8 satellite. In the figure, HP is the magnetic component parallel to the satellite spin axis, oriented northward, HE is Earthward, and HN completes the right-handed system, mainly eastward. Notice the large decreases in the HP component at 0500 and 0700 UT. The HP component is nominally sinusoidal, due to the orbital path of the satellite, and these decreases represent the stretching of the Earth's magnetic tail, storing energy for release in the form of a substorm. We use these data together with the WIND data to anticipate good launch conditions. Good launch conditions entail a relatively high density, high speed solar wind, southward pointing z-component of the solar wind magnetic field and a strong stretching of the tail. Reconnection will occur in the tail, which causes the magnetosphere to relax and snap back to its preferred dipole geometry. This release presages an auroral enhancement, a westward traveling surge, and an auroral break-up [*Kivelson and Russell, 1995*].

The WIND and GOES satellites indicate the input to the Earth's magnetosphere and ionosphere. To observe the effects of these inputs, we turn our attention to the POLAR

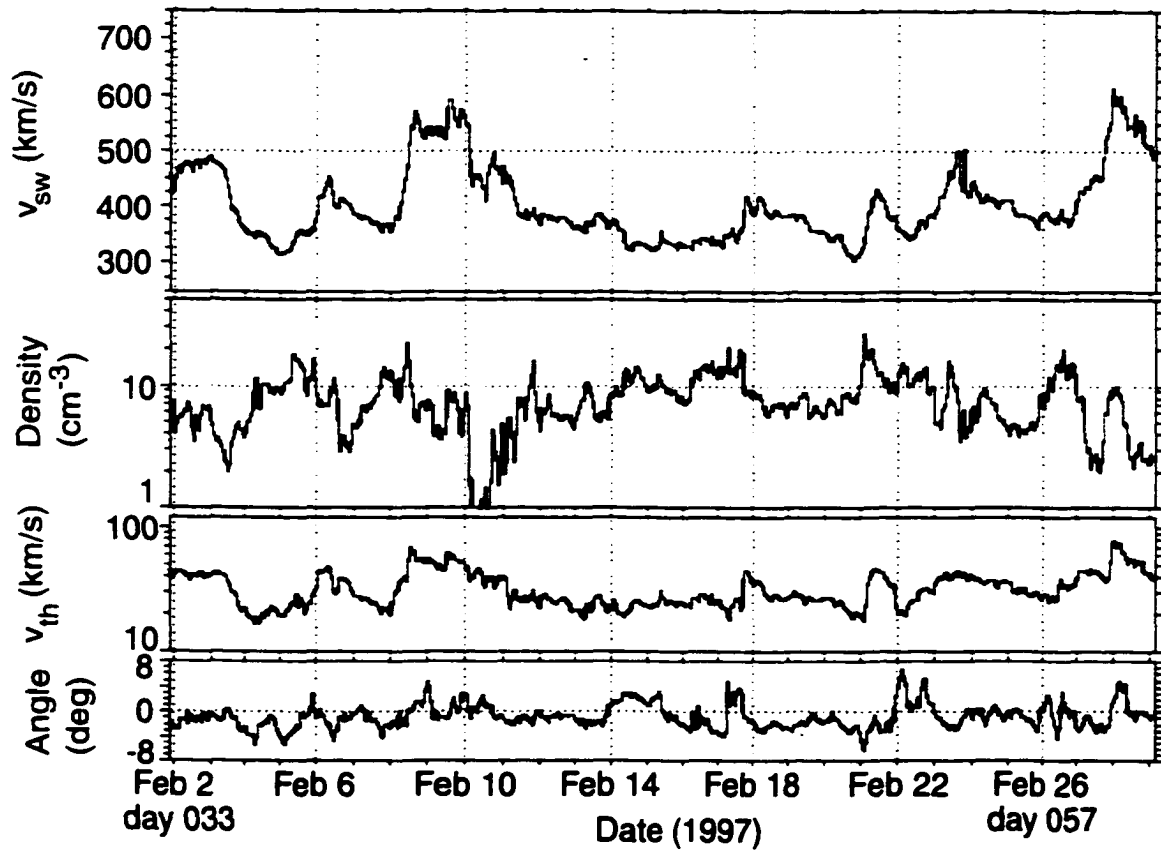


Figure 3-8: WIND solar proton monitor data from February, 1997 (courtesy University of Maryland).

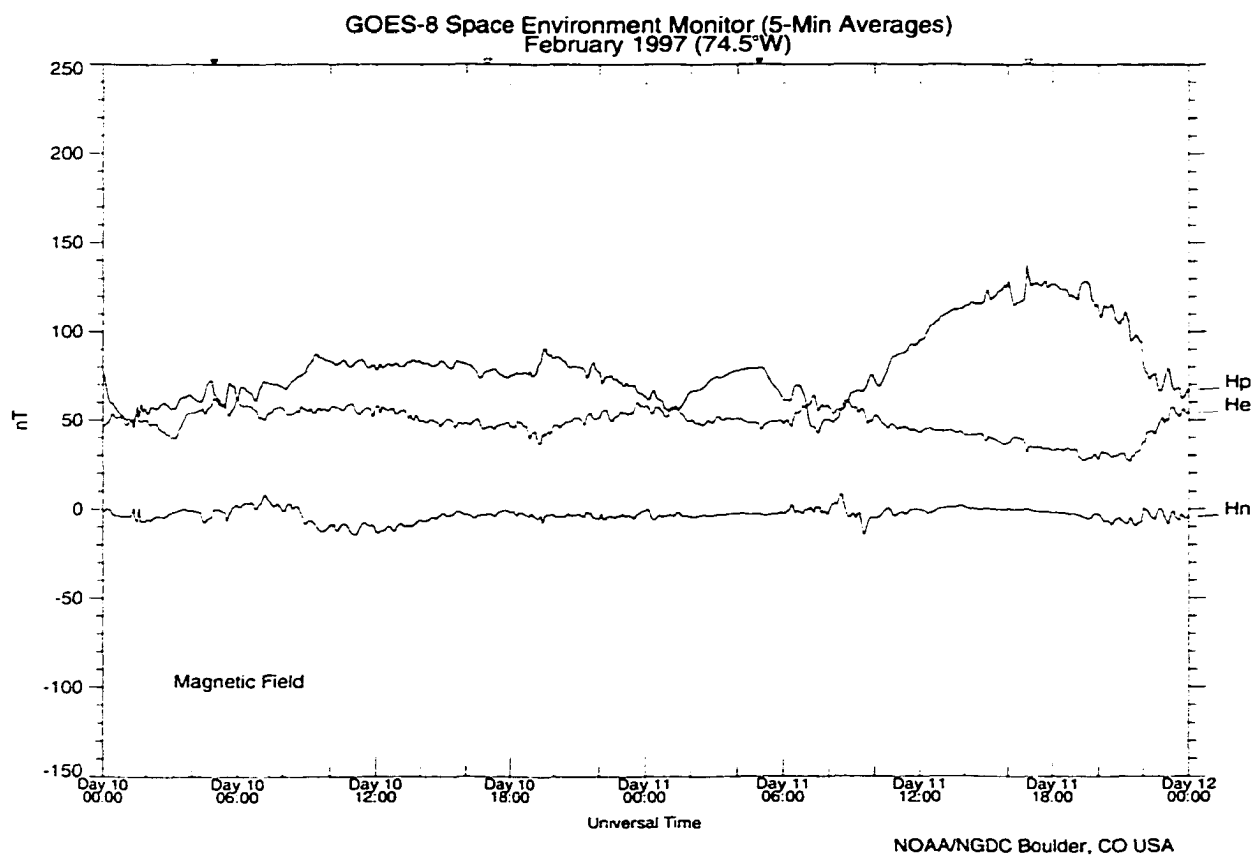


Figure 3-9: GOES-8 magnetometer data (courtesy NOAA/NGDC).

spacecraft. Figure 3-10 is a composite of images from the POLAR ultraviolet imager (UVI) from 0801 to 0901 UT on February 11. The left image in each frame shows the UVI data mapped onto the Earth in geographic coordinates, and the right image is in magnetic coordinates. In the geographic mapping, Greenland can be seen at the bottom of the image, and Alaska is near the top. The color bar between the images displays the photon intensity, and the time of each image pair. A bulge near the Alaskan-Canadian border can be seen to move westward (top two panels) and break up (middle two panels). The bottom panels show another bulge forming in western Canada and also starting to move westward. This provides a global context for the night of the AT II launch.

To summarize, the environmental data has two main purposes. The first is their use as a predictor of auroral activity. The ability to obtain real time data from satellites, cameras, and magnetometers allows prediction of auroral activity, and is now a standard means of anticipating good launch conditions. Secondly, having these data after the launch gives context to the payload data. With this in mind, we now present the specifics of the AT II launch.

3.2 Launch Details

3.2.1 Launch Specifics

The Auroral Turbulence II sounding rocket mission (NASA 40:011) was launched from the Poker Flat Research Range on February 11, 1997 at 0836:40 UT, or 10:36 p.m. local time. The launch facility is located at 65° 06' N latitude and 147° 28' W longitude. The payloads were carried by a four stage Black Brant XII rocket.

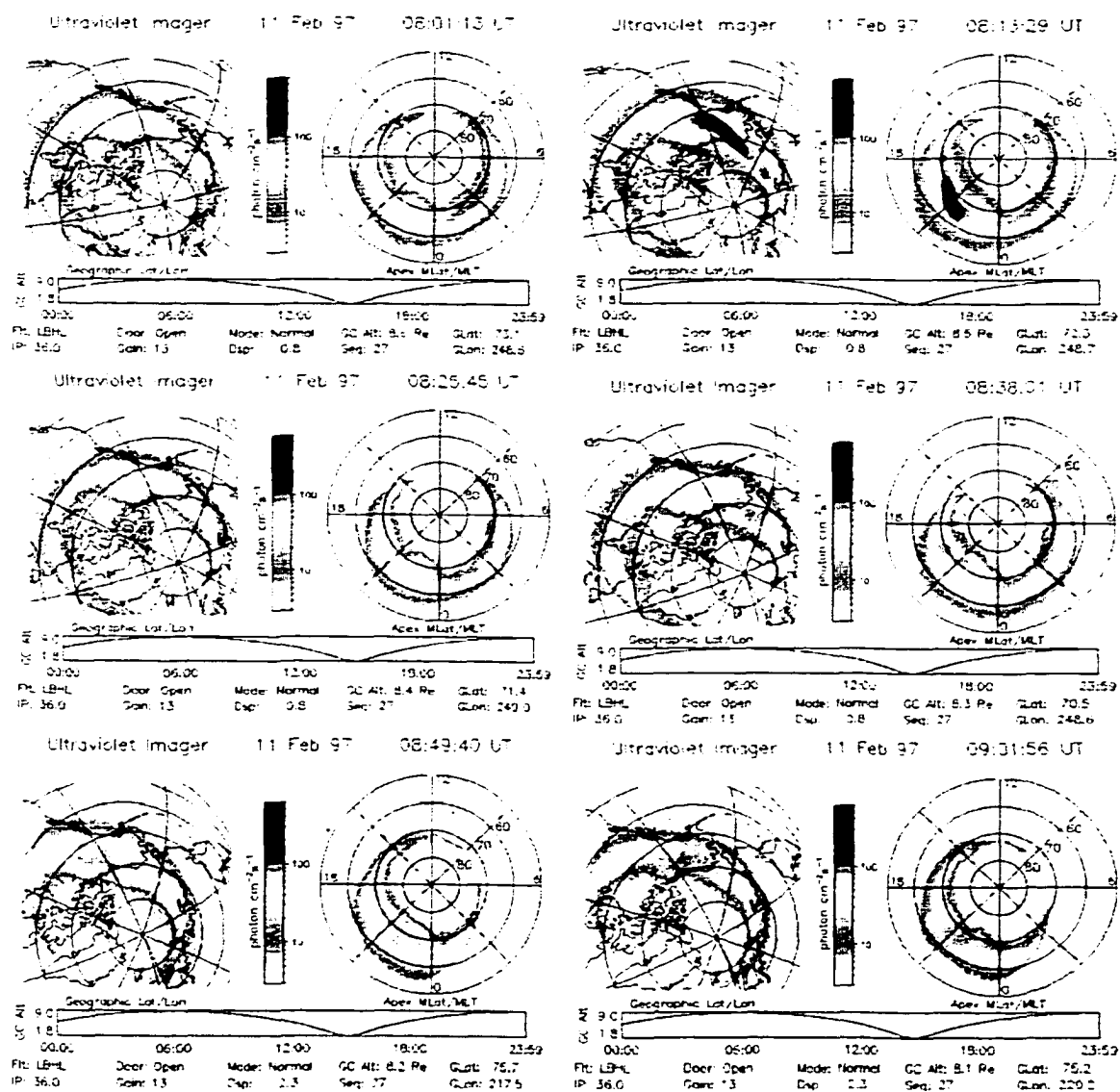


Figure 3-10: Composite of POLAR Ultraviolet Imager during AT II launch (courtesy MSFC/NASA/M. Brittner, UW).

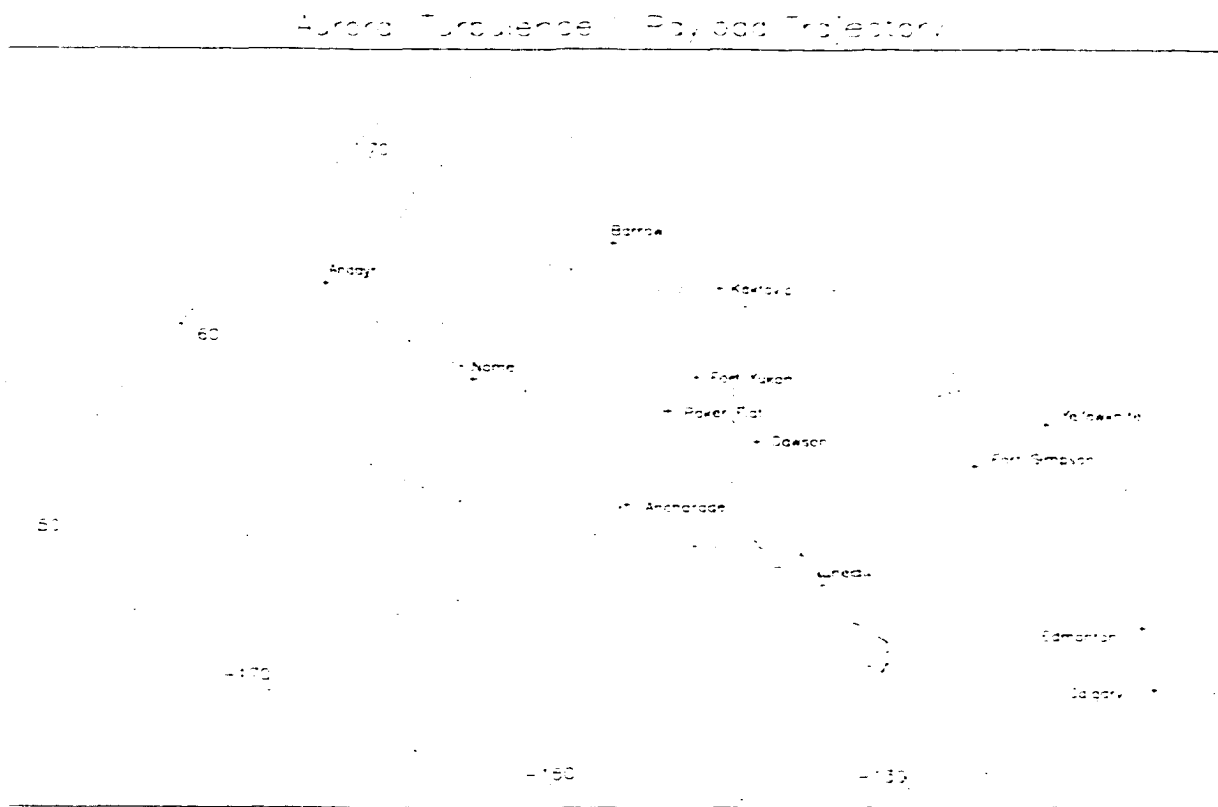


Figure 3-11: AT II Main payload geographic footprint trajectory.

3.2.2 Payload Trajectory

The AT II payload trajectory is shown in Figures 3-11 and 3-12. Figure 3-11 shows the geographic location of the main payload for the duration of the flight in geographic coordinates. Some city locations have been added for reference. All-sky cameras at Poker Flat, Fort Yukon, and Kaktovik. Magnetometers are located at Poker Flat, Dawson, Yellowknife and Fort Simpson.

Figure 3-12 shows the positions of the three payloads with respect to the launch facility, located at (0,0,0) in the figure. The black trace is the Main payload, the red is the East, and the blue, which is very close to the black trace, is the North payload. Note that the

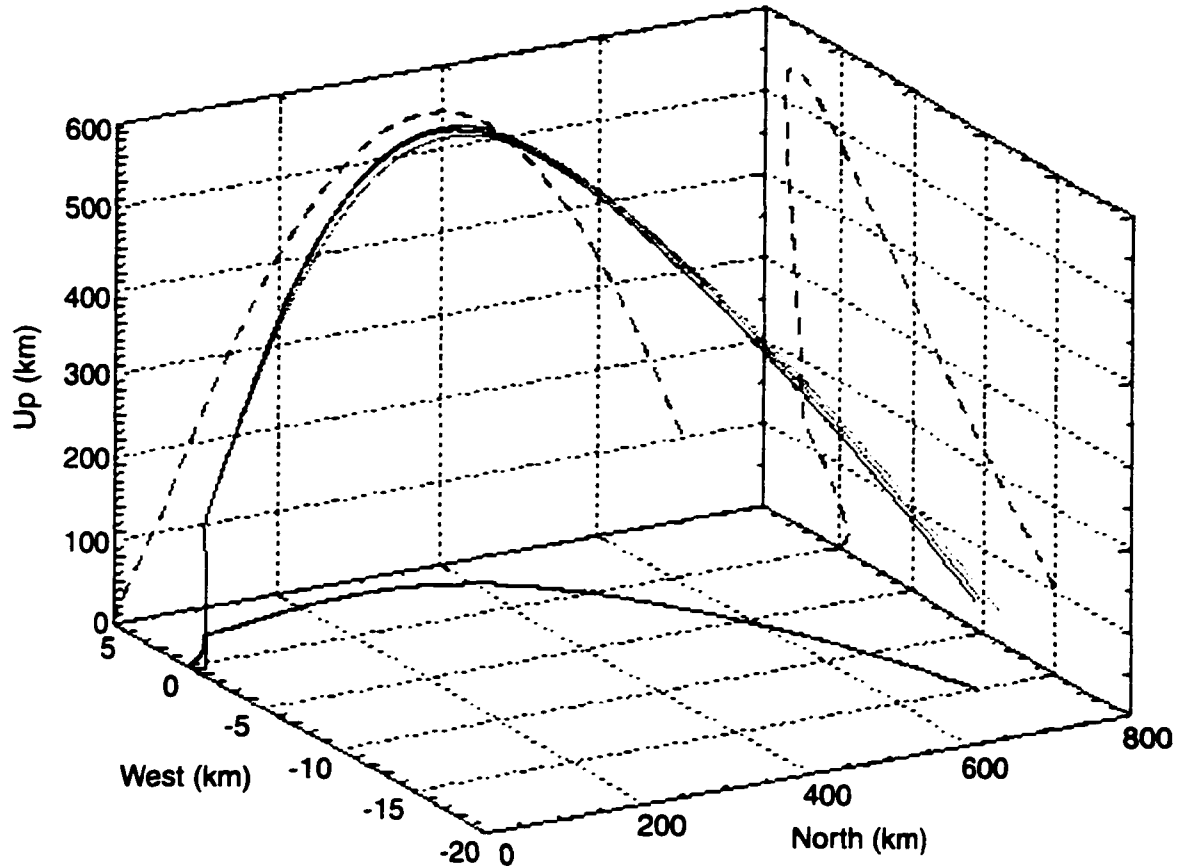


Figure 3-12: AT II payload trajectories.

three axes are not the same scale, in order to distinguish the differences between the payload trajectories.

Figure 3-13 is a schematic of the northward-moving three-payload configuration. The North payload is the most north and reached the highest elevation of the three payloads. The East payload is the easternmost payload. The Main closely follows the North payload. The payloads separated before T+150 seconds flight time, and reached a maximum separation distance of nearly 6 km.

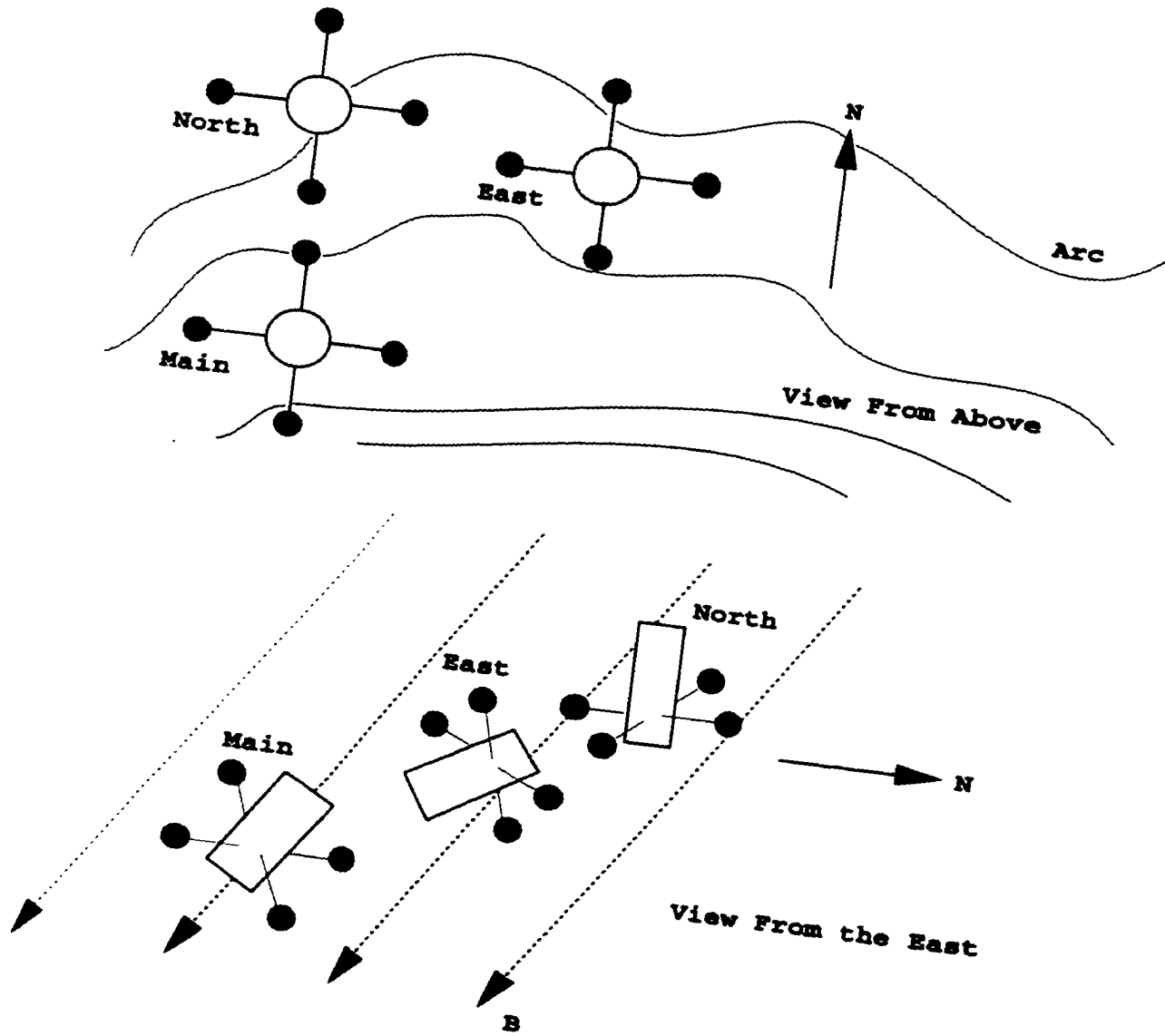


Figure 3-13: AT II payload orientation.

3.2.3 Vehicle and Instrument Performance

At T+120 seconds after launch, the Main payload maneuvered to specific orientations before ejecting the subpayloads. The payloads traveled at roughly 1 km/s. The North payload was deployed first. Its nominal ejection velocity had the spin axis oriented northward, with a tip angle of 45° with respect to \vec{B} , and a speed of 10 m/s relative to the Main payload. The magnetometer data showed that this deployment was very successful, with the actual spin axis being $6.8^\circ (\pm 1^\circ)$ west of north and $47^\circ (\pm 1^\circ)$ from \vec{B} . The East payload was not deployed as cleanly. Its nominal ejection conditions had the spin axis eastward, with the spin axis 30° to \vec{B} , and with a relative speed of 10 m/s with respect to the Main payload. The result had the spin axis at 25° with respect to \vec{B} and 54° east of north. It is unknown what caused the deployment to be so far from 90° east of north. Attitude information from the Main payload shows that the payload did rotate fully to the east, but perhaps the ejection was not clean so the payload was ejected at less of an angle than was desired. Despite this, both payloads did eject, and after ejection the Main payload properly oriented its spin axis to \vec{B} .

Telemetry for all three payloads experienced no problems. The science mission had mixed successes. The electron MESAs worked as expected, but had difficulty resolving the lowest energy steps. This was because the sweeping high voltage supplies could not drop quickly enough from the highest to the lowest steps. The BAGEL detector received reliable data from two of its four channels. The other channels were shorted out possibly from a warping of the Delrin insert below the hemispheric sections. The ion ESAs saw counts, but only in regions of high electron fluxes, and they followed the electron data exactly. The

large openings in the ESAs may have allowed high energy electron contamination, making the ion data extremely difficult to interpret correctly.

The electric field booms on all payloads fully deployed and operated correctly, although there were errors in the data associated with electron shadowing that will be discussed in the next section. However, the Main payload electric field data were severely compromised. The Main payload ACS system used an argon gas to keep the spin axis oriented with \vec{B} . Apparently, the threshold departure angle was set too low, for the gas fired almost continuously throughout the flight, until the gas reserves were depleted. The release of argon sufficiently changed the local plasma conditions that the electric field spheres reached saturation levels whenever the argon was released. This makes the Main payload electric field data effectively unusable until after the gas runs out. Unfortunately, there is little electric field activity at that time or for the remainder of the flight. As for the magnetic field experiment, all three payloads had no problems with the operations of the magnetometers.

The Plasma Frequency Tracker and Swept Frequency Analyzers worked nominally. However, the gain level for the SFAs was incorrectly set, so a very small level activity tended to saturate the instrumentation. This level of activity is met for many portions of the flight and the incorrect setting makes the data at these times not useful. Also, the Plasma Frequency Probe from Utah University was not operational for any portion of the flight. Lastly, it was not possible to determine the operational status of the strobe lights, since there was extreme cloud cover at the Deadhorse, AK location, and therefore no way to use the narrow-field cameras to track the payloads or to obtain high resolution optical conditions at apogee. Although the camera data would be extremely useful, the launch window was nearing its end, and with growing concern about a decreasing window time, and with

excellent auroral activity that particular night, the decision was made to launch despite the cloud cover at the camera site.

3.3 Measurements

We now present the data results from the various instrumentation on the payloads. There are measurements from all three payloads, but similarities between payloads allow us to present only one measurement when appropriate. When differences between payloads are relevant to this thesis, the appropriate data will be displayed. All of the payloads obtained data from roughly T+150 seconds to Loss Of Signal (LOS) at T+754 seconds.

Figures 3-14, 3-15, and 3-16 show an overview of the electron precipitation, high frequency electric field, and dc electric field data for the flight. In the next sections, we shall indicate salient features in each data set, and will also present magnetometer data and analysis of the low frequency wave data from the electric field experiment.

3.3.1 Particle Data

Figure 3-14 shows a spectrogram of electron energy from the East payload MESA instrument, plotted as a function of flight time. The data are summed over all look angle directions of the MESA. The color bar to the right of the main panel shows the electron differential energy flux intensity. The lowest energy steps have been removed from the spectrogram because of the unreliable readings from the high voltage supplies.

We can identify most of the auroral forms that were traversed by the payloads if we refer back to Figure 3-1. Comparison with Figure 3-14 shows that the payloads are in the large, stable arc for nearly 100 seconds, or from T+300 to T+400 seconds. Prior to

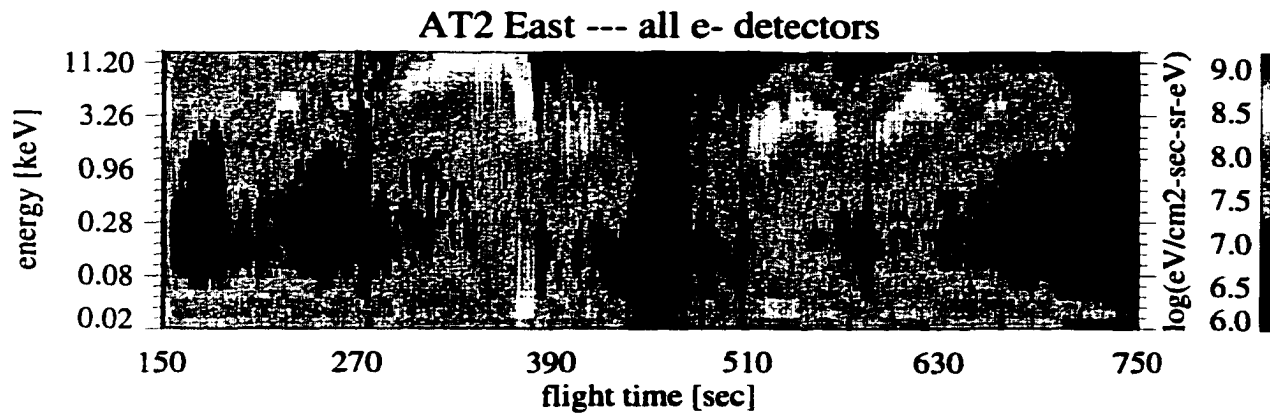


Figure 3-14: Survey plot of East payload electron data.

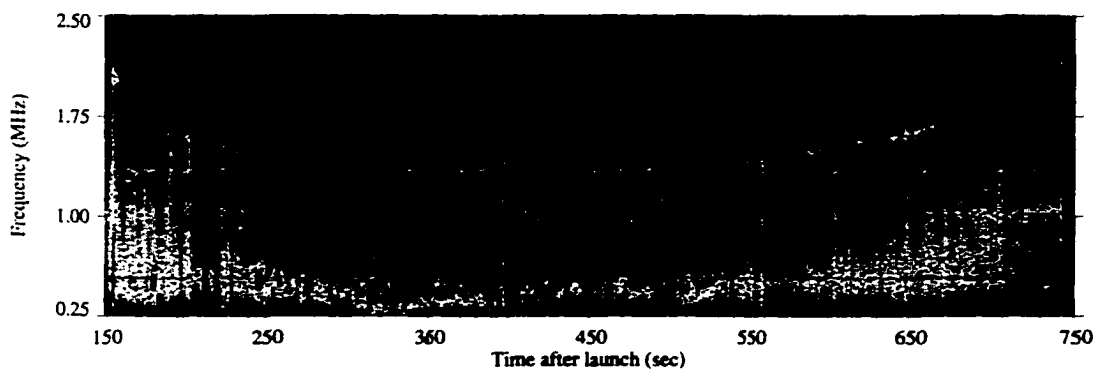


Figure 3-15: Survey plot of Main payload HF data (from [McAdams, et al., 1997]).

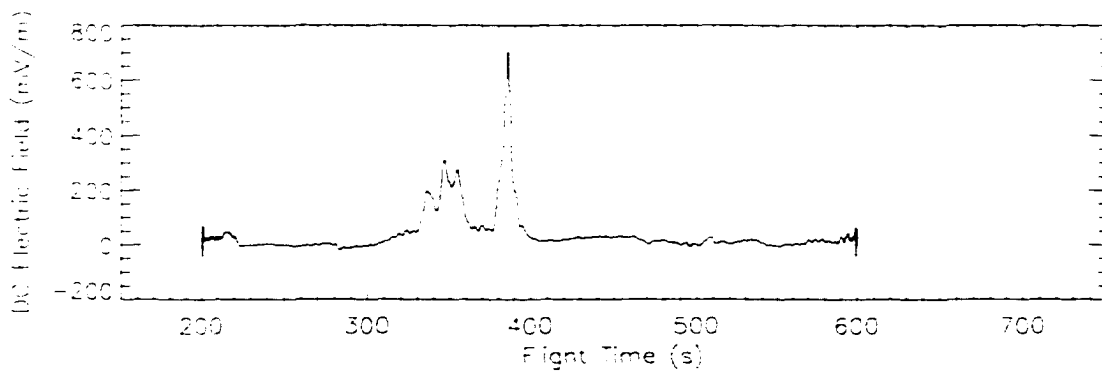


Figure 3-16: Survey plot of dc electric field from the North payload.

crossing this arc, the payloads traversed another arc, not seen on the Kaktovik image, from T+200 to T+270 seconds. This arc was much lower in energy flux than the large arc in the all-sky still image. After T+400 seconds, the payloads traversed several more smaller arc structures, which correspond with the amorphous and either barely visual or sub-visual arcs near the center of the all-sky image. Their beam energies are also lower than the large arc. While there are many interesting features of these lower intensity arcs, the work in this thesis has focused on the large, stable arc, and particularly the poleward portion of that arc. Figures 3-17 and 3-18 display the electron data from the North and East payloads, respectively, in the same form as Figure 3-14, but from T+300 to T+410 seconds. This encompasses the entire pass through the large arc. From the all-sky images and the superimposed payload positions, as well as from the magnetometer data, it is evident that the payloads traversed the arc roughly 45° to the poleward arc edge. Knowing how the payloads traveled through the arc, and using the payload velocity relative to the arc of 0.5 km/s, we can determine the thickness of the arc to be approximately 35 km. Both payloads see similar electron precipitation, but there are some differences. The East payload measures a slightly lower peak energy of the electron beam than the North payload. This is most evident in the range between T+335 and T+385 seconds. Each MESA is identical and cross-calibrated, so this discrepancy is not instrumental and should represent a small change in precipitation along the arc. The separation between the North and East payloads along the arc is 860 m at T+300 seconds and 1425 m at T+410 seconds. It is important to note that the Main payload data, not presented here, show electron precipitation similar to the North payload. While it is obvious that the electron fluxes change as the arc is traversed, the Main and North payloads show the same fluxes, when adjusted for delay between the

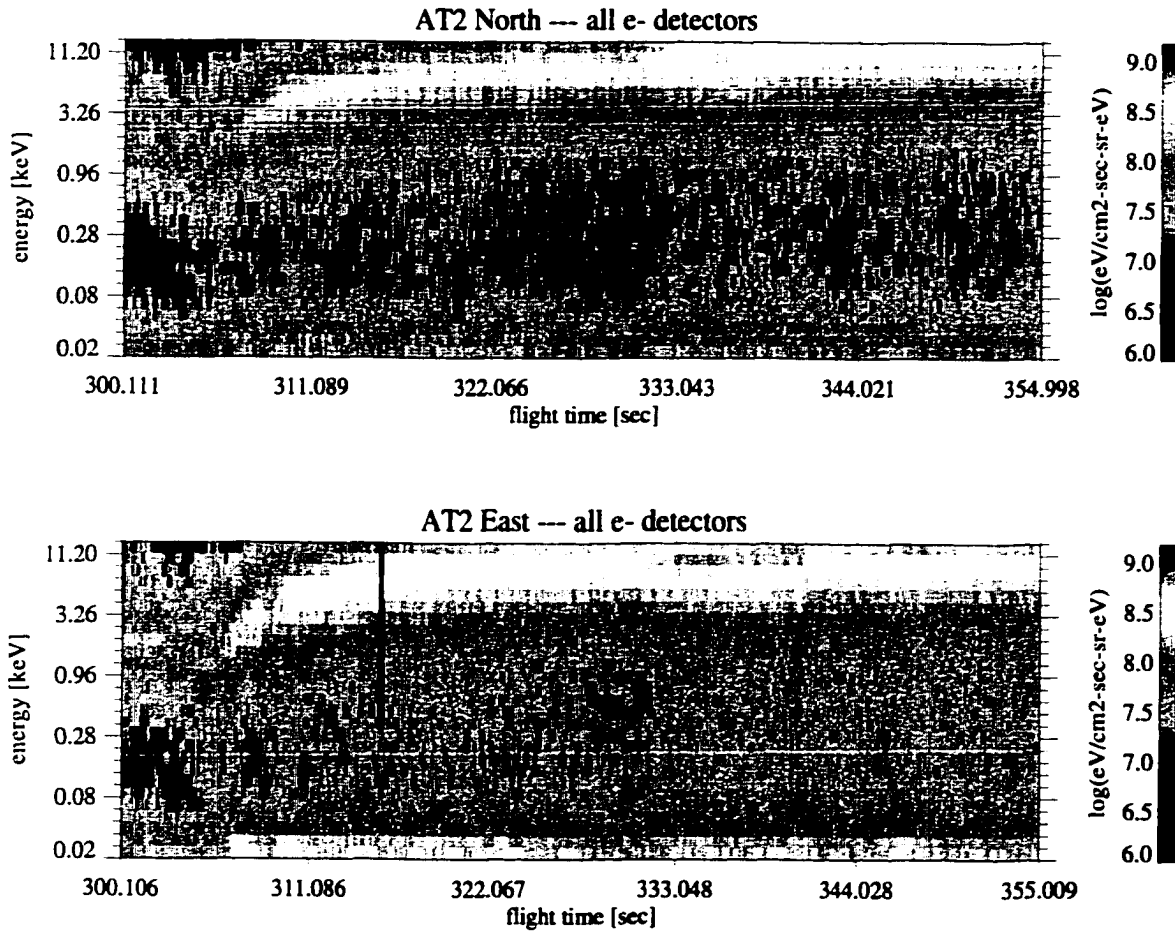


Figure 3-17: North and East payload electron data from T+300 seconds to T+355 seconds.

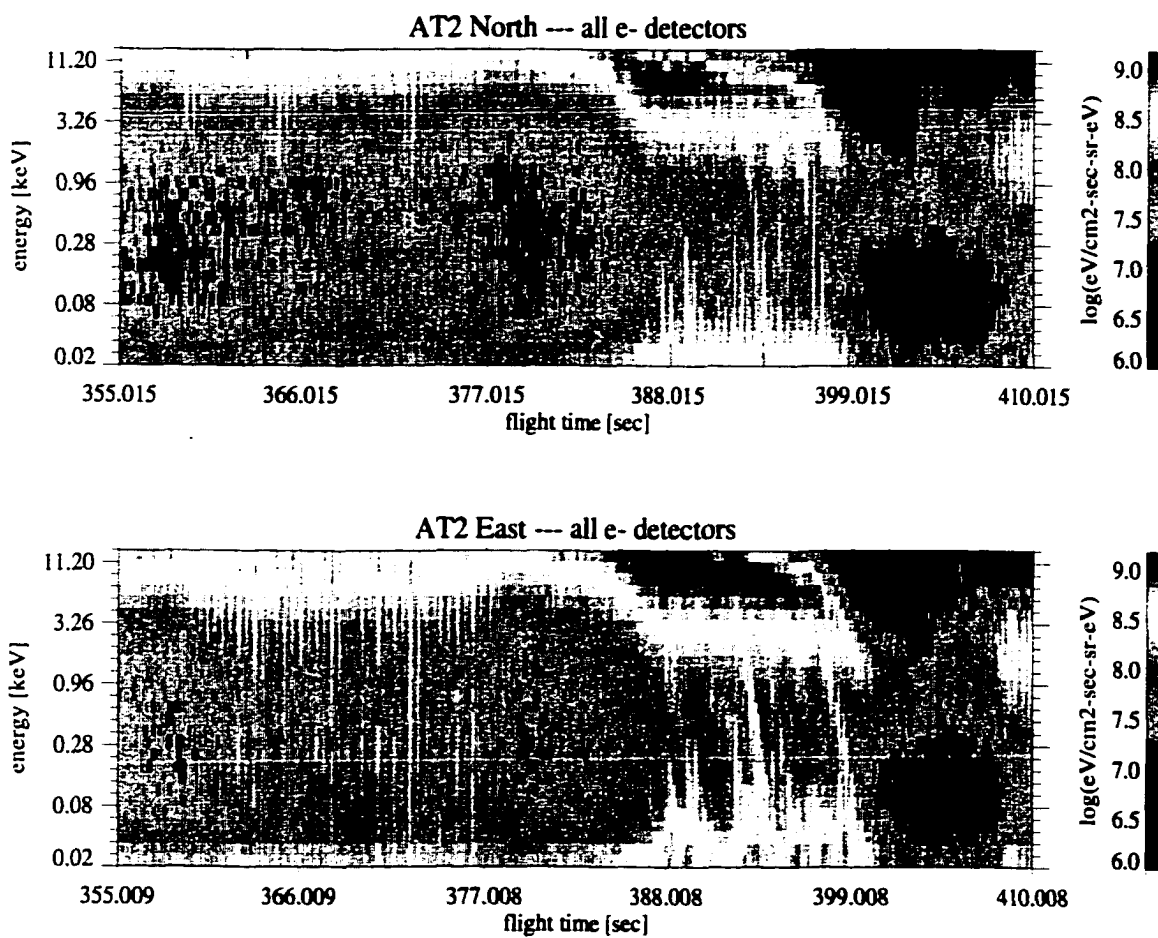


Figure 3-18: North and East payload electron data from T+355 seconds to T+410 seconds.

payloads. The differences between the East and North/Main payloads show that there is a change in electron precipitation along the arc, on scales at least as small as a kilometer.

Another difference can be seen in the region from T+385 to T+400 seconds. Here, there is significant field aligned precipitation, as evidenced by the "bursty" appearance of the electrons at lower energies. This apparent burstiness is caused by the coning of the spin axis of the payload, which causes the apertures of the detector to periodically become poorly aligned with \vec{B} . At higher resolution time scales, not only do these field aligned bursts have temporally dispersive signatures, but they are periodic and their occurrence times are different from payload to payload [Lynch, et al., 1999]. This, along with observing the poleward edge of the precipitation region, distinguishes the motion of the arc relative to the payloads, which is critical for separating spatial events from temporal changes.

3.3.2 HF Data

The high frequency data from the Main payload is presented in Figure 3-15 as a function of flight time [McAdams, et al., 1997]. The faint trace near the top third of the panel is the upper hybrid frequency, while the cutoff above the broader activity is at the Langmuir frequency. The cutoff at the lowest frequencies is instrumental. From these cutoffs, the local plasma frequency, and therefore electron density, can be derived [Baumjohann and Treumann, 1996]. The electron density was determined to be 1100 particles per cubic centimeter near apogee at T+428 seconds, which is a lower density than typically observed on auroral experiments at similar altitudes. It is evident from the plot that the density remains fairly constant over a large time scale, especially from T+300 to T+410 seconds, while the payloads were in, and then exiting, the large arc. This means

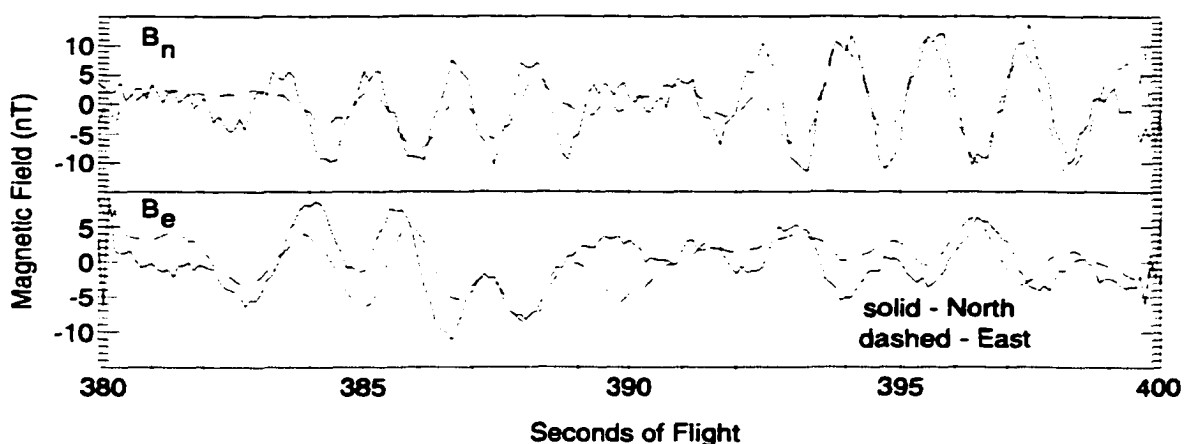


Figure 3-19: Magnetometer data during the dispersed electron event (from *Ivchenko, et al., [1999]*).

that there were no significant depletions or enhancements in the electron density during between T+300 to T+410 seconds, which will have an impact on the data analysis. Finally, the sharp red spikes in the data plot are a function of the automatic gain control of the system and do not represent any physical phenomena.

3.3.3 Magnetometer Data

The data from the magnetometers are used for the attitude solution of the subpayloads. Using the Main payload attitude solution, obtained by the NASA group at Wallops Flight Facility, we can obtain a rough idea of the initial deployment directions of the subpayloads. However, slight changes in the spin frequency and the more important problem of subpayload coning cannot be resolved from the Main attitude solution. We use the magnetometers of the subpayloads to determine actively the angular momentum and angular velocity vectors of the free body motion of the subpayloads. This process of obtaining the correct rotation matrices (attitude solution) for the measured electric field vector quantities

is explained at length in Appendix A. The despinning process has not been optimized to the level that *Ivchenko, et al., [1999]* have used to look at nanoTesla changes in the large baseline signal of the magnetic field, but is more than adequate to discern the fluctuations in the electric field data.

The magnetometers can also provide information on the field aligned currents in the region and electromagnetic wave information. An example of the deviations of the despun magnetometer data is shown in Figure 3-19 [*Ivchenko, et al., 1999*]. The data are shown in a north, east, down coordinate system, with the top panel displaying the north component and the bottom showing the east component. The solid line in each plot is the North payload magnetometer data and the dashed line represents the East data. The fluctuations in $\delta\vec{B}$ indicate a wave in the region, which can also be seen in the electric field data.

3.3.4 Electric Field Data

The electric field experiment is the main focus of this work and provided many challenges and exciting results. One of the largest challenges was the use of the Main payload electric field. Figure 3-20 shows the northward component of the electric field of the Main payload. This data set did not utilize the magnetometer method of despinning described in Appendix A, but instead used the Main payload onboard gyroscope data.

Before T+445 seconds, the electric field data consist of regions of large amplitude spiky structures bordered by small regions that appear similar to the region after T+445 seconds. The spiky signals are caused by the ACS system. Analysis of the ACS firings shows that the regions of strong spikes correlate with the time the argon gas jets are opened to maintain alignment with \vec{B} . This makes most of the data before T+445 seconds relatively useless.

After this time, the gas is depleted. The spiky data, unfortunately, include the time while the payloads passed through the large stable arc that we plan to study. We show this panel to demonstrate the effects of the ACS on the electric field data. We are then left with two payload measurements for the electric field, which cannot yield three dimensional flow fields, but can still separate spatial from temporal events.

Figure 3-21 shows the subpayload electric field components, perpendicular to the magnetic field. Since we measure the electric field perpendicular to the spin axis of the spacecraft, we only measure two components of the vector electric field. The third component is determined by assuming $\vec{E} \cdot \vec{B} = 0$. These three components are then rotated into a coordinate system where the z axis is anti-parallel to the magnetic field. Thus, the z-component of the electric field is zero, and the x and y components are perpendicular to \vec{B} . The x axis is chosen to have no eastward component, so it is northward and slightly upward, due to the dip angle of the magnetic field. The y axis completes the right-handed system, and is mainly westward. When we reference the northward or eastward components of the field perpendicular to \vec{B} , we are referring to these x and y axes, respectively.

In Figure 3-21, the top panel is the northward component and the bottom is the westward component. The black trace in each panel represents the North payload data, and the red line is the East payload data. The regions at the beginning and end of the data sets are not truly valid, as the despinning process used by the magnetometers is subject to edge effects at the limits of the data set. The $\vec{v} \times \vec{B}$ electric field has been removed. The fields are primarily northward and eastward, although for a majority of the flight there is little electric field activity at all. Only in the region of the large arc from T+300 to T+400 seconds is there significant electric field power. This is more evident in Figures 3-22 and 3-23. These

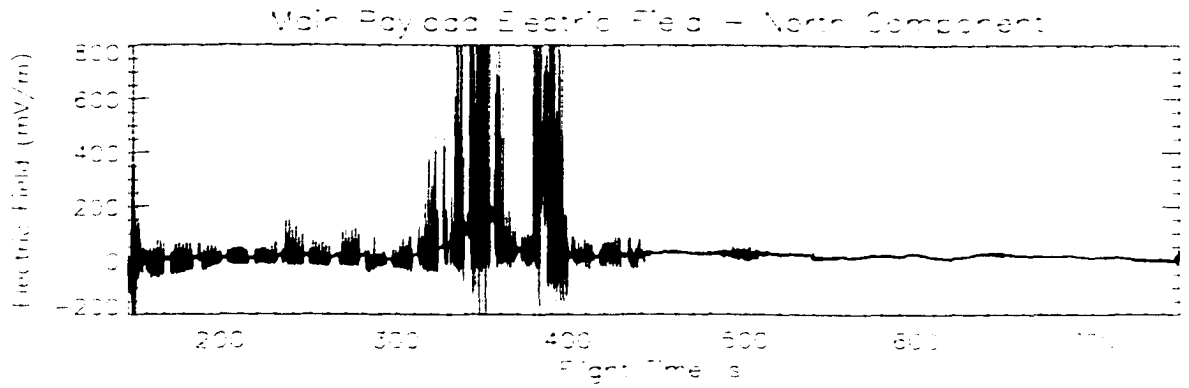


Figure 3-20: Northward component of the Main payload electric field.

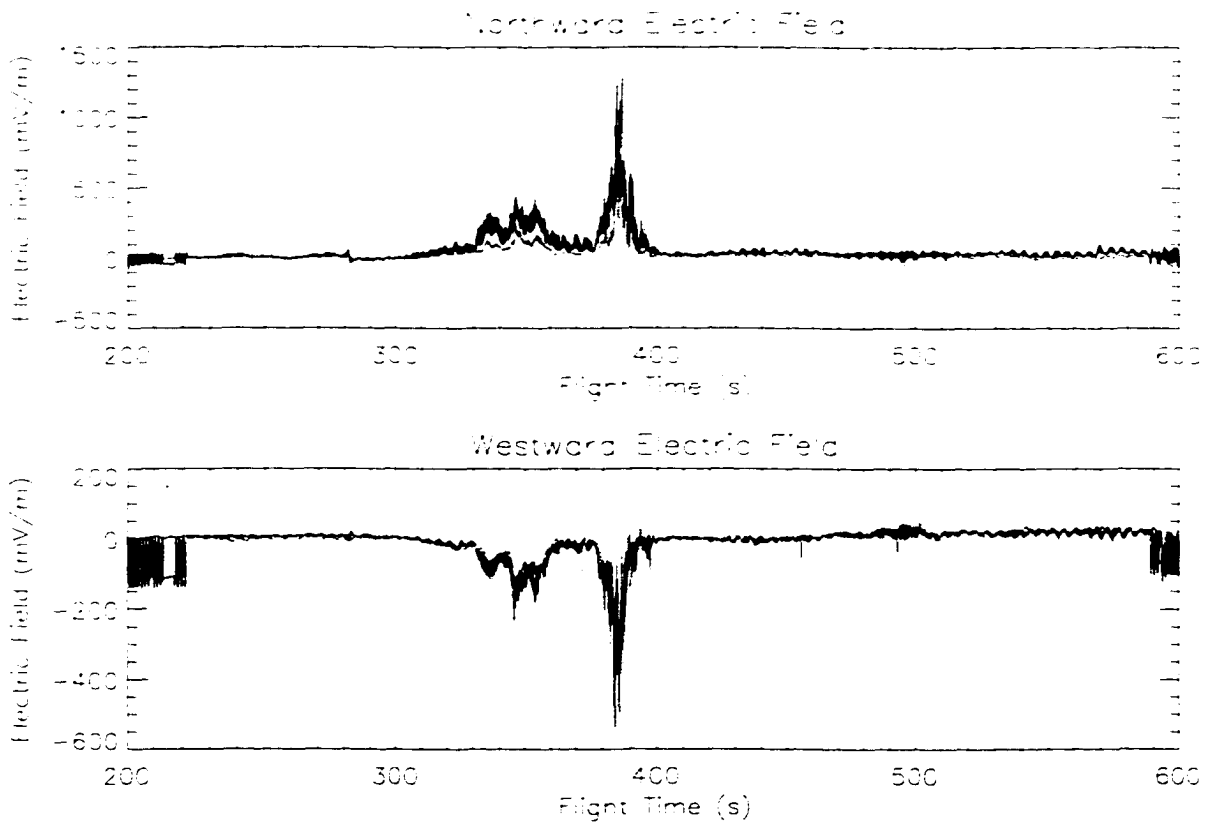


Figure 3-21: Components of the North (black) and East (red) payload electric fields.

panels show the northward and westward electric field components of the subpayloads on an extended time scale. Again, the North payload data is in black and the East payload data is in red.

The residual coning of the payload can be seen in the panels, but it is important to note that each panel has a different vertical scale that accentuates the coning signature. There are no significant differences between the electric fields inside and outside the arc structures before T+300 seconds and after T+400 seconds. The electric field data during the large arc crossing from T+300 to T+400 seconds is remarkable, since a large, northward electric field inside an arc is not among the typical classifications [Marklund, 1984]. Since the region between T+300 and T+400 seconds contains most of the electric field activity, we shall focus there for the remainder of this work.

There are obvious differences in the relative thicknesses of the two traces in each panel. The thickness of the line is due to the magnitude of spikes in the data. The East payload data has significantly fewer spikes, and the spikes are lower in magnitude than the spikes seen in the North payload data. Also, the spikes are most prevalent in regions of electron precipitation. We believe that the spikes are due to a shadowing of precipitating electrons by the payload. A model of this shadowing is provided in Appendix B. The results of modeling are not quantitatively valid, so we cannot use the model to subtract out the effects of the shadowed region. Instead, we take a sliding average of the data and remove the largest of the spikes. This will set an upper bound on the magnitudes of the field strengths that we present for the remainder of this work.

Since the arc is very large in longitude, but relatively small in latitudinal extent, we rotate the electric field data into an arc aligned coordinate system. The three vector elec-

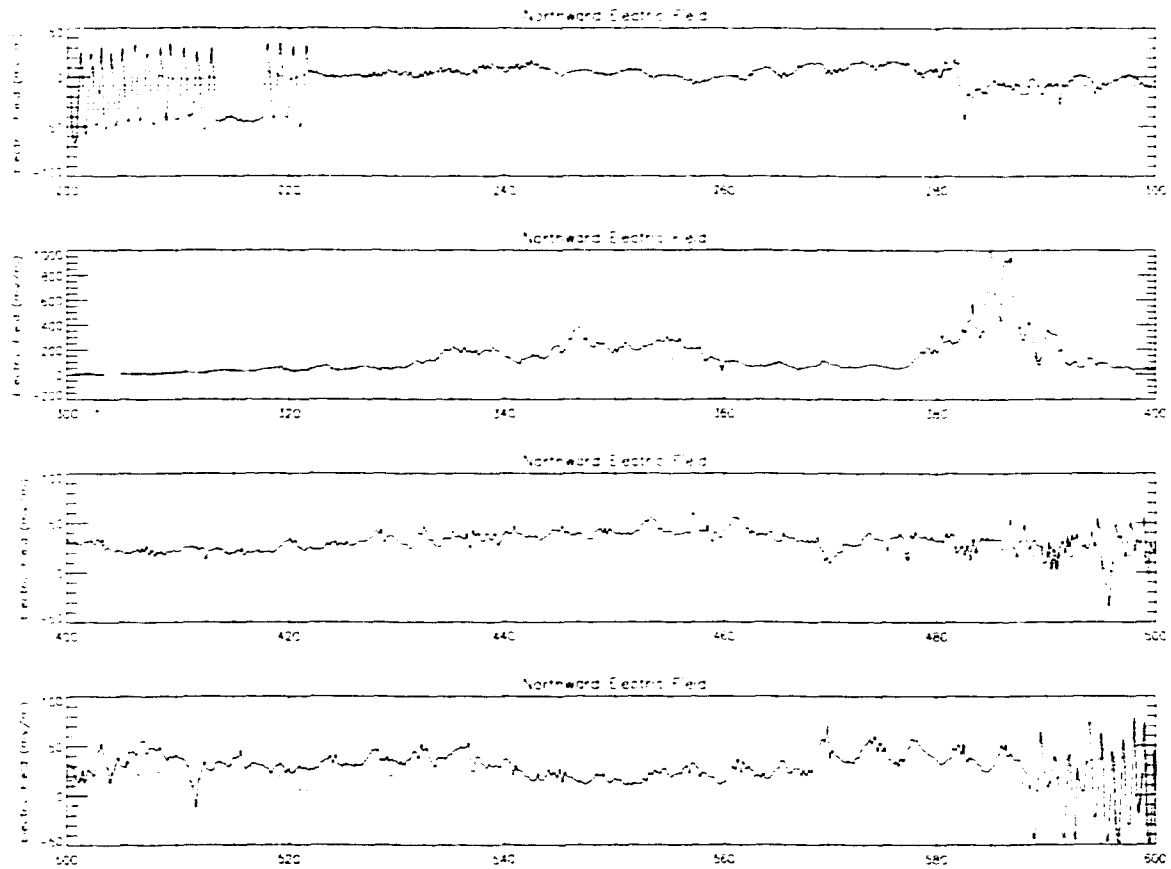


Figure 3-22: Northward electric field component of the subpayloads from T+200 to T+600 seconds (North - black, East - red).

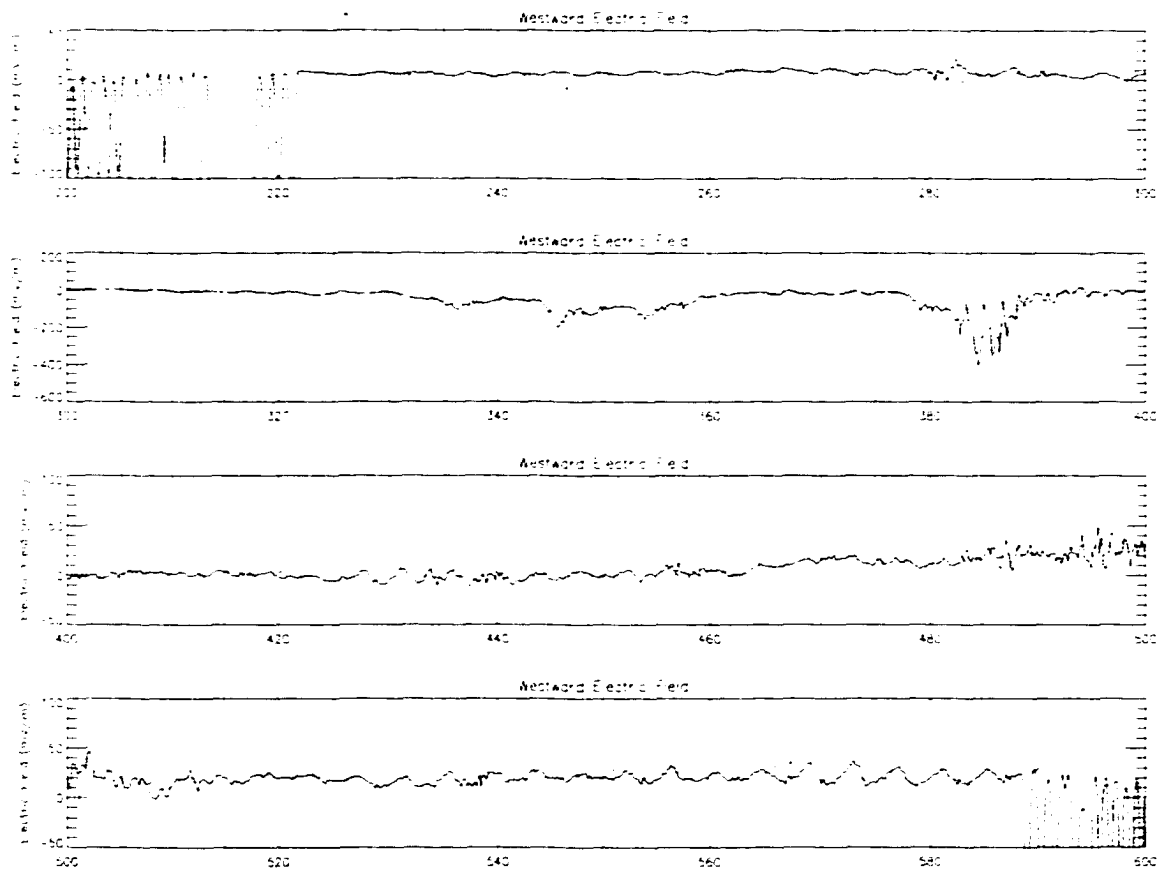


Figure 3-23: Westward electric field component of the subpayloads from T+200 to T+600 seconds (North - black, East - red).

tric field components are arc-normal, arc-aligned, and anti-parallel to \vec{B} . The rotation is performed using the geographic orientation of the large arc seen in the all-sky images. The only distinguishable arc in the all sky images is the one the payloads cross from T+300 to T+400 seconds, so that is the only arc-aligned data presented.

Figure 3-24 shows the arc-aligned electric field components while the payloads are in the large arc from T+300 to T+400 seconds. Figure 3-25 is the electron spectrogram from the North payload data, shown for reference and context. There are several features of note in this figure. One is that the North payload field components are generally larger than the East payload components. This is especially true in the arc-normal component. At first glance, one may assume that this is a result of poor spatial resolution of the all-sky images. The limited resolution would make it difficult to determine if there is a slight change in the arc-normal direction between the subpayloads. One then could imagine a different angle of rotation for the North payload to get to an arc-aligned system. However, this would then increase the arc-normal component, which would augment the difference in the subpayload magnitudes of that component, so it would not explain away the difference. Also, looking at regions where there the electric field magnitude is lower inside the arc, the data between payloads matches extremely well. This is another indication that the angle used to rotate the data into an arc-aligned system is probably correct. *Ivchenko, et al., [1999]* have shown that the orientation of the current sheet of this arc is the same as the orientation of the arc on the all-sky, further reinforcing the reliability of using the camera data to determine the rotation angle. Another reason for the difference in magnitudes could be the shadowing effect discussed above. Although an attempt has been made to remove this using a sliding window average, there may be some effects still present, but they may not be sufficient to

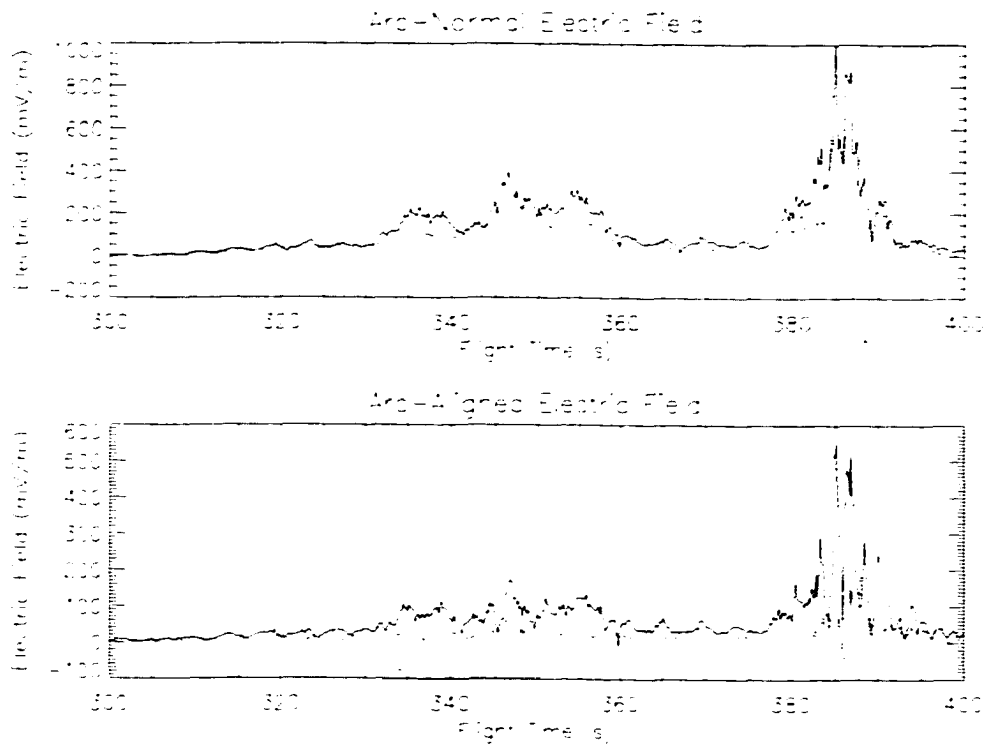


Figure 3-24: Arc aligned electric field components of the subpayloads (North - black, East - red).

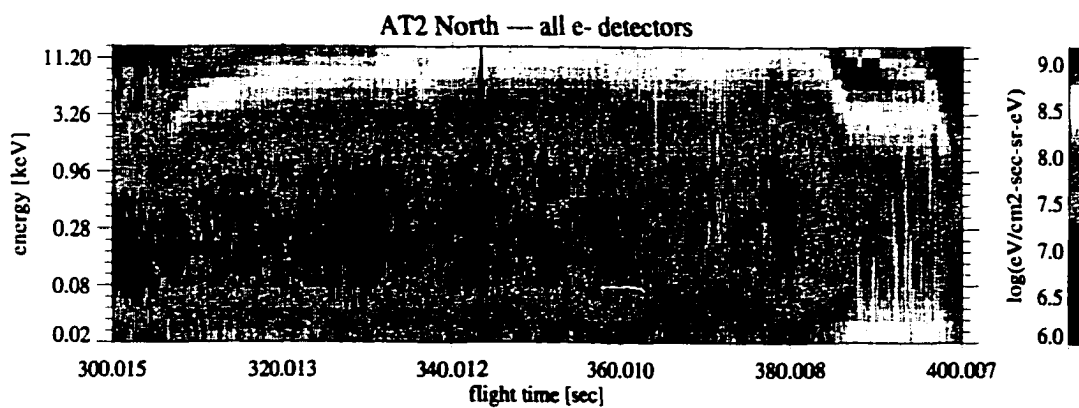


Figure 3-25: Electron spectrogram from the North payload.

explain away the difference in electric field magnitudes.

Another feature is the wave signature seen from T+383 to T+400 seconds. This is the counterpart to the magnetic fluctuation seen in Figure 3-19. Figures 3-26 and 3-27 show the ac magnetometer fluctuations, the ac electric fluctuations of the North payload, and the Poynting flux calculated from the $\delta\vec{B}$ and $\delta\vec{E}$ of the North payload. There is an obvious change in the polarization of the electric wave near T+392 seconds, as the wave is seen in both components before T+392 seconds, but is confined more to the westward direction after this time. A similar polarization signature is seen in the magnetometer data [Ivchenko, et al., 1999]. In both magnetic and electric field data, we observe a periodic wave signature in $\delta\vec{B}$ and $\delta\vec{E}$, with a period of 0.65 Hz. The wave is likely Alfvénic, since the speed of the wave is comparable to the local Alfvén speed as determined by the local density and magnetic field. The method of determining the ac component of the electric field assumes linear superposition of a dc field and the ac oscillation. We are therefore ignoring the effects on the Alfvén wave from the local plasma environment, such as has been considered in work on the interaction between Alfvén waves and small scale density perturbations [Drozdenco and Morales, 1999]. This method will give a first order glimpse of the energy density flow, but the few degrees in phase shift in the electric field that may be present can cause the oscillatory nature of the Poynting flux.

The Poynting flux shows that in the region between T+380 to T+392 seconds, the energy transport, $\delta\vec{E} \times \delta\vec{B}$ is generally upward. This indicates that the Alfvén wave is launched from below the payloads, in the lower ionosphere, and moves upward through the arc structure between T+380 to T+392 seconds. The waves do not originate in the magnetosphere and enter and reflect from the ionosphere, but may be generated due

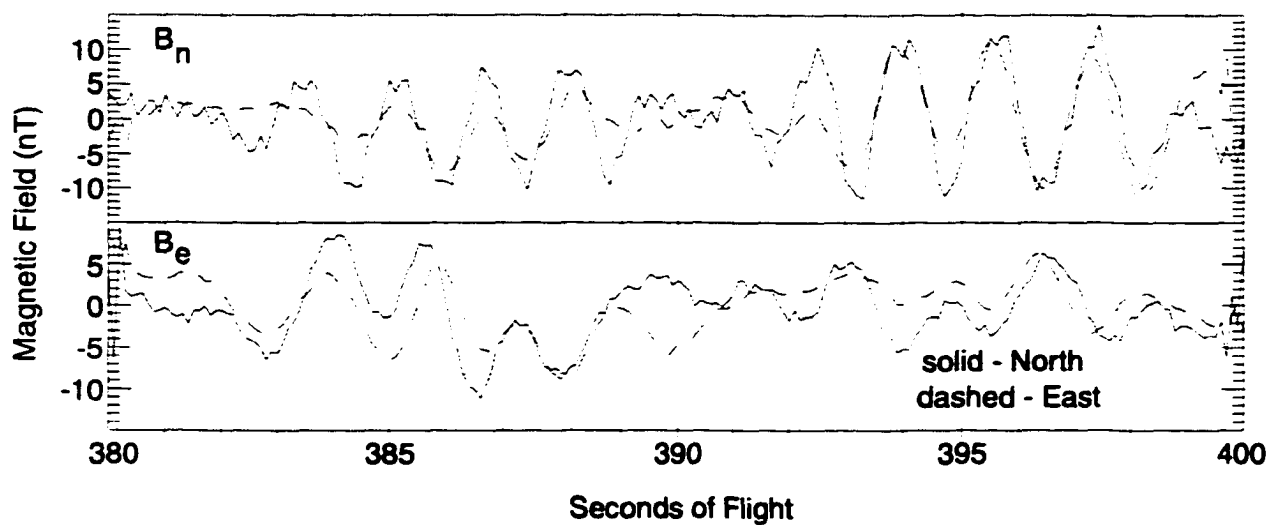


Figure 3-26: Oscillations in the magnetometer data (from *Ivchenko, et al., [1999]*).

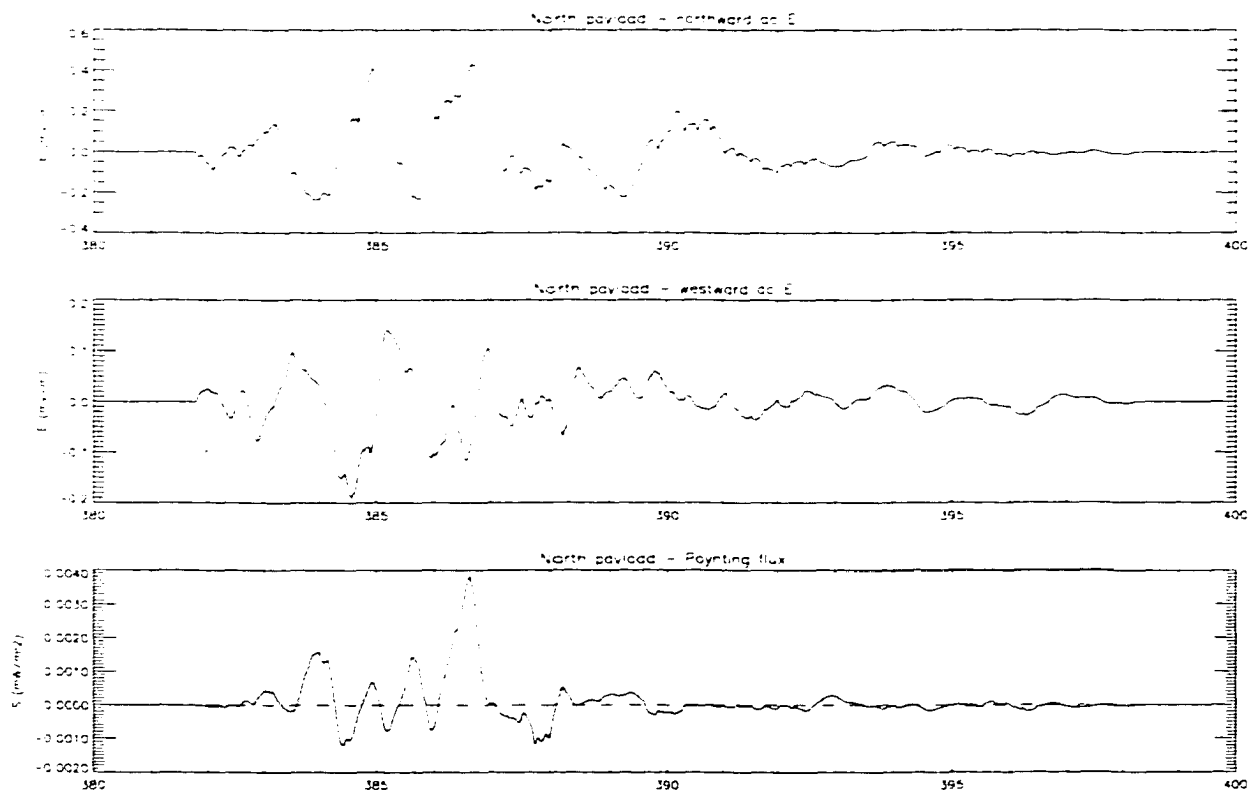


Figure 3-27: Oscillations in the electric field data and the calculated Poynting flux from $\delta\vec{E} \times \delta\vec{B}$.

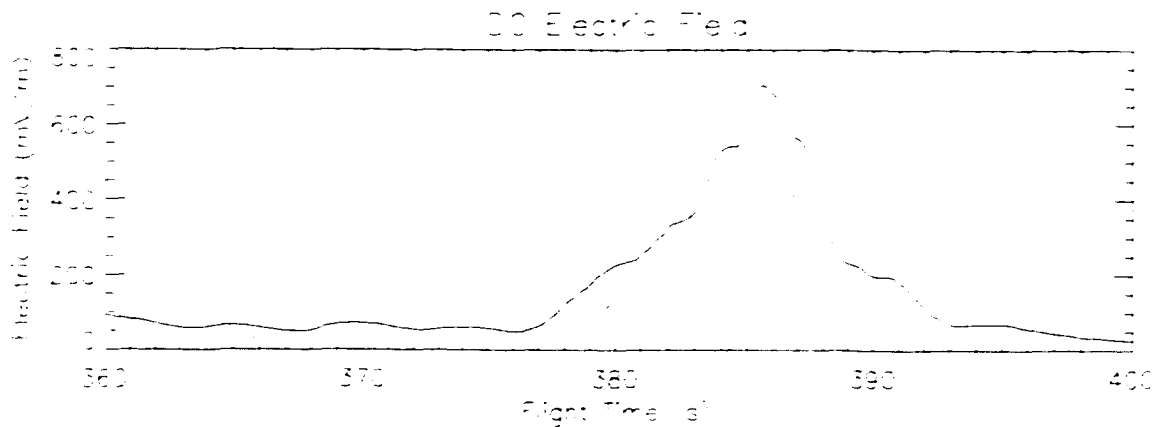


Figure 3-28: Arc aligned electric field components of the subpayloads (North - black, East - red).

to gradients in the ionospheric conductivity. The DE-2 satellite observed regions of upward Poynting flux, although it was either small ($< 1 \text{ mW/m}^2$), or in a region with net downward flux [Gary, *et al.*, 1995]. The FREJA and FAST satellites have also seen upward fluxes of electromagnetic ion cyclotron waves [Erlandson and Zanetti, 1998, Chaston, *et al.*, 1998]. Recent work has been done to show that localized electric fields, transverse to the magnetic field, in the ionosphere can spontaneously generate upward traveling electromagnetic waves [Peñano and Ganguli, 1999].

From T+392 to T+400 seconds, there is no apparent preference for an energy flow direction. This can be a result of wave interference due to reflections in an Alfvén resonator cavity [Lysak, 1991]. The reflection occurs between the local Alfvén speed maximum and the conductivity gradients in the lower ionosphere, which would produce a signature of wave interference. Detailed analysis of this wave event is explained by Ivchenko, *et al.*, [1999].

The last feature is simply the size of the electric field in this large arc. The vector electric field reaches a peak magnitude of 1 V/m, although that magnitude also includes the oscil-

lation signature of the Alfvén wave. Even in the T+330 to T+360 region, the field strength reaches over 400 mV/m. These values are not only high for experiments in the entire ionosphere, but are rarely seen at the relatively low altitudes of AT II [Boehm, et al., 1990]. Figure 3-28 shows the dc arc-normal component of the subpayload electric fields. Here, all ac components of the electric field data over 0.5 Hz have been filtered out from the data. The peak value of the field in the arc-aligned direction is lower, but is still substantial for both payloads.

3.3.5 LF Wave Data

Figures 3-29 and 3-30 show the Fourier spectrum of the electric field data from T+200 to T+600 seconds. The intensity is defined by the color bar in each panel. The white line in each figure is the total integrated power as a function of time. The vertical scale on the right of each panel show the magnitude of this power.

Both figures show that the majority of electric field wave power is in the region of the large, stable arc structure from T+300 to T+400 seconds. There is also some wave power after 400 seconds, although the electric field magnitude is negligible. Figures 3-31 and 3-32 show enlargements of Figures 3-29 and 3-30 from T+360 to T+400 seconds. Both payloads see regions of heightened broadband wave activity from dc to approximately 100 Hz. Figure 3-33 shows the average intensity of the wave spectrum from the East payload from T+385 to T+386 seconds as a function of frequency. FFT analysis of the magnetometer data show no ULF wave frequencies present at any time, demonstrating the electrostatic nature of the observed waves in the electric field data.

Having displayed all of the particle, magnetometer, dc electric field, HF, and ULF

wave data, and the local and global auroral environment, we are now able to investigate the physics underlying our many observations. In Chapter 4, we discuss the scientific implications of our measurements and ultimately begin to touch upon the richness of this multiple payload data set.

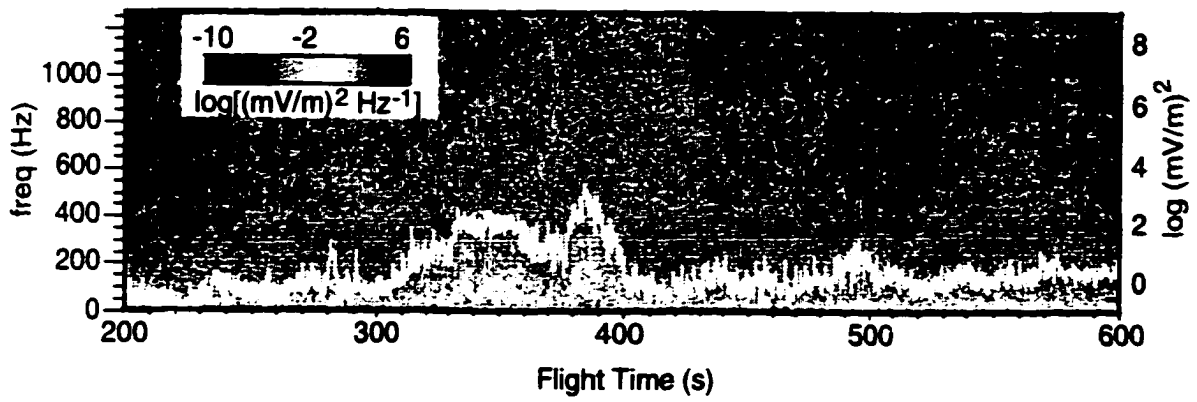


Figure 3-29: Survey plot of low frequency data from the North payload.

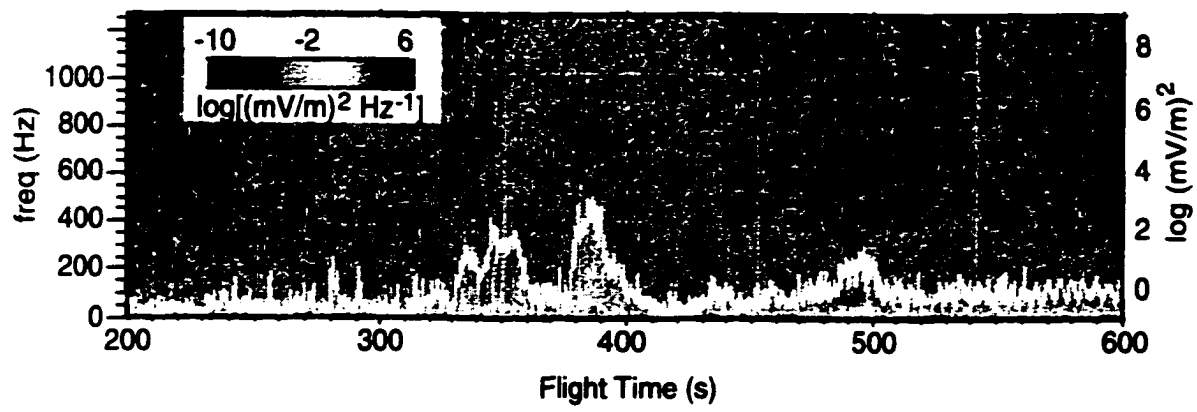


Figure 3-30: Survey plot of low frequency data from the East payload.

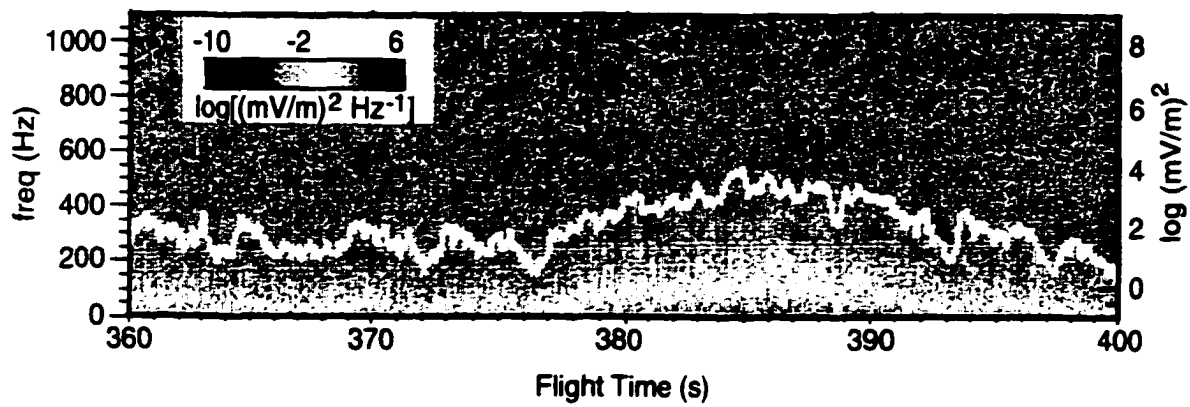


Figure 3-31: Plot of low frequency data from the North payload.

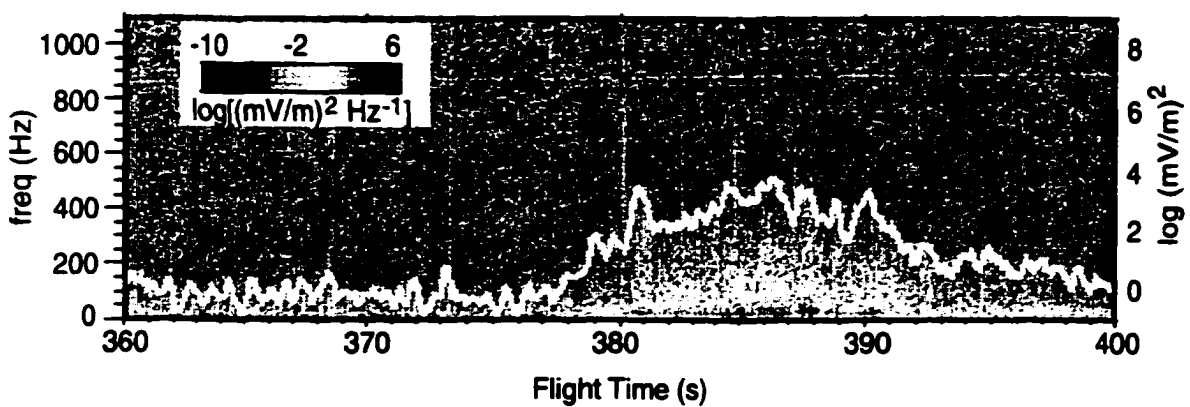


Figure 3-32: Plot of low frequency data from the East payload.

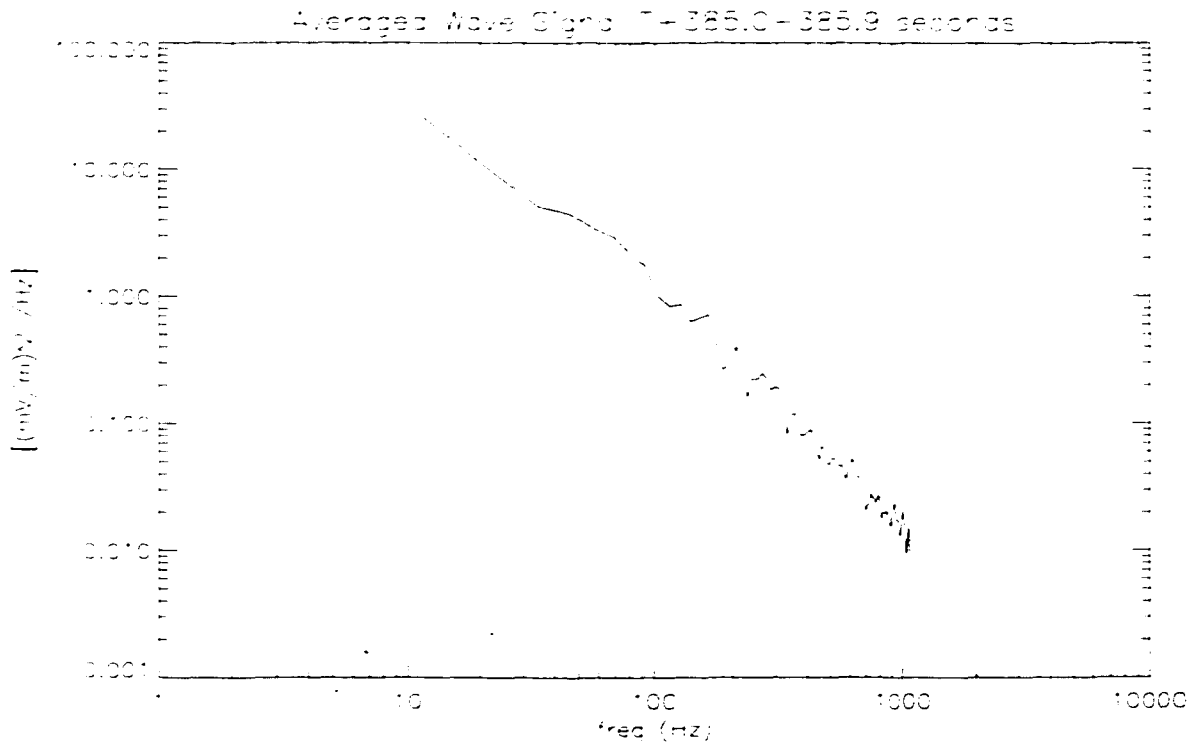


Figure 3-33: Average wave intensity from T+385 to T+386 from the East payload.

Chapter 4

Science Discussion

The focus of this thesis is an investigation of the poleward edge of the large, stable arc traversed from T+300 to T+400 seconds. Three point measurements in this region of large dc electric fields and electrostatic wave power can resolve spatial gradients from temporal changes. The fields and waves power have inherently interesting properties as well. Our discussion will be broken into three parts. First, we investigate the magnitude of the observed electric field. Second, we look at separating space and time in the data set. Lastly, we discuss the interpretations of the measured broadband electrostatic waves.

4.1 Implication of Electric Field Magnitudes

An obvious feature in the electric field data is the lack of any substantial electric field for a majority of the flight, as evident in Figures 3-20 and 3-21. Most electric field values are less than 10 mV/m before T+300 seconds. After T+400 seconds, the electric field does not exceed roughly 30 mV/m. Figure 3-14 shows a significant amount of auroral activity that the payloads passed through from T+200 to T+300 seconds, and from T+400 to T+600 seconds. The all-sky images from T+200 to T+300 seconds show some low intensity arcs, and the auroral forms from T+400 to T+600 seconds are mainly subvisual or wispy. The lack of electric field in the presence of precipitation can be associated with the wake of westward expanding, enhanced aurora, also termed a westward traveling surge. Figure 3-10 shows the passage of a westward traveling surge in the trajectory region, between 0825 and

0838 UT. The increased conductivity that is associated with intense electron precipitation can effectively short out any electric fields that attempt to form in the ionosphere. The Freja satellite has shown that low magnitude electric fields and auroral forms lacking much structure can be observed in the surge wake [Marklund, et al., 1998]. The electric field measurements from AT II appear to support the same conclusions, when viewed in the context of the global auroral environment.

This scenario of the surge wake region seems to be in direct conflict with the extremely large electric fields seen in the regions between T+330 to T+360 seconds and T+380 to T+390 seconds. The large dc electric fields seen in the first region, reaching a maximum of 400 mV/m on the North payload, are seldom seen at 500 km altitude, and the 700 mV/m dc electric field of the second region from T+380 to T+390 seconds is among the highest fields recorded at such low altitudes. Typical rocket experiments at similar altitudes measure dc electric fields in the several tens of mV/m range.

One explanation for the large fields could be an error in the dc electric field measurement. Calibrations of the spheres showed no anomalies, and there are no known gain vs. amplitude errors associated with the op-amps used. This may not have been true if the amplifiers had saturated, but analysis of the raw electric field data clearly shows that the preamplifiers in the potential spheres did not saturate. An underestimate of the electric field could occur, especially in the very low density (1000/cc) environment traversed by AT II, if the spin period were smaller than the RC time constant of the electronics [Boehm, 1999]. However, it is extremely unlikely to overestimate the fields due to an electronics error.

Next, we note that the raw data waveforms of the electric field are nonsinusoidal. This is best seen in Appendix B, Figures B-7 and B-8. As we note in Appendix B, this may be

due to a shadowing of the potential sphere by the payload body. Since the North payload spin axis is tipped at a greater angle with respect to the magnetic field, a greater physical shadow would be produced. The larger shadow would produce a greater shadow effect than the East payload would observe, and the measured data clearly reflects this feature. Although we cannot fully model the shadow region accurately enough to remove its presence from the data, it is evident that the shadow has an effect on the observed electric field. Since the actual Debye lengths in a plasma are rarely equal to the theoretical predictions, the inability to produce a quantitative model could be a result of being unable to model the in-situ Debye shielding. The shadowing could cause the measured electric field magnitudes to be artificially larger than the actual fields by a factor of two on the North payload, and somewhat less on the East payload (see Appendix B for more details). Therefore, the large fields observed may be a result of this shadowing. If we assume the factor of two increase in the electric field, this would then indicate that the peak dc electric fields that we measure are on the order of 350 mV/m. This is significantly smaller, although still substantial. Although analysis of the Main payload data is difficult, it can be seen, when the ACS is not firing, that the electric fields observed are no larger than a factor of two smaller than the East payload data, and often are in good agreement. Unfortunately, the times that the ACS is not on are few and far between, but this does indicate that the East payload data is perhaps a good representation of the actual electric field environment. This would still indicate dc electric field magnitudes in excess of 300 mV/m. This magnitude is certainly possible, but might also be too large when viewed in parallel with magnetometer results presented next.

At the altitudes reached by the AT II payloads, the electric fields measured are generally

presumed to be the convection fields and not the auroral acceleration fields. We now must test that presumption. We can go back to Equation 1.1.4 to determine the amount of field aligned current that should flow along field lines in order to close the current due to the perpendicular electric field in the conducting ionosphere. By using the electron precipitation data, we can infer values for the Pedersen and Hall conductivities [Reiff, 1984]. These values are shown in Figure 4-1. The inferred Pedersen conductivity for the North and East payloads are shown in the top and middle panels, respectively, and the inferred Hall conductivity for the East payload is shown in the bottom panel.

The spatial derivatives can be written as:

$$\bar{\nabla}_{\perp} = \frac{\partial}{\partial a_{\perp}} = \frac{\partial}{\partial t} \frac{\partial t}{\partial a_{\perp}} = \frac{1}{v} \frac{\partial}{\partial t} \quad (4.1.1)$$

where a_{\perp} is the direction perpendicular to the arc, v is the velocity of the payload perpendicular to the arc, and we assume that there are no spatial gradients parallel to the arc. The gradient in the arc-normal dc electric field, as measured by the subpayloads, is ten times the gradient of the arc-aligned dc field, a fact that shall enter into our later calculations. Using the observed values of the electric field perpendicular to the arc from the East payload, we can derive the expected field aligned current which is shown in Figure 4-2.

Figure 4-2 shows that the currents required (to maintain the gradients and intensities in the conductivity and electric field) reach 15 mA/m^2 . Analysis of the onboard magnetometers reveal currents reaching $3 \text{ } \mu\text{A/m}^2$, a factor of 5000 less than the predicted currents. Of the three terms in Equation 1.1.4, the first, $\Sigma_P(\bar{\nabla}_{\perp} \cdot \vec{E})$, is the dominant term, a factor of 2.5 greater than the next largest term, and a factor of over 16 larger than the smallest term. The gradient of the electric field appears to be the driving force behind the large predicted

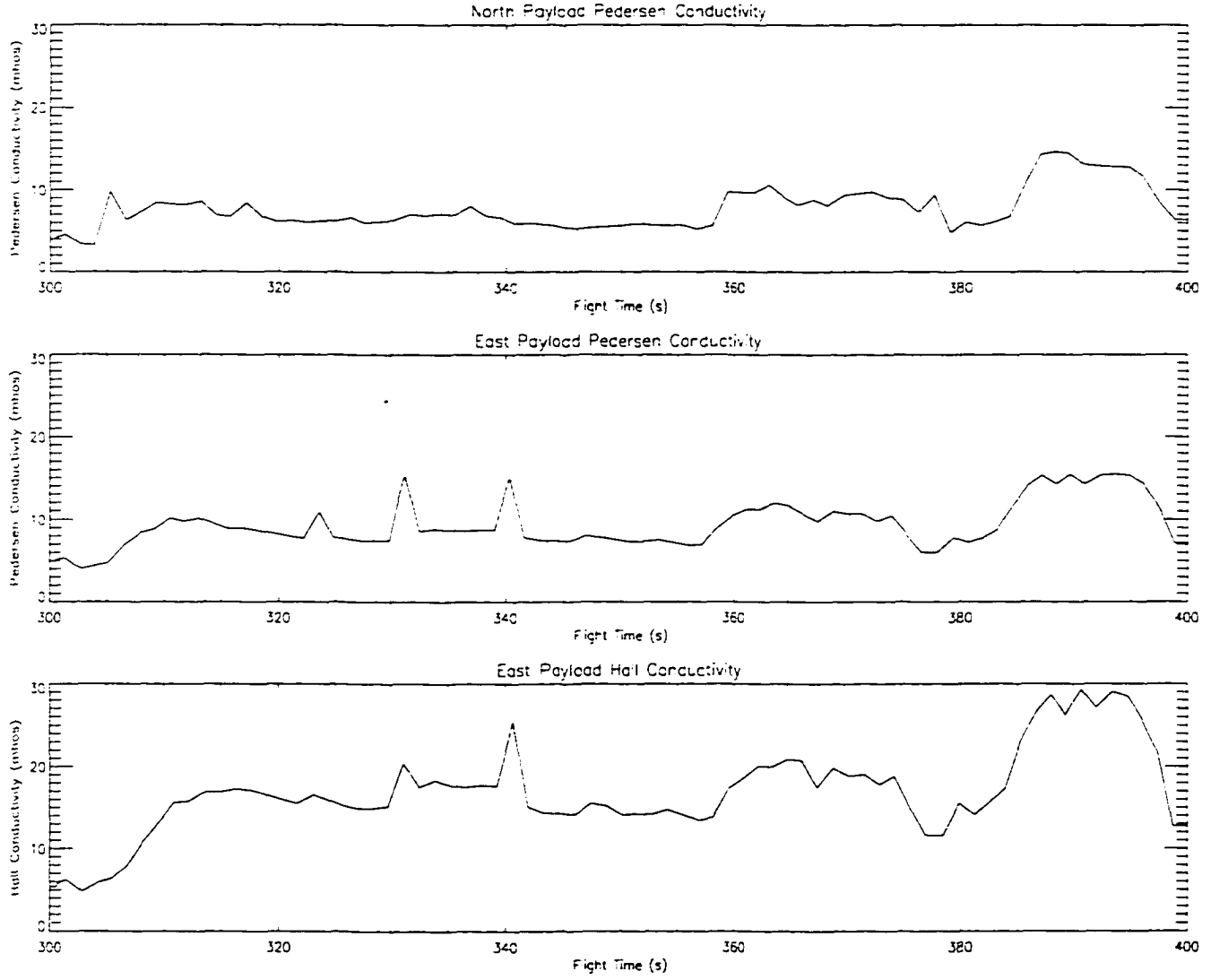


Figure 4-1: Inferred conductivities from electron precipitation.

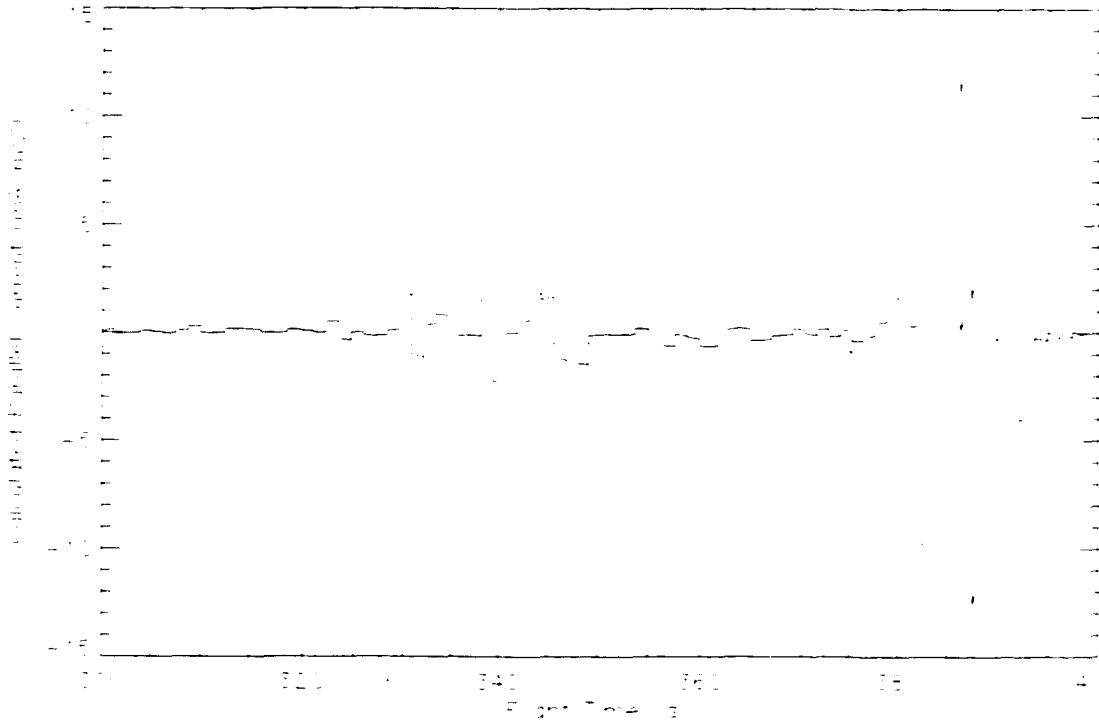


Figure 4-2: Calculated field aligned current from East payload data.

currents.

If we now go back to our assumption about the field magnitudes being incorrect by as much as a factor of two, we can reevaluate these currents. This factor of two was for the North payload, so using the East payload data and this factor of two will set a lower bound on the expected field-aligned currents. A lowering of the East payload dc electric field by a factor of two will change the overall slopes in the gradient of the electric field such that the $\Sigma_P(\vec{\nabla}_\perp \cdot \vec{E})$ term decreases by the same factor of two. Again, the dominant term is the gradient of the electric field, not the absolute magnitude. This decrease is obviously far short of the factor of 5000 needed to have the magnetometer results agree with the predicted currents. Therefore, if we are truly measuring the spatial gradient of the convection field,

the currents are not sufficient. Even if the currents are closed over a region of space, the currents integrated over the entire arc still fall well short of supplying the needed closure.

Therefore, we can conclude that perhaps we did not measure the convective electric field. Alternatively, the payloads could have been inside the auroral potential structure. We must now test this hypothesis. The peak electron energy of the auroral beam is measured to be near 14 keV for all three payloads during the arc crossing. If we integrate the electric field across the payload trajectory, as a measure of the total potential drop the particles experience, we obtain a value of 4.7 kV. If the payloads were inside an inverted-V potential structure, there would be a 4.7 kV potential below the payloads, since the potential would have to reduce to zero before reaching the highly conductive ionosphere. If the payloads were in the acceleration region, we should also have seen upward flowing ion beams with energies near 4.7 keV that have been accelerated by this potential below the payloads. We also would expect to see a converging electric field shock structure and a density depletion region if the payloads were inside the downward current region potential structure, as seen in numerous passes on the FAST satellite [Ergun, *et al.*, 1998]. The ion data do not show any indication of a 4.7 keV ion beam that would be expected, even though the data are heavily contaminated with electron counts. The payloads measure a unidirectional electric field and no change in the density, as seen in Figures 3-16 and 3-15.

Analysis of field aligned dispersive electron precipitation indicates the possibility that the potential structure responsible for acceleration of the observed electrons is moving vertically up the field line as a function of time [Lynch, *et al.*, 1999]. The dc electric field measurements indicate a temporal decrease in intense electric field at the time when the potential structure is thought to be moving upward (see next section). This could account

for the lack of an observed diverging field signature if we are indeed in an inverted-V potential structure. The potential structure might move above the payloads before the payloads have crossed into the other side of the potential structure. We would also loosen the size of density depletion that should be observed, since the payloads would never cross into the other side of the potential structure. This also would explain why there is continued precipitation after the electric field falls back to ambient levels, since the payloads would now be under the acceleration region and the potential structure would be isolated from the probes. As the potential structure moved up in altitude, the payloads would be measuring the bottom of the inverted-V region where equipotential contours could be more spaced out, so the payloads would observe a decrease in the observed electric field. However, we would also expect the observed precipitating electrons to have fallen through the entire potential structure. The payloads would then observe an increase in the peak energy of the precipitating beam at this location. For most of the arc crossing, the peak energy of the beam is above the upper threshold of our particle detectors. In this region of time of upward motion the beam energy is decreasing as seen in Figure 3-18. Although it is not conclusive, we are probably not observing this expected increase. This evidence, when viewed in full, makes it difficult to accept the possibility that we are inside an inverted-V potential structure.

However, inverted-V potentials are not completely sufficient to describe many of the particle data observed in rocket experiments [Mozer, 1981]. Oblong structures and S shaped potentials are also possible characterizations for potential field lines [Mozer, 1981, *Temerin, et al.*, 1981, *Boehm, et al.*, 1990, *Kimball and Hallinan*, 1998]. Combinations of S shaped potential structures and inverted-V structures can also develop. Based on the observed data, we present a possible scenario for this arc crossing, shown in Figure 4-3.

Here, we have a combination of an inverted-V potential and an S shaped potential pattern. Since the payloads would be crossing equipotential lines that do not map to the ionosphere, substantial field aligned currents would not be required. The equipotential lines of the S shaped structure would spread apart as a function of decreasing altitude, such that low dc electric fields would be seen at the altitudes where the conductivity is the highest. The inverted-V and S shaped regions may be tied together such that the upward motion of the inverted-V may cause the S region to move upward as well, explaining the temporal decrease in electric field magnitude. The S potential might not contribute much to the acceleration of the precipitating electrons, and therefore might not contribute much to the upward acceleration of ions, depending on the exact shape of the S structure. Most of the acceleration could occur at higher altitudes or lower latitudes in the S shaped region, but the inverted-V region that is well above the payload is still required to support the electron data. Passing through an S shaped potential structure would also result in measuring a unidirectional electric field. The S shaped potential lines could fan out over a large distance, and spread poleward enough to enter the ionosphere in the polar cap. This would greatly reduce the conductivity which would reduce the $\Sigma_P(\vec{\nabla}_\perp \cdot \vec{E})$ term by at least an order of magnitude.

After consideration of all of the parameters, the data appear to support the following scenario. The lack of significant electric field power in the majority of the flight supports the premise that the payloads were in a region of enhanced conductivity due to the passing of a westward traveling surge. There is, however, a large region of extremely large dc electric field. The shadowing of the potential spheres might give electric field values that are as much as 50% higher than the actual electric field, as described in Appendix A. Factoring

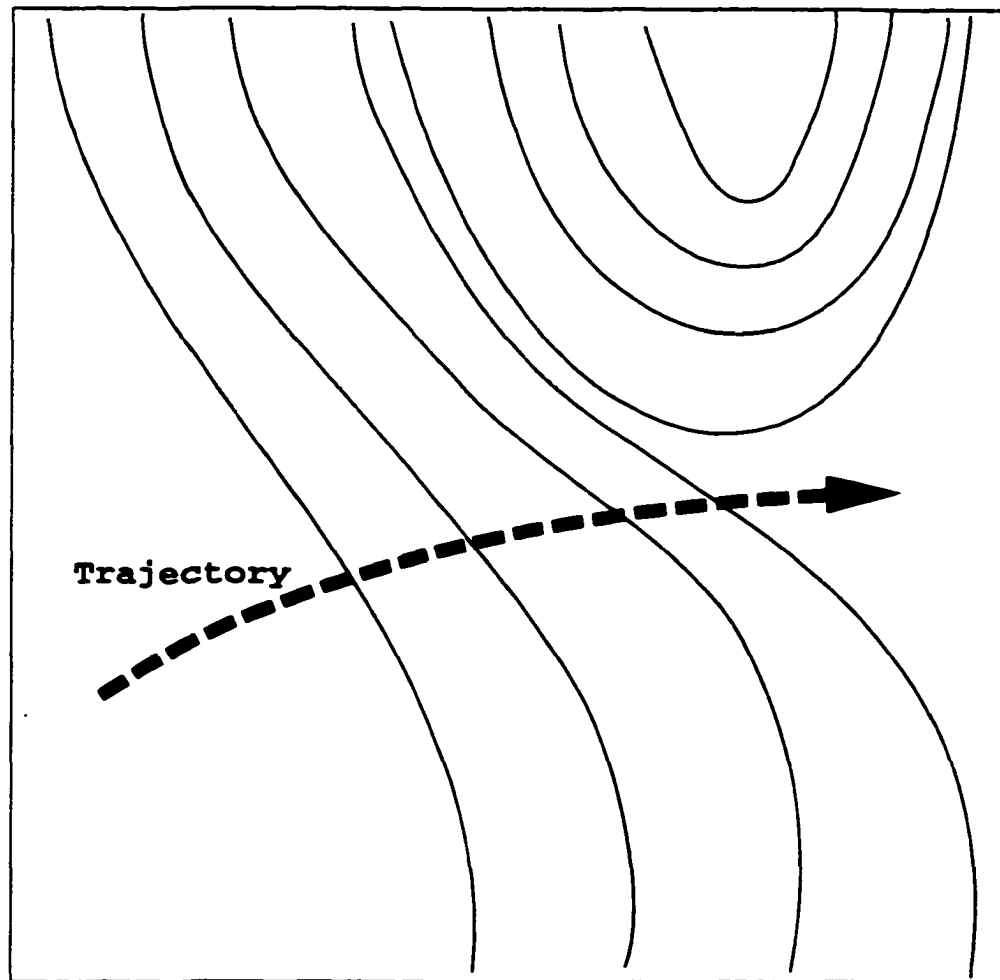


Figure 4-3: Possible potential lines during arc crossing. Geographic north is to the left of the figure, altitude increases vertically.

in this decrease, the electric field magnitudes are still inconsistent with the assumption that the payloads are measuring a convection electric field, based on the low measured field aligned currents. Although the large dc electric field region has a temporal component, there is also a definite spatial gradient that cannot be supported by the observed currents. It appears likely that from T+300 to T+400 seconds the payloads were passing through an S shaped potential structure that was below an inverted-V structure. The magnitude of the dc electric field would be plausible if the payloads were inside such a potential structure,

and large currents would not be required if the S shaped potential lines entered the polar cap. The inverted-V and S shaped structures moved upward in altitude when the payloads were at the poleward edge of the arc, causing a temporal decrease in the magnitude the large electric fields. The lack of density depletions and the measured unidirectional electric field also agree with a payload passing through an S shaped potential structure.

4.2 Temporal and Spatial Considerations

The electric field measurements provide important information about the motions of the arc structures the payloads traversed. Three point measurements can yield information about the spatial and temporal characteristics of the movement. The AT II payload particle and electric field data can be used to determine these motions. In *Lynch, et al. [1999]*, the stable arc that the payloads crossed from T+300 to T+400 seconds was shown to be drifting slowly northward at 500 m/s. This determination would not be possible from a single payload measurement. Since our electric field data are in an arc-aligned coordinate system, we can subtract out the relative arc motion to help separate temporal events from spatial changes. We shall first investigate the regional characteristics of the high dc electric field region, and then determine a possible explanation within the framework of the visual arc observations.

Figures 4-4 and 4-5 show the cross correlation between the dc electric fields from the two subpayloads. The cross correlation is given by

$$P_{xy}(L) = \frac{\sum_{k=0}^{N-L-1} (x_k - \bar{x})(y_{k+L} - \bar{y})}{\sqrt{[\sum_{k=0}^{N-1} (x_k - \bar{x})^2][\sum_{k=0}^{N-1} (y_k - \bar{y})^2]}} \quad (4.2.1)$$

where x and y are the sample populations, and L is the lag between the populations. The

result of the correlation, P_{xy} , is the correlation coefficient, which is a direct measure of how well the sample populations vary together. The correlation is carried out by taking a window of data from one population and adjusting the lag between the other population. In the bottom left of each figure are the two times, in seconds of flight time, that make up the beginning and end of the sliding data window. The number to the right of these indicates the time where the correlation coefficient reaches a maximum during this time interval. If the start time of the window matches exactly the maximum correlation time, the event is considered to be temporal. Deviations of the maximum time from the start time of the sliding window can indicate a spatial variation. In these figures, the correlation coefficient is plotted as a function of the lag. The horizontal scale is represented as seconds of flight time. In a given plot, the start time of the sliding window must be subtracted from each flight time value to determine the lag. For example, the lag in Figure 4-4 at a flight time of 370 seconds is 1.25 seconds. A correlation confidence line is overplotted on each figure. This demarcation is set at 0.8, which represents the three sigma confidence line, or the value above which a correlation coefficient can be interpreted confidently as an accurate correlation. It should also be noted that negative correlations are possible, and a correlation coefficient less than -0.8 would indicate a strong anti-correlation. A high degree of correlation or anti-correlation merely indicates that the two data sets fit well with a positive or negative linear model.

Figure 4-4 shows the correlation between the payloads for the increase in the electric field magnitude, from T+368 to T+385 seconds. The high correlation value shows that both of the payloads see a similar rise in field magnitude. The broad level of high correlation makes it difficult to determine exactly a time shift between the onsets of the increase. The

time given by the maximum in correlation coefficient indicates a time lag of 1.25 seconds for the East payload. This means the rise in electric field occurs first at the North payload and then later at the East payload, which could indicate passing through an arc-aligned boundary. The main point is that the maximum correlation does not occur at zero lag, indicating that this event is not purely temporal. We will revisit this in a moment, and determine a more exact delay time by looking closer at the electric field data, but for now we turn our attention to Figure 4-5.

Figure 4-5 shows the correlation between the dc electric fields from T+385 to T+392 seconds. The first notable feature is the relative narrowness of the coefficient maximum when compared with Figure 4-4. Also, the delay time is zero, at least to within the resolution of the data set being used, as seen by the match between the window start time and the maximum correlation time. This indicates that the decrease in electric field is a purely temporal event. The fast plasma motion that characterized the first region of time from T+368 to T+385 seconds wanes with a decrease that must be constant over at least 1 km. We therefore characterize this time region as purely temporal, and now look more closely at the previous region to better determine the characteristics there.

We present again the electric field data from the three payloads in Figures 4-6 and 4-7. Figure 4-6 is the total measured electric field, and not the purely dc component as seen in Figure 4-7. The ACS firings on the Main payload make it difficult to subtract out the ac components, and Figure 4-6 shows how little data can be used from the Main payload electric field experiment. Upon closer examination of the region of time between T+368 to T+385 seconds, the Main payload appears to see an increase in the electric field, although the magnitude cannot be determined. This can be seen in the difference in

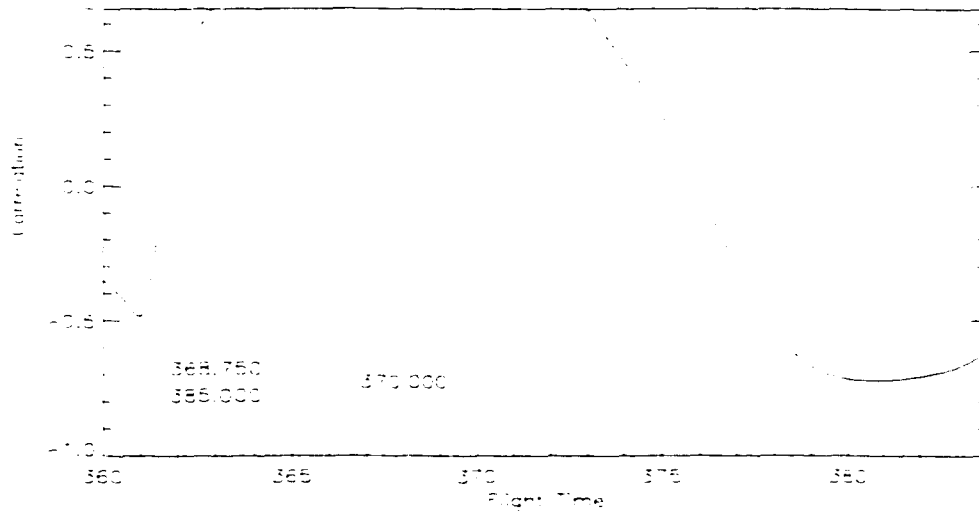


Figure 4-4: Correlation between the North and East Payload dc electric fields from T+368 to T+385 seconds.

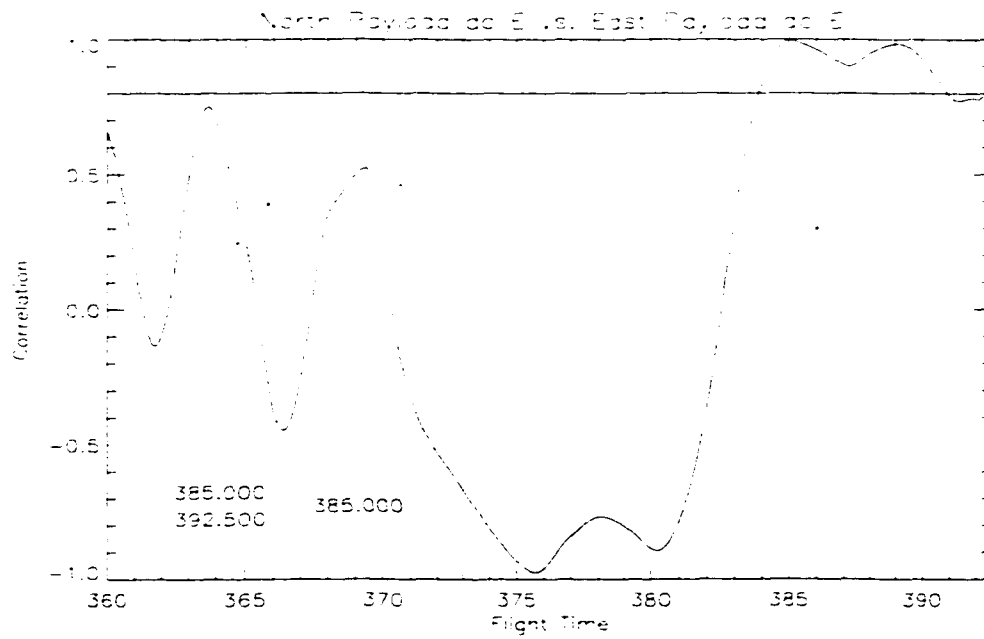


Figure 4-5: Correlation between the North and East Payload dc electric fields from T+385 to T+392 seconds.

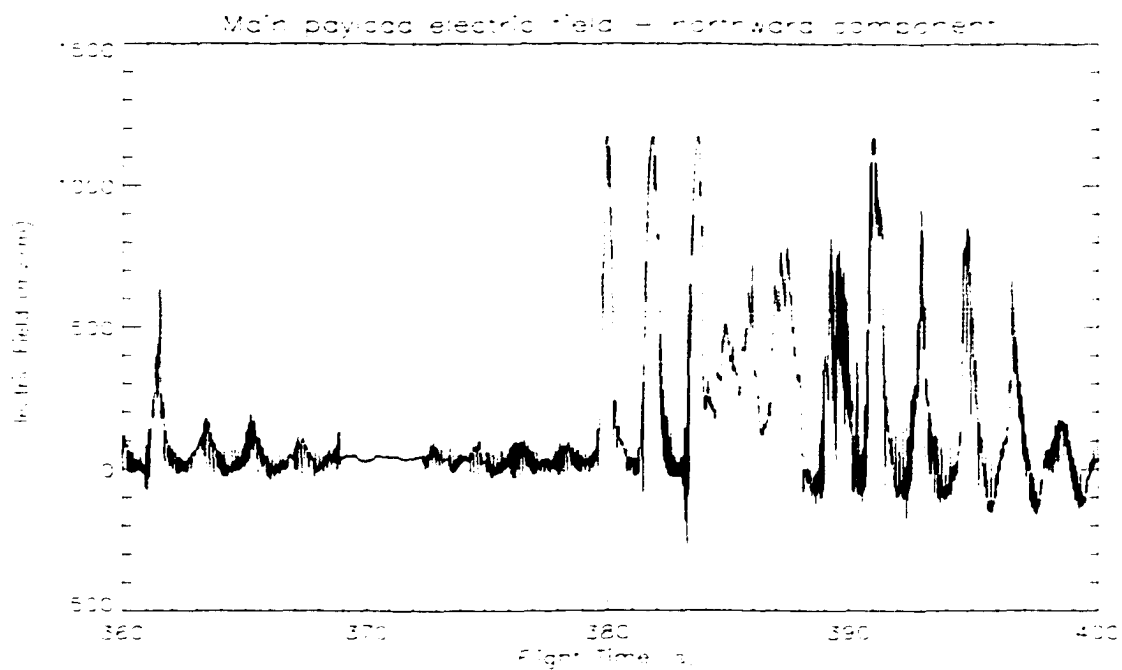


Figure 4-6: Northward electric field from the Main payload.

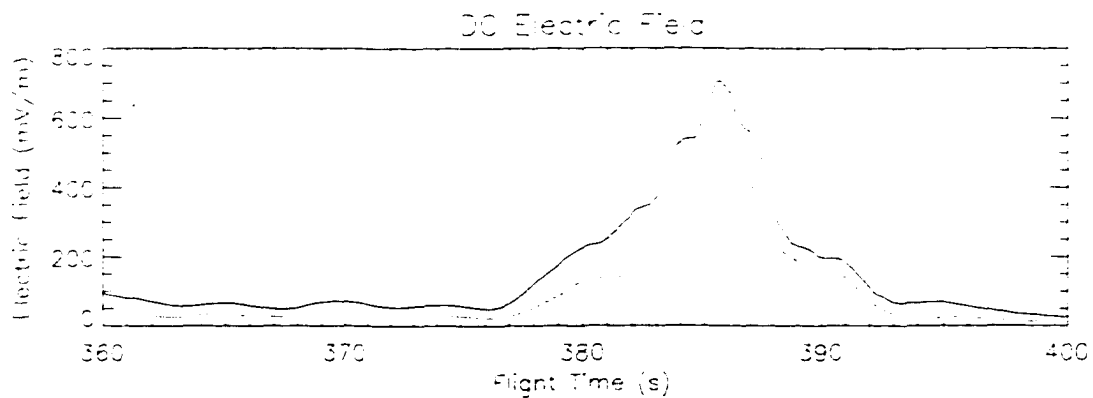


Figure 4-7: Arc aligned electric field components of the subpayloads (North - black, East - red).

shapes of the Main payload data. For example, the ACS is firing from roughly T+373 to T+384 seconds, as evidenced by the large noise signal. This is much different from the region just before T+373 seconds where the ACS is not firing, and the electric field measurement is not compromised. However, the ACS region has two distinct regions in the former time range. Large amplitude oscillations occur near T+380 seconds, rather than the smaller oscillations seen just prior. It is believed that this change in signal indicates a change in the background electric field. While this yields no information as to the magnitude of the increase, we assume that the time of this change can be used as a proxy for the time of the Main payload electric field increase. We can now include the onset times from the other payloads from Figure 4-7 to have three points from which we can determine the spatial and temporal aspects of the increase in field strength.

The data clearly show that the North payload observes the increase in electric field first, followed by the East and Main payloads. The time delay between the increases can be found by focusing on the region just near the onset. The rise in dc electric field on the East payload is 0.75 seconds after the onset of the North payload, somewhat smaller than the time obtained from the correlation analysis, but probably more accurate. Analysis of the Main payload data yields an onset time that lags the North payload by 1.75 seconds and the East payload by 1 second. We know the location of the payloads, the direction of travel, the payload speeds, and the speed of the payloads relative to the drifting arc. This information reveals that the payloads cannot be crossing through a static structure oriented parallel to the arc. The speeds of the payloads normal to the arc boundary, the time delays between the payloads, and the payload positions (see Figure 3-13) make the scenario of a static arc-aligned structure inconsistent with the data. Likewise, the delay

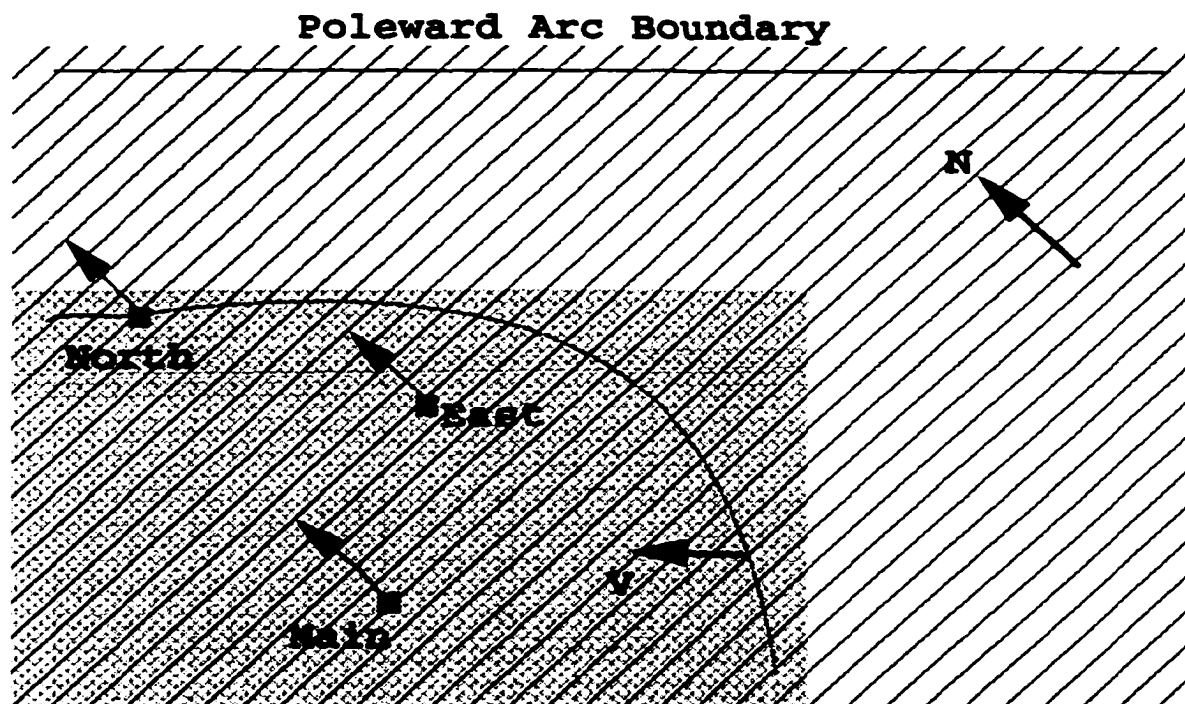


Figure 4-8: Possible scenario of a region of high electric field moving along the arc. The grey region represents a region of low electric field, the pink region is a region of fast plasma flow.

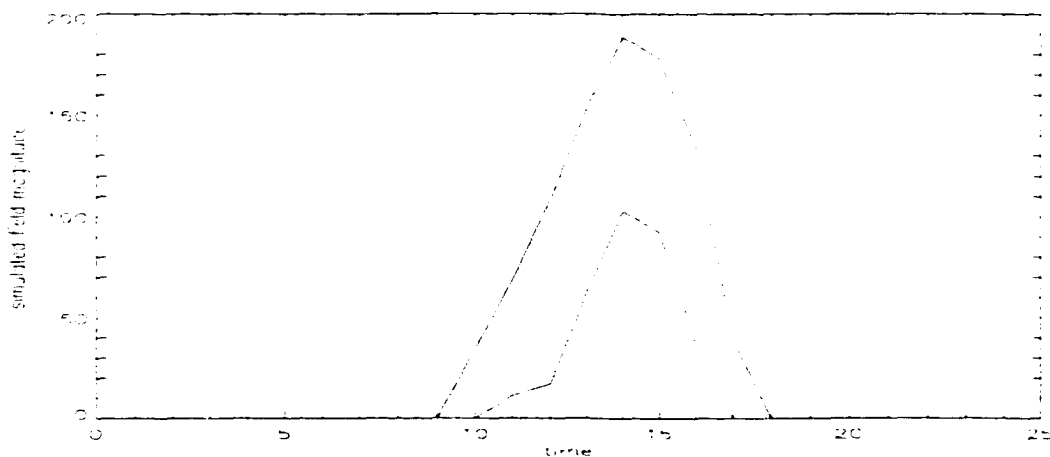


Figure 4-9: Modeled electric field measurement of three payloads moving northward as a region of fast moving plasma moves westward, followed by a temporal decrease in the plasma velocity. The North payload is in black, the East in red, and the Main in Blue, as in Figure 4-8.

time is not sufficient to support crossing some static region of enhanced field that is either oblique to the arc or arc-normal. The order in which the onsets occur rule out most other spatial forms.

Figure 4-8 represents a possible scenario that explains the electric field onsets at the various payloads. A boundary separates a region of no electric field (shown in grey) from a region of electric field with a magnitude of 63 mV/m. This field strength roughly represents the increase above two to three times the ambient electric field. The figure shows the three payloads inside the large arc, their velocity vectors (0.5 km/s northward with respect to the arc), and the poleward arc boundary. The difference in onset times between the North and East payloads is less than the time it would take to cross a structure that is arc-aligned. Only using the two subpayloads, we know that the structure must be oblique to the arc-aligned direction. The angle this structure makes with the poleward edge of the arc can have only one value for a spatially confined structure, based on the delay times observed. This alone, however, does not explain the rise in dc electric field magnitude. If the region of electric field structure was changing temporally in intensity, the second payload would not record a gradual change from ambient levels. Instead the second payload would have to have the same value in electric field magnitude as the first payload at the same time, which would appear as a discrete jump in the field magnitude. This is not observed, suggesting that the entire region is not changing in time before T+386 seconds.

The Main payload data show that a stationary spatial structure is inadequate to describe all of the observations. The onset of the Main payload is only 1 second after the onset of the East payload. The 1 km distance between these two payloads in the arc-normal direction is too large a distance for the Main payload to traverse in the time between delays, since the

relative motion of the payloads is only 0.5 km/s with respect to the arc. The region must have a strange shape, that the payloads happened to catch, or the region must be moving along the arc. Therefore, we suggest the scenario in Figure 4-8. The electric field values show that $\vec{E} \times \vec{B}$ motion of plasma would be mainly westward. Since the arc is aligned at an angle 45° to north, the flow would be primarily along the arc. The figure shows a line indicating a constant velocity contour. This line represents motion of plasma at one velocity, roughly 1.4 km/s, which the North payload encounters, the East 0.75 seconds later, and the Main 1 second after that. An increasing electric field then indicates an increase in the plasma flow. Increasing plasma flow would lead to a broadening of the curve of the next higher velocity contour between the East and Main payloads, to allow for the payloads to observe the same rise in electric field. This makes each subsequent line bulge out toward the middle, making a series of contours resembling an oval blob of plasma. The payloads then observe a blob moving past them, with ever increasing speed, ultimately reaching speeds of nearly 10 km/s. Then, at roughly T+385, a temporal effect takes over and diminishes the entire plasma speed uniformly over the entire spatial region.

Figure 4-9 shows a simulation of this scenario. A region of plasma with a shape similar to that in Figure 4-8 was given an initial westward velocity. The flow region had an increasing velocity as a function of eastward position in the region. Three observation points, simulating the payload positions, were then introduced into a region leading this westward flow and were allowed to move northward at 1 km/s. Each line trace represents the dc electric field that the payloads would measure as a function of time. The simulation was created to test the spatial and temporal signatures of the plasma blob, so the magnitudes shown were not meant to simulate exactly the measured magnitudes. The color of each

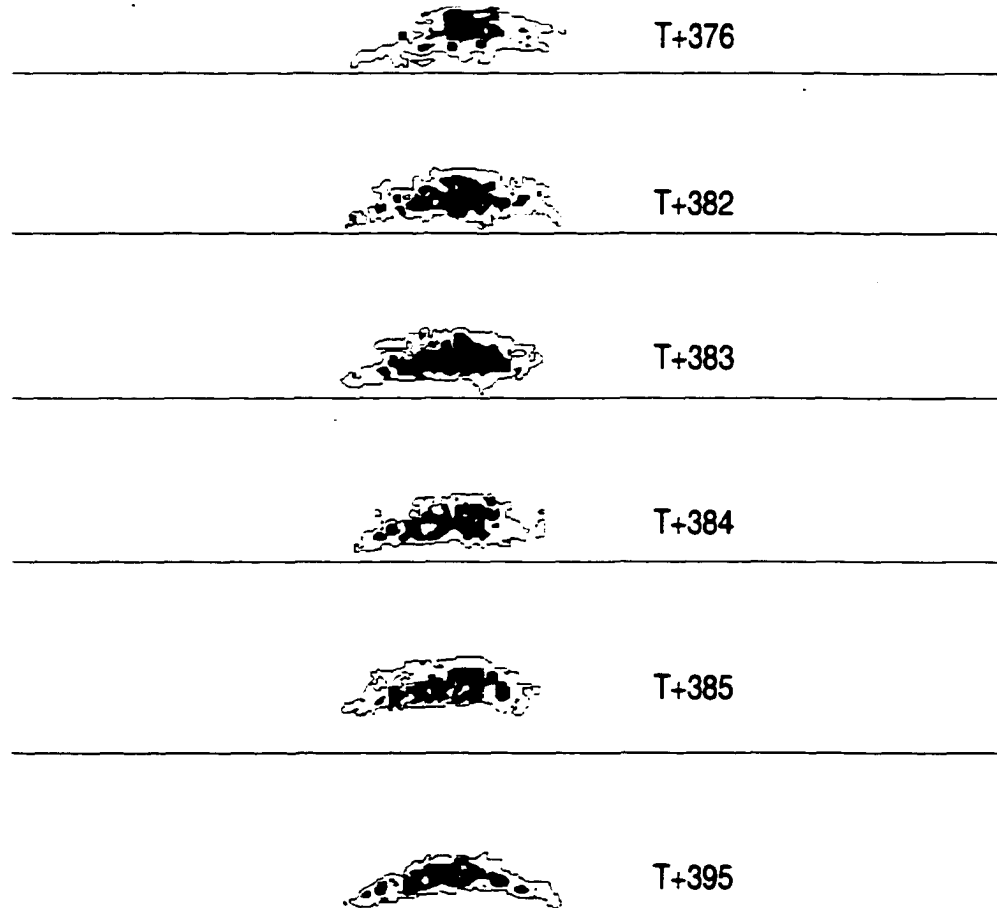


Figure 4-10: Digitized all-sky images for successive flight times during the main arc fly-through.

trace matches the payload colors given in Figure 4-8. The payload entries into this fast flow region are obvious in Figure 4-9, and although the spatial resolution of the figure is low, the North payload does observe the rise in electric field magnitude first. The East payload is the next to see this rise, followed by the Main payload. The modeled temporal decrease is also evident in all three traces. The three payload simulation data match very well with the actual measured changes in dc electric field. We do not wish to compare the magnitudes simulated at each payload location, but the important features that were reproduced were the delay in rise times and temporal decrease of the dc electric field due to a spatially confined region of fast plasma flow that moved westward across the payload trajectory.

These types of fast motions in aurora are certainly not uncommon. Sporadic plasma flows have been shown to reach tens of km/s in auroral arc forms [*Hallinan*, 1981]. The observations of these flows are traditionally performed using all-sky imagers. We can use the all-sky images from the AT II flight to verify this westward-moving blob scenario. Figure 4-10 shows the results of this analysis. Still images from the video of the all-sky camera from the night of the launch were digitally captured. Every fifth video frame capture was then analyzed by graphically tracing regions of the same intensity level. In Figure 4-10, the brightest region is filled in green, and the payload location is shown in red. The blue trace in each panel is an outline of the next brightest region of the arc. After the tracing was completed, the background all-sky capture was removed from the picture, leaving only the tracings. The brightness traces can be compared to Figure 3-1, which is one of the frames used in this process. The flight time for each panel is given to the right of each tracing.

The digitized frames of the all-sky images do not substantiate conclusively motion of

the plasma in any one direction. It is impossible to verify whether perceived motions are actually motions of plasma or temporal changes in a source region for precipitating electrons. However, visually a gradual motion of the bright green blob appears to drift toward the payloads from T+383 to T+386 seconds, which would be a mostly westward motion. The images indicate a 2.9 km/s westward motion along the arc. This value falls well within the range of 1-10 km/s as obtained from the electric field data. Therefore, the all-sky images do support the proposed scenario, even though visually interpreting the motions can be somewhat subjective.

We therefore turn to the particle data, which may be more useful since there are multiple independent measurements. *Lynch, et al., [1999]* have shown that dispersed electron events near this time indicate a westward motion of the field aligned electrons at speeds between 2 and 5 km/s. This speed is also in the correct velocity range in order to be in agreement with the dc electric field observations. The times of the bursts do not exactly coincide with the time of the electric field increase, but the motion again supports the moving blob scenario.

When comparing the precipitating electron data with the dc electric field data, there is a noted dissimilarity. The particle data indicate a reversal in motion after T+390 seconds. This reversal is not seen in the electric field data. This counterstreaming in auroral arcs is rather common in both visible and black aurora [*Trondsen and Cogger, 1997*], and the inferred 1 km/s eastward motion of the electron bursts would again mean the presence of a rather large dc electric field [*Hallinan and Davis, 1970*], directed mostly southward. However, it was conjectured in *Lynch, et al., [1999]* that the source of the precipitating electrons could be moving eastward during this entire time from T+380 to T+400 seconds.

However, the large electric field dominates the plasma motion before T+390 seconds and thus the plasma drifts westward when the field is present. When the field is reduced, the source motion then dominates. As indicated in the previous section, the decrease in electric field may indicate the upward movement of the the acceleration region and the S shaped potential structure. The payloads could then be in a region where the observed electric fields are disconnected from the fields in the acceleration region above, which would also explain the dissimilarity.

There is another type of dissimilarity, but not between the particle data and electric field measurements. There is a noted dissimilarity in the two electric field measurements by the subpayloads, as evidenced in Figure 4-7. Although both payloads see, in general, an increasing electric field, there are marked differences in the slopes of the increases. Thus, even if the magnitudes are not certain due to the shadowing, there are still differences in how the dc field changes, which is indicative of a dc electric field shear between the two subpayloads.

4.3 Electric Field Shear and Waves

This region of large electric field, fast plasma motion, and dc electric field shear is also remarkable for the existence of electrostatic wave power. We now explore the relation between these characteristics and why the shear may be necessary to explain the wave observations.

4.3.1 Brief Description of the IEDD mechanism

The inhomogeneous energy density driven mechanism has been developed and explained by *Ganguli, et al., [1985]* and *Gavrishchaka, et al., [1996]*, and we briefly summarize their findings to provide the context we need for interpreting the observed electrostatic waves.

The dispersion relation for ion-cyclotron modes (D_{IC}) is given by

$$D_{IC}(\omega, k) = 1 + \tau - \Gamma_0 - \sum_{n>0} \frac{2\omega^2 \Gamma_n}{\omega^2 - n^2 \Omega^2} = 0. \quad (4.3.1)$$

where

$$\tau = T_i/T_e \quad (4.3.2)$$

$$\Omega = eB_0/m_i c \quad (4.3.3)$$

$$\Gamma_n(b_1) = I_n(b_1) e^{-b_1} \quad (4.3.4)$$

$$b_1 = k_{\perp}^2 \rho_i^2 / 2 \quad (4.3.5)$$

$$\rho_i = v_i / \Omega_i \quad (4.3.6)$$

k_{\perp} is the perpendicular component of the wave vector, I_n are the modified Bessel functions, and $(k \lambda_i)^2 \ll 1$ and $(\omega/v_e) \ll k_{\parallel} \ll (\omega - n\Omega_i)/v_i$ has been assumed, where λ_i is the Debye length.

The energy density for these modes is then given by

$$U \propto \omega \left(\frac{\partial D}{\partial \omega} \right) = \omega \left(\sum_{n>0} \omega \frac{4\Gamma_n n^2 \Omega^2}{(\omega^2 - n^2 \Omega^2)^2} \right) = \omega^2 \sigma(\omega), \quad \sigma > 0. \quad (4.3.7)$$

Since this energy is always positive, let us introduce a spatially confined, transverse electric field, E_0 , and call the region where the field exists Area 1. The introduction of an electric field creates a velocity drift that Doppler shifts the mode frequency in the lab frame. Thus, the new energy density can be given as

$$U' = \omega \omega_1 \sigma(\omega_1) \quad (4.3.8)$$

where

$$\omega_1 = \omega - k_y V_E \quad (4.3.9)$$

is the Doppler shifted frequency in the region of electric field, k_y is the y component of the wave number, and V_E is the resulting drift from the electric field. From Equation 4.3.8, it is easily seen that for sufficiently large $k_y V_E$, the energy density will be negative. The inhomogeneity in the electric field, due to its spatial limitation, prohibits the waves from transforming to another frame in which they can have a positive energy density. Nonlocal wave packets can couple fluctuations in the different regions such that an instability is fueled by the transfer of energy across the shear layer. This is the origin of the inhomogeneous energy density driven instability.

The IEDD mechanism has both a reactive and dissipative response. The dissipative response is a non-reversible process by which the wave gains energy from the plasma through inverse Landau damping. The reactive response is a reversible, non-local energy transfer between waves in Area 1 and the area without electric field, where the medium and waves do not exchange energy. For large scale sizes of the shear, the dissipative response dominates and this has several implications for waves generated by the instability. The inhomogeneity in the electric field not only causes a dependence of ω_1 upon V_E as seen in Equation 4.3.9,

but the growth rate, γ also develops a dependence upon V_E . The effects on the growth rate can be much more severe than on the Doppler shifted frequency, seriously affecting mode growth. In fact, the threshold currents required for generation of ion-acoustic and drift mode waves are raised with the inhomogeneous electric field, while the current required for the ion-cyclotron waves is diminished. The lowering of the threshold current is a direct result of the inhomogeneity creating multiple roots of the dispersion relation and affecting the phase velocity of each mode that can be excited. This allows resonance conditions to be met over a wider range of parameters, such that the net effect is the lowering of currents required for the onset of wave activity. The strength of the inhomogeneity also lowers the mode frequencies, which leads to a broadening and spiking of the observed wave spectrum [Amatucci, *et al.*, 1994]. We now apply this information to the AT II data set.

4.3.2 AT II Electrostatic Wave Observations and Discussion

The waves observed in the subpayload data are shown in Figures 3-29 through 3-32. The observations to note are that the broadband waves cover frequencies from dc to roughly 100 Hz (the oxygen cyclotron frequency is 42.8 Hz), the waves have distinct regions of enhancement, and the waves are electrostatic. This last property is not seen in the electric field data alone - the magnetometer data is needed to verify this assertion. Fourier transforms of the magnetometer data reveal no wave signatures or power throughout the entire region of interest. If there were wave signals in the magnetic data, they would be below the resolution of the magnetometers. The bit errors in the magnetometers would cause oscillations below 0.2 nT to be unobservable. With the oscillations in the electric field at approximately 2.0 V/m, the ratio $\frac{\delta E}{\delta B}$ is on the order of 10^{10} m/s. This is well above the

local Alfvén speed of 7.4×10^6 m/s, and we can therefore make the claim that the observed waves are indeed electrostatic [Wahlund, et al., 1998]. The cutoff near 100 Hz can be used to determine the perpendicular wave number of the ion-cyclotron waves through

$$\omega_{ic} = \omega_{gi} \left(1 + \frac{1}{2} k_{\perp}^2 r_{gi}^2 \right). \quad (4.3.10)$$

If we input the measured plasma parameters into the above equation, we can determine a minimum perpendicular wave number of 111 km^{-1} . The calculation of $\frac{\partial \omega}{\partial k}$ then yields a group velocity approximately 1.2 km/s.

Based on the altitudes that the AT II payloads reached, we can estimate the concentrations of oxygen and hydrogen from Figure 1.2 in Kelley [1989]. Between T+380 and T+390 seconds, the payloads were at an altitude of roughly 540 km, which corresponds to a plasma that is approximately 90 percent oxygen ions and 10 percent hydrogen ions. In a pure oxygen plasma, at 500 km altitude, an ambient density of $10^4/\text{cc}$, $T_e/T_i \approx 1$, and $T_e = 2600^\circ$, a field aligned current of nearly $10 \mu\text{A}/\text{m}^2$ is needed to drive the ionosphere unstable to ion cyclotron waves [Kindel and Kennel, 1971]. If the plasma has a hydrogen component, the critical current threshold is increased, while if the density decreases, the critical current likewise decreases. Ion acoustic waves cannot be excited at these low altitudes unless the current reaches over $1000 \mu\text{A}/\text{m}^2$, and a decrease in the ratio of T_e/T_i increases the value of the critical drift for all wave modes.

Given the framework of Kindel and Kennel, [1971] and the observed wave characteristics, we can interpret the AT II results. Our observations are in a 10 percent hydrogen plasma with an ambient density of $1100/\text{cc}$. Assuming $T_e/T_i \approx 1$ and $T_e = 1160^\circ$, we have nearly the same conditions as noted in Kindel and Kennel, [1971]. As mentioned in the previous

section, onboard magnetometers only measure a field aligned current of, at most, $4\mu\text{A}/\text{m}^2$. This is a factor of more than two below the needed current to be conducive for ion cyclotron wave growth, and orders of magnitude too small for ion acoustic waves.

Rather than comparing rough numbers to the figures in *Kindel and Kennel, [1971]*, we can put the known plasma parameters into the Waves in Homogeneous, Anisotropic, Multicomponent Plasmas, or WHAMP [*Rönmark, 1983*] computer program. The WHAMP code solves the dispersion relation of waves in a magnetized plasma, given the inputs of the local electron cyclotron frequency, and information about the composition, density, temperature, anisotropy, velocity drift, and loss cone features of the ambient plasma species and precipitating particles. The code returns the frequencies of waves able to be supported by the input parameters. We have used the WHAMP code with the AT II data set inputs to determine the waves that can exist in our plasma environment.

Figure 4-11 shows dispersion surfaces for the input parameters from the AT II data set. The left two figures show the dispersion surfaces for the plasma parameters that the AT II payloads directly measured. The axes of the plots are normalized to the hydrogen cyclotron frequency, and the surfaces represent the wave frequency (f / Ω_H), on the vertical axis, as a function of wave number ($\log(k_{\parallel}/\rho_H)$ and $\log(k_{\perp}/\rho_H)$), horizontally. Some values of the normalized frequency have been superimposed on the plot for identification purposes, since the vertical scaling is different for each panel. The WHAMP code solves the dispersion relation in an iterative process, varying either the perpendicular wave number or the parallel wave number first. The top plots in Figure 4-11 represent cycling through the perpendicular wave number first, while the bottom plots indicate the code iterating through the parallel wave number first. The resulting profiles are very similar, although some features become

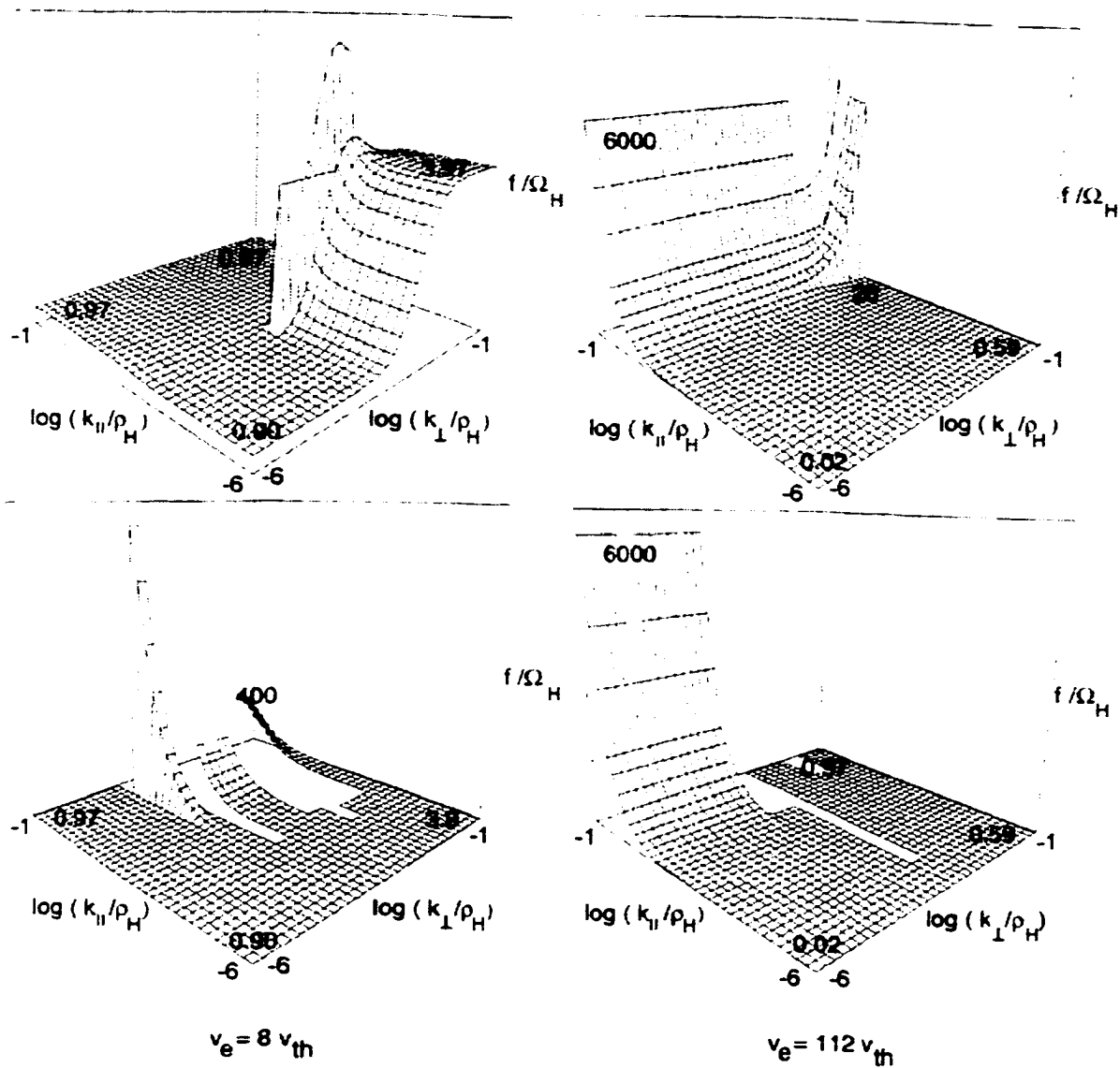


Figure 4-11: Dispersion surfaces from the WHAMP code. Note that each panel has a different vertical scale. Some frequency values have been superimposed on each plot for identification.

more evident when one approach is used vs. the other. This tends to change the vertical scaling which accentuates small differences. For example, the top left panel clearly shows the wave frequency increasing from near the hydrogen cyclotron frequency to four times Ω_H as a function of k_{\perp} . The bottom left panel also shows this feature, although the large increase seen in the k_{\parallel} direction changes the scale such that the rise in the k_{\perp} direction is not noticeable.

Let us now investigate the particulars of Figure 4-11, and then explain the meaning of the right two panels of the figure. The left panels clearly show that using the measured plasma parameters from the payloads, including the precipitating electron beam, the lowest frequencies that can be attained are near the local hydrogen cyclotron frequency, or approximately 685 Hz. Referring back to Figures 3-29 through 3-32, there is no wave power over 400 Hz, and the only significant wave power is found well below 200 Hz. Using the measured plasma conditions, the observed waves could not be created in a homogeneous, isotropic plasma.

This fact leads us to consider the right panels in Figure 4-11. These two panels show dispersion surfaces using the same plasma conditions as the left panels except for the speed of the precipitating electron beam. This modified electron beam has a velocity 56 times greater than the measured beam taken from the particle data on the subpayloads. The value of this artificial increase represents the lowest velocity that would allow the plasma to sustain wave growth below 600 Hz. Therefore, ion cyclotron waves would be excitable in the plasma that the payloads flew through, if currents provided in the region of precipitation were sufficient to drive the region unstable to these waves. Something would need to decrease the threshold currents needed for onset of the ion cyclotron instability. As we have mentioned in the

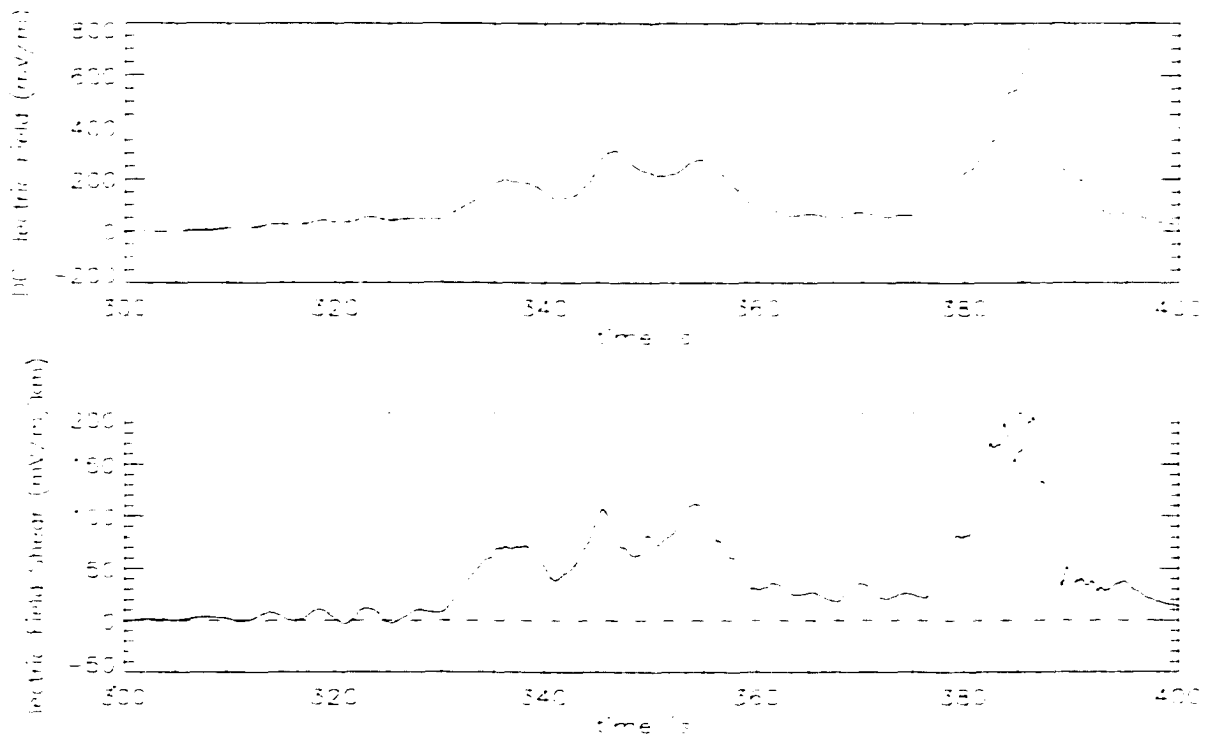


Figure 4-12: Dc electric arc-normal fields (top panel) from the North (blue) and East (red) payloads and the dc shear (bottom panel) calculated from the top panel.

previous section, if there was a region of electric field shear, which could also be thought of as a region of velocity shear, the threshold current levels needed for wave growth would be dramatically reduced [Ganguli, *et al.*, 1985, Gavrishchaka, *et al.*, 1997].

Figure 4-12 shows the dc electric field perpendicular to the arc normal from the North (blue) and East (red) payloads in the top panel, and the bottom panels shows the shear between the payloads in the arc normal electric field. The shear is calculated by subtracting the dc electric field values of the two payloads and dividing by the distance between them, yielding a shear with units of mV/m/km. From the bottom panel, it is seen that the shear between the payloads reaches a maximum magnitude of nearly 200 mV/m/km near the

same region where the dc field from both payloads records maxima. This numeric value for the shear may be in question, due to the shadowing effect explained in Appendix A. Therefore, we re-calculate the shear, assuming the East payload is the more correct. We then normalize the North payload electric field data to the East payload data. This analysis is shown in Figure 4-13.

The top panel shows the dc electric field of the East payload in red and the normalized North payload data in black. It is clearly evident that there are still significant differences between the payloads. This difference is shown in the second panel, where the shear between the payloads has been recalculated using the new normalized North payload data. The is now smaller in overall magnitude, but still reaches a peak value of almost 100 mV/m/km. Although the absolute magnitude of the shear between payloads may be in question, the existence of it is not.

Before we move on to comparisons between the shear and the electrostatic waves, we note the following aspect of the shear measurement. The final panel in Figure 4-13 shows the arc-normal spatial derivative of the East dc electric field data. This derivative is what is usually used to infer a shear from a single payload measurement, with the assumption that there are no temporal variations. We have already shown that the region after T+386 seconds is a purely temporal change, but this would not be evident from a single payload observation. The inferred shear reaches a magnitude of over 200 mV/m/km when we know the changes are temporal. The multiple payload shear in the panel above does observe a shear, but the magnitude is more than four times lower than the inferred shear. The shear estimate for the single payload is only along the direction of the payload trajectory. The multipayload shear calculation can measure shear both across and along the arc. Since many auroral arc

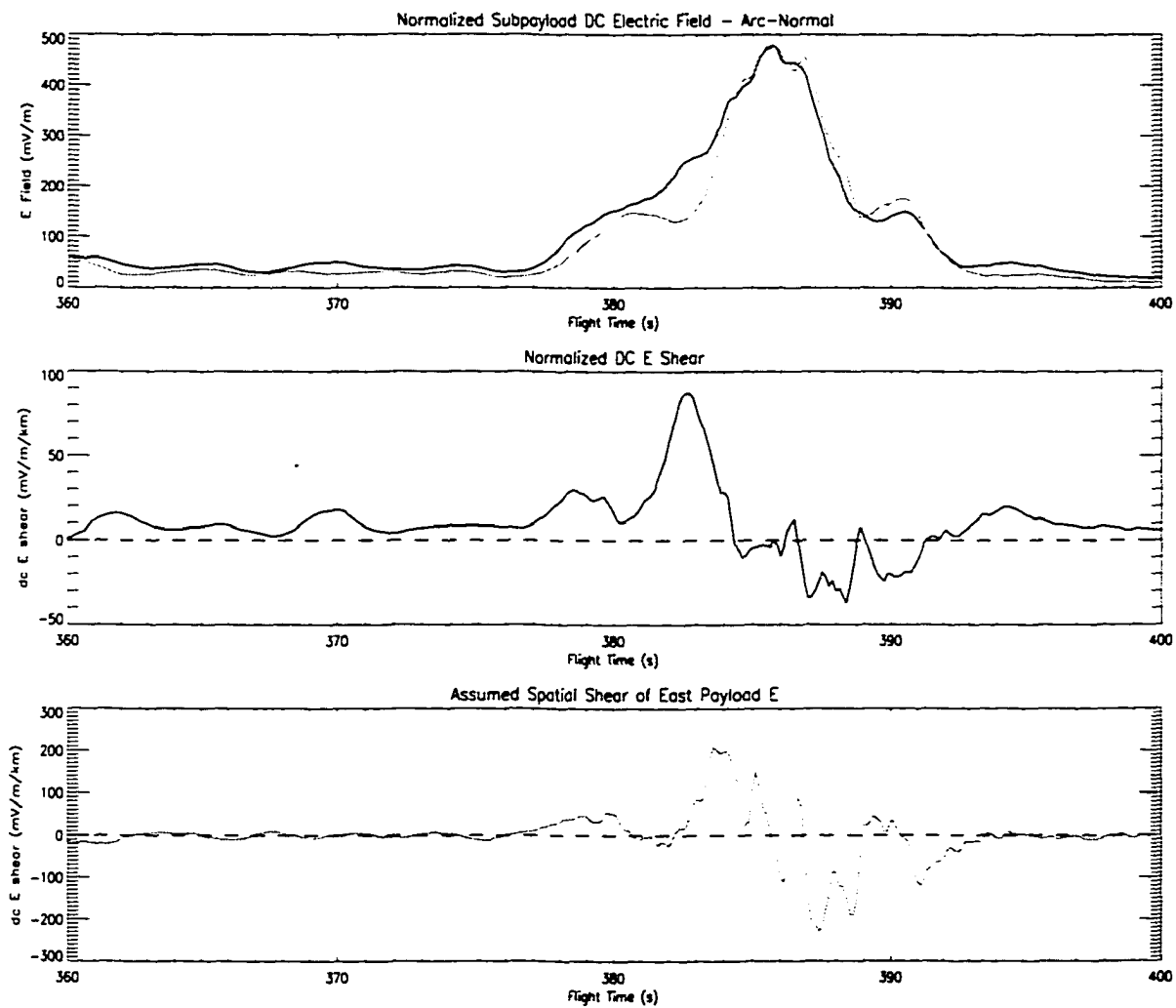


Figure 4-13: Top panel: dc electric arc-normal fields from the North (black) and East (red) payloads. The North panel has been normalized to the East payload. Middle panel: recalculated shear using the normalized data set. Bottom panel: dc shear calculated from the arc-normal spatial derivative of the East payload.

models assume no significant variations along an arc, this can determine the validity of that assumption.

We now refer back to Figures 3-29 through 3-32 to look at the electrostatic wave activity over this same region. The regions of increased dc electric field fall in the same area as the regions of electric field shear and the regions of increased wave activity. We must therefore attempt to determine the correlations between these three measurements to understand the root cause of the wave production. Determining numerical correlation values between the different measurements is not straightforward, and the results are not always obvious, and we now present a variety of correlative studies to better understand the limitations of using this type of analysis.

Figure 4-14 shows the correlation between the dc electric field measurements of the two subpayloads. The figure has the same labeling as Figures 4-4 and 4-5. Figure 4-14 covers a much broader time range than Figures 4-4 and 4-5, so it includes both the increase in electric field and the temporal decrease. Although we now lose the information about the different regions, we gain information about the region in a general sense. The similar increases and decreases in slopes are indicated through a high correlation number of nearly one. The offset time here can only be interpreted as noting the marked similarity between the measurements, and cannot be used to determine spatial/temporal properties. Thus, we can use a large time span to indicate general trends and verify that the payloads were measuring the same basic phenomenon.

Figures 4-15 and 4-16 show the correlations of wave power between two different frequencies in the dc electric field data. Each compares the wave power at the oxygen and hydrogen cyclotron frequencies for the North (Figure 4-15) and East (Figure 4-16) pay-

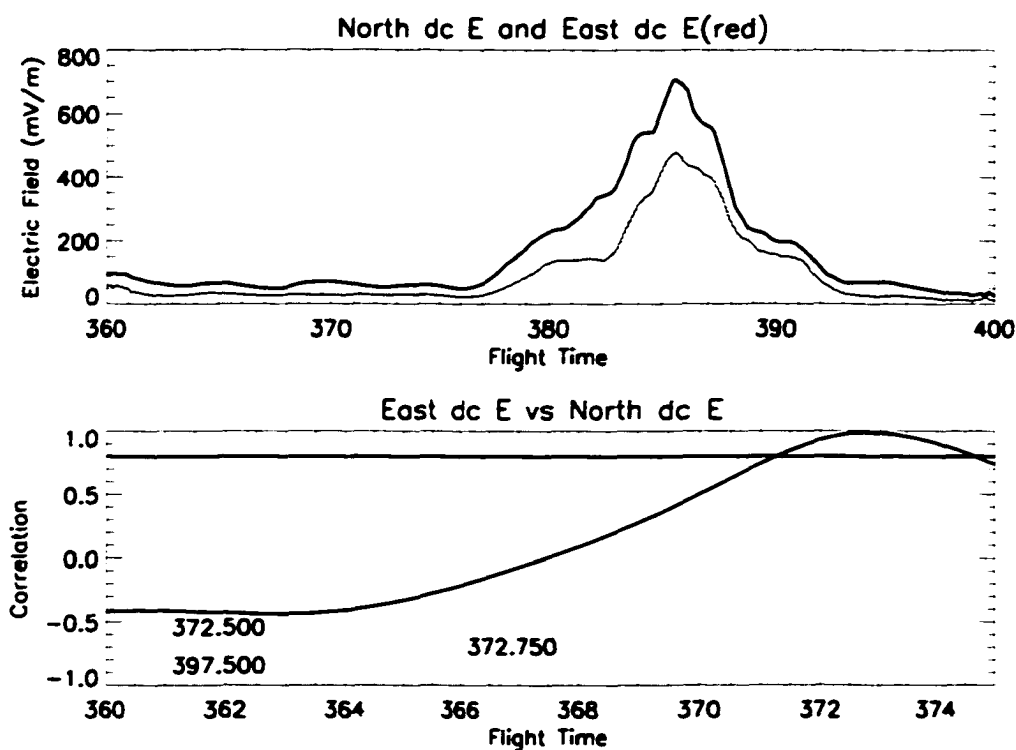


Figure 4-14: Top panel: North and East dc electric fields. Bottom panel: Correlation between East payload dc electric field and the North payload electric field from T+372 to T+397 seconds.

loads. We can see that there is no correlation between the strong signal seen at the oxygen cyclotron frequency and the weak signal seen at higher frequencies. This likely indicates the signal at frequencies larger than 200 Hz is mostly random noise. This verifies that the wave power is generally concentrated around the oxygen cyclotron frequency, which is the dominant species in this region of interest.

Since the majority of the wave power is concentrated near the oxygen cyclotron frequency, we will use the power at that frequency as a basis of comparison for the other measurements. First, we return to the idea of regarding general trends in the data by correlating the wave power at 42 Hz on both payloads, which is shown in Figure 4-17.

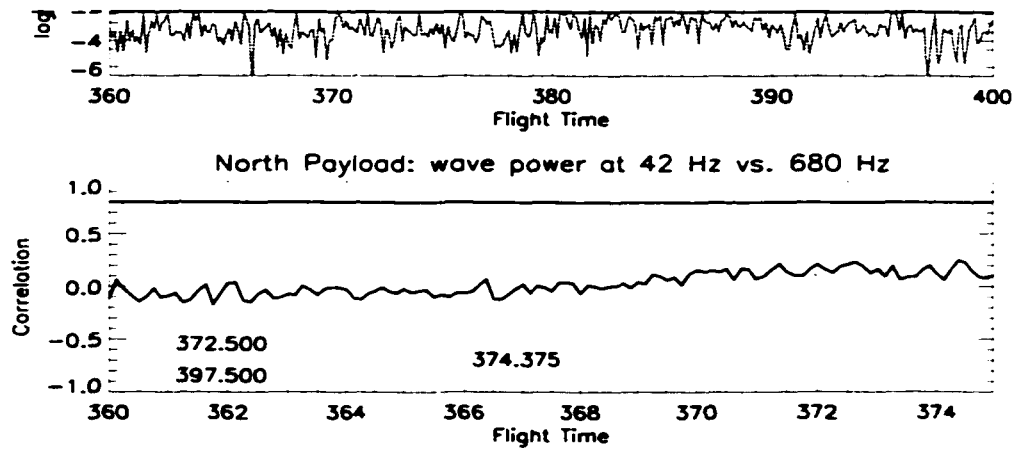


Figure 4-15: Top panel: North payload wave power at 42 Hz and 680 Hz. Bottom panel: Correlation between wave power at 42 Hz and at 680 Hz on the North payload from T+372 to T+397 seconds.

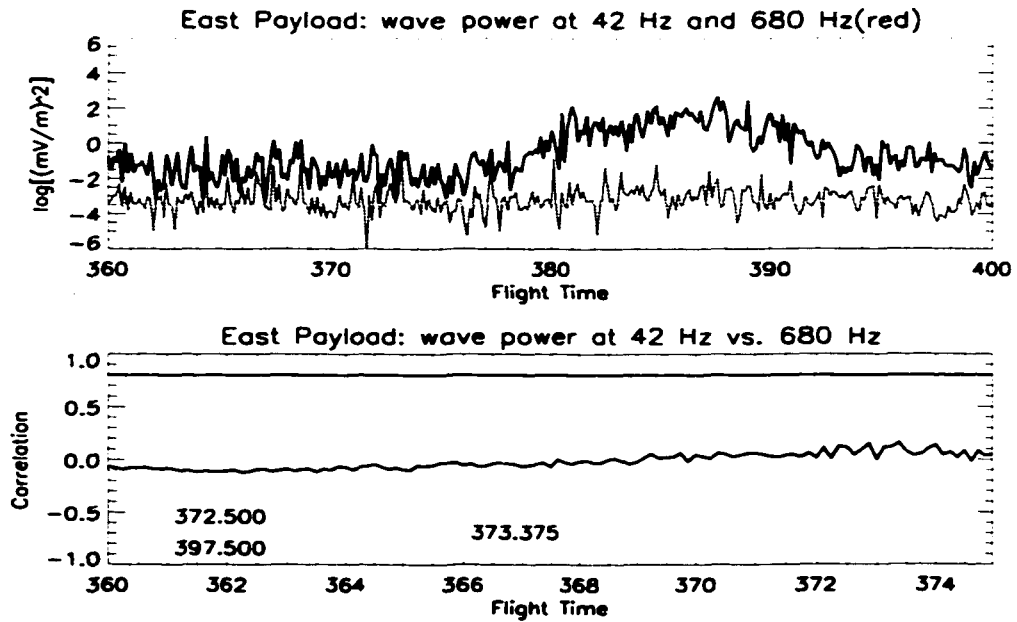


Figure 4-16: Top panel: East payload wave power at 42 Hz and 680 Hz. Bottom panel: Correlation between wave power at 42 Hz and at 680 Hz on the East payload from T+372 to T+397 seconds.

The highest value of correlation is well below the confidence value of 0.8, so we cannot claim that the wave power between the two payloads is exactly correlated. This is a direct contrast to Figure 4-14, where the two payloads measure nearly the same global increase and decrease in dc electric field. The wave measurements appear very different, indicating a spatial/temporal variation between the payloads. This suggests that the dc field alone, which both payloads measure similarly, may not be responsible for the observed electrostatic waves.

If the localized, transverse dc electric field alone is not wholly responsible for the wave generation, it is possible that the cross-payload shear is a contributor. Figure 4-18 shows the correlation between the shear in the dc electric field and the wave power at 42 Hz from the East payload. The maximum value of the correlation of 0.7 is not quite high enough to establish firmly a correlation between the two measurements. For argument's sake, Figures 4-19 and 4-20 are also presented, showing the correlations between the North and East payload dc electric fields and the East wave power at 42 Hz, respectively. The maximum values for all three correlations are near 0.7, which is not surprising, since the shear calculation is based on the two dc electric field measurements to which it is being compared. The general rise and fall in wave power is picked up in the correlation computation, but no significant conclusions can be made concerning the source of the waves from these three figures. Comparing individual peaks in the wave power data to fluctuations in the dc electric fields and shear are inconclusive when trying to determine correlations at smaller time scales. Some peaks in the wave power match peaks in the shear, while others match with the electric field data from each payload, making it difficult to ascribe the wave production to the shear.

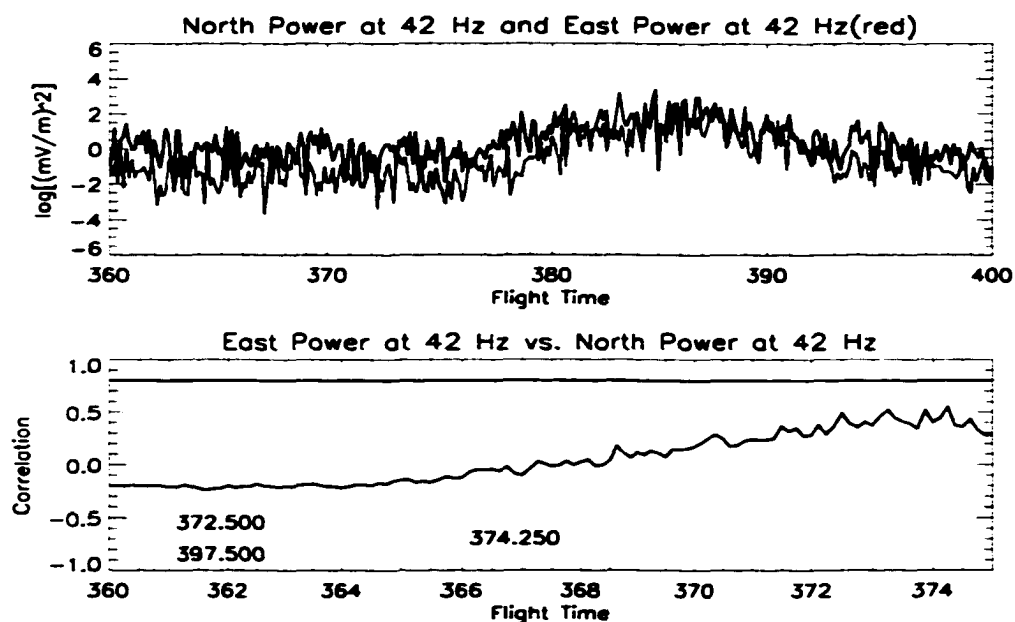


Figure 4-17: Top panel: North and East payload electric field wave power at 42 Hz. Bottom panel: Correlation between wave power at 42 Hz on the East payload and wave power at 42 Hz on the North payload from T+372 to T+397 seconds.

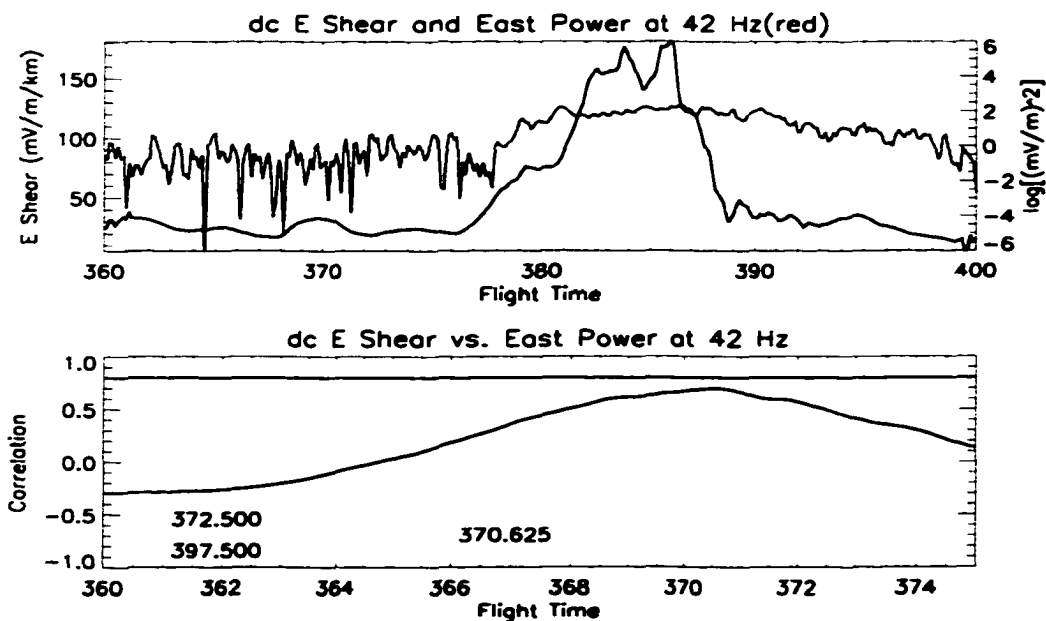


Figure 4-18: Top panel: dc electric field shear and East payload electric field wave power at 42 Hz. Bottom panel: Correlation between dc shear and the East payload wave power at 42 Hz from T+372 to T+397 seconds.

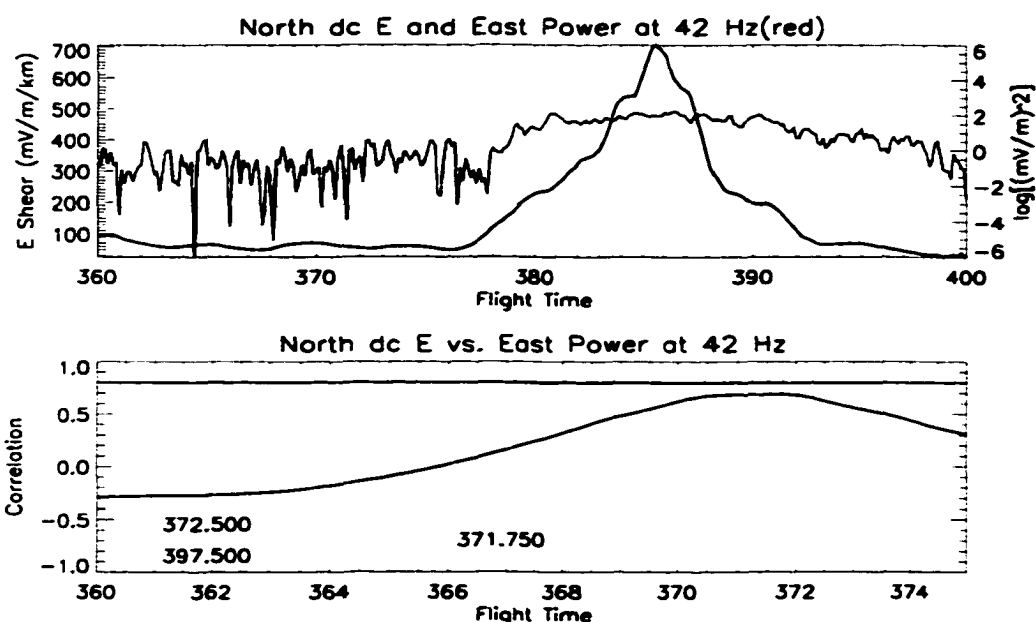


Figure 4-19: Top panel: North payload dc electric field and East payload electric field wave power at 42 Hz. Bottom panel: Correlation between the North dc electric field and the East wave power at 42 Hz from T+372 to T+397 seconds.

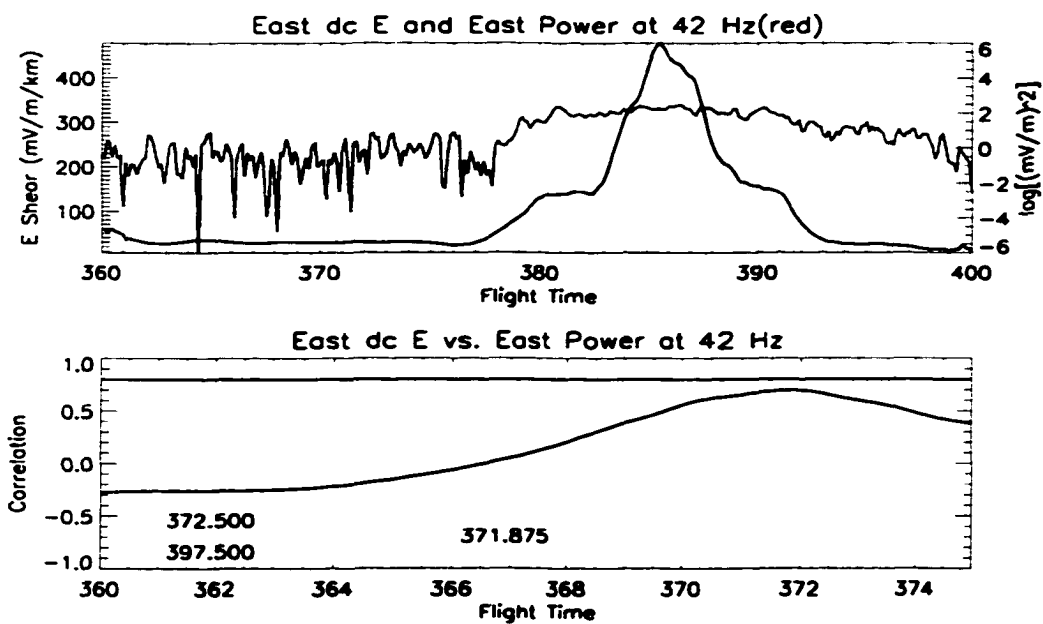


Figure 4-20: Top panel: East payload dc electric field and East payload electric field wave power at 42 Hz. Bottom panel: Correlation between the East dc electric field and the East wave power at 42 Hz from T+372 to T+397 seconds.

We have shown in the previous section that the decrease in electric field magnitude after T+385 seconds is temporal, while the increase in field before that time is most likely a region of spatially limited plasma moving past the payloads. The wave power, seen best in Figures 3-31 and 3-32, does not show any significant change between the regions T+379 - T+385 seconds, the more spatial regime, and T+385 - T+392 seconds, the temporal regime. The shear between the payloads, like the wave power, spans both of these ranges, and the decrease in shear beginning just after T+386 seconds appears to match well with the change in slope of the wave power from positive to negative. If we also consider the time that the dc field is increased, both subpayloads show an enhancement above ambient levels for 17 seconds. Meanwhile; the shear between the payloads shows enhancement for 15 seconds, and the wave power for both payloads also shows enhancement for 15 seconds. This may be evidence that the shear between the payloads is more responsible for the observed waves than the localized dc field itself.

Although the exact magnitudes of the shear may be less than the calculated values, we can use the values of shear from Figure 4-12 to determine an upper bound as to the shear frequency, ω_s , which is given by Equation 1.1.7. From the figure, we can determine the shear frequency simply through

$$\omega_s = \frac{dV}{dx} = \frac{1}{B} \frac{dE}{dx} \quad (4.3.11)$$

where B is the magnetic field strength, and dE/dx is the shear as given by the bottom panel in Figure 4-12. The calculated value for ω_s is then 4.4 s^{-1} , or $0.1 \Omega_{O+}$. If we instead use the normalized shear values from Figure 4-13, we obtain a value for ω_s of 2.2 s^{-1} . We now can compare the characteristics of the shear and the observed electrostatic waves in a

quantifiable manner.

We can systematically eliminate many shear-driven instabilities from our list of causes of the wave growth observed. The cross-payload shear observed is perpendicular to the magnetic field, so that eliminates several field aligned possibilities, including the D'Angelo and streaming instabilities [Ganguli, *et al.*, 1994]. The electron ion hybrid (EIH) instability requires shear frequencies that are greater than the lower hybrid frequency, and for the plasma environment of the AT II measurements, that value is approximately 1.7 kHz, thus eliminating EIH from the list. The current driven electrostatic ion cyclotron (CDEIC) instability is not likely for several reasons. As already mentioned, the threshold currents needed for destabilization are higher than the $4\mu\text{A}/\text{m}^2$ observed in the region. Also, the CDEIC instability produces waves that are in a single, small frequency range very close to the cyclotron frequency. The limited resolution of the electric field frequency spectrum shows that the observed wave frequencies are not only broadband, but do not have any one single preferred frequency.

Recent studies have also investigated the role of Alfvén waves in ionospheric heating [Kagan, *et al.*, 1996]. Near this time, there is an Alfvénic wave measured on the subpayloads. It may be possible that the electrostatic waves are a result of the interaction between the Alfvén wave event and the ionosphere. However, the electron detectors are unable to measure heating of the core populations as measurements below 10 eV were unattainable due to the range of the high voltage supplies. Also, the electron heating discussed in Kagan, *et al.*, [1996] is proportional to the inverse square of the density. There are no observable changes in the density when the payloads measure the broadband waves.

Through process of elimination, we come to the inhomogeneous energy density driven

(IEDD) instability. This instability, as previously mentioned, requires the existence of a localized dc electric field, perpendicular to the magnetic field, which creates a region of velocity shear. The existence of the localized dc field may be able to lower the current requirements, but we observe an additional shear between two payloads that seems to be responsible for wave growth. The localized region of shear can be characterized by a shear frequency, which must be at or below the ion cyclotron frequency. In our instance, a value of one tenth the oxygen cyclotron frequency is not too low a shear frequency and would be able to destabilize the plasma [Amatucci, 1999]. The IEDD instability generates waves near the ion cyclotron frequency, but the waves are not produced at one main frequency, as are CDEIC waves, but are rather broadband and spiky in nature. Our observed waves show no preference for any one particular frequency, and range in frequency around Ω_{O^+} . It is therefore very likely that the IEDD instability mechanism is driving the plasma unstable, and in so doing allowing the current requirements for wave growth to be reduced to below their usual levels and allow for the generation of the broadband, spiky waves near the oxygen cyclotron frequency that are observed on multiple payloads.

Chapter 5

Conclusions

The AT II sounding rocket mission has provided, for the first time, three points of measurement in an auroral arc. These measurements helped to distinguish temporal events from spatial structures, and in doing so provided new insights into auroral processes. The use of global auroral imaging from the POLAR satellite supported the findings from the electric field data and all-sky imagery that the payloads passed through the wake of a westward traveling surge. The surge resulted in a region of high conductivity, low electric field, and many non-structured arc formations. This supports similar electric field observations from the Freja satellite in wake regions. There was one arc that distinguished itself from the others, due to its large, stable structure and the extremely high values of electric field within it. In the process of investigating the electric field data, a shadowing effect was discovered that created anomalous features in the data and cast doubt on the magnitude of the field measurements. A model was created in an attempt to remove the shadow-induced signal from the data, and although the model accurately reproduced the raw data qualitatively, it was found to be quantitatively insufficient to remove the shadowing from the data. Estimates were made on the size of the field due to the shadowing, and the largest estimates, together with the observed field aligned currents, were insufficient to explain the magnitudes of the dc electric field. Thus, it was proposed that the payloads were not measuring a convection electric field. The particle, magnetic field, and electric field data combine to provide a scenario where the payloads passed under a region of both an inverted-V and

S shaped potentials. This explains well the size and direction of the dc electric field, the characteristics of the electron precipitation data, and the small currents derived from the magnetometer data.

Analysis of the electric field data showed a time delay between the payloads in the onset of an increase in the dc electric fields. Comparisons with all-sky images supported the idea that a spatially confined region of fast plasma flow moved across the payload trajectory. Some time later, the entire spatially confined region slowed temporally, showing the extreme usefulness of three point in-situ measurements. The electric field yielded even more richness when the payloads observed different structures in the dc field as well as electrostatic broadband waves near the oxygen cyclotron frequency. The observed waves could not be produced in a homogeneous plasma under the observed conditions, but the shear in the electric field could lower the threshold currents required for wave generation through the IEDD instability mechanism. The estimated values of shear frequency and the properties of the electrostatic waves supported the findings of ion cyclotron wave production through IEDD means in both theoretical simulations and laboratory experiments. Again, the three point measurements allowed for verification of theory that could not have been possible with a single payload measurement.

The successes and findings from the AT II data set prove the usefulness of multiple payload/spacecraft measurements in the aurora. They also may cast some doubt on the results taken from the most common measurement technique for measuring electric fields in the aurora. The need of multi-point measurements is vital for understanding many still unexplained phenomenon and auroral processes. The recent Enstrophy rocket flight and the much anticipated Cluster-II satellite launch hopefully represent the movement toward

continued investigation into the true three dimensional characteristics of fields and shear in the auroral zone.

Bibliography

- [Akasofu, 1981] Akasofu, S.-I., The Aurora, *Amer. Scientist*, 69, 492, Sept.-Oct., 1981.
- [Amatucci, et al., 1994] Amatucci, W. E., M. E. Koepke, J. J. Carroll III, T. E. Sheridan, observation of ion-cyclotron turbulence at small values of magnetic-field-aligned current, *Geophys. Res. Lett.*, 21, 1595, 1994.
- [Amatucci, et al., 1998] Amatucci, W. E., D. N. Walker, G. Ganguli, D. Duncan, J. A. Antoniadis, J. H. Bowles, V. Gavrishchaka, M. E. Koepke, Velocity-shear-driven ion-cyclotron waves and associated transverse ion heating, *J. Geophys. Res.*, 103, 11,711, 1998.
- [Amatucci, 1999] Amatucci, W. E., *private communications*, 1999.
- [Arnoldy, 1999] Arnoldy, R., *private communications*, 1999.
- [Basu, et al., 1988] Basu, Su., Sa. Basu, E. MacKenzie, P. F. Fougere, W. R. Coley, N. C. Maynard, J. D. Winningham, M. Sugiura, W. B. Hanson, W. R. Hoegy, Simultaneous density and electric field fluctuation spectra associated with velocity shears in the auroral oval, *J. Geophys. Res.*, 93, 115, 1998.
- [Baumjohann and Treumann, 1996] Baumjohann, W. and R. A. Treumann, Basic Space Plasma Physics, Imperial College Press, London, 1996.
- [Bering, et al., 1973] Bering, E. A., M. C. Kelley, F. S. Mozer, Split Langmuir probe measurements of current density and electric fields in an aurora, *J. Geophys. Res.*, 78, 2201, 1973.
- [Bering and Mozer, 1975] Bering, E. A. and F. S. Mozer, A measurement of perpendicular current density in an aurora, *J. Geophys. Res.*, 80, 3961, 1975.
- [Birkeland, 1908] Birkeland, K., The Norwegian Auroral Polaris Expedition 1902-1903, Vol. 1, Aschehoug, Christiania, Norway, 1908.
- [Boehm, et al., 1990] Boehm, M., C. W. Carlson, J. P. McFadden, F. S. Mozer, Dual sounding rocket observations of low-altitude electrostatic shocks, *J. Geophys. Res.*, 95, 173, 1990.
- [Boehm, 1999] Boehm, M., *private communications*, 1999.

- [Bonnell, 1997] Bonnell, J., Identification of broadband ELF waves observed during transverse ion acceleration in the auroral ionosphere, Ph.D. dissertation, Cornell University, Ithaca, 1997.
- [Carlson, et al., 1983] Carlson, C., D. W. Curtis, G. Paschmann, W. Michael, An instrument for rapidly measuring plasma distribution functions with high resolution, *Adv. Space Res.*, 2, 67, 1983.
- [Carlson, et al., 1998a] Carlson, C. W., R. F. Pfaff, J. G. Watzin, The Fast Auroral SnapshoT (FAST) mission, *Geophys. Res. Lett.*, 25, 2013, 1998.
- [Carlson, et al., 1998b] Carlson, C. W., J. P. McFadden, R. E. Ergun, M. Temerin, W. Peria, F. S. Mozer, D. M. Klumpar, E. G. Shelley, W. K. Peterson, E. Moebius, R. Elphic, R. Strangeway, C. Cattell, R. Pfaff, FAST observations in the downward auroral current region: Energetic upgoing electron beams, parallel potential drops, and ion heating, *J. Geophys. Res.*, 25, 2017, 1998.
- [Chaston, et al., 1998] Chaston, C. C., R. E. Ergun, G. T. Delory, W. Peria, M. Temerin, C. Cattell, R. Strangeway, J. P. McFadden, C. W. Carlson, R. C. Elphic, D. M. Klumpar, W. K. Peterson, E. Moebius, R. Pfaff, Characteristics of electromagnetic proton cyclotron waves along auroral field lines observed by FAST in regions of upward current, *Geophys. Res. Lett.*, 25, 2057, 1998.
- [Chiu and Schultz, 1978] Chiu, Y. T. and M. Schultz, Self-consistent particle and parallel electrostatic field distributions in the magnetospheric-ionospheric auroral region, *J. Geophys. Res.*, 83, 629, 1978.
- [Chiu and Cornwall, 1980] Chiu, Y. T. and J. M. Cornwall, Electrostatic model of a quiet auroral arc, *J. Geophys. Res.*, 85, 543, 1980.
- [Drozdenco and Morales, 1999] Drozdenco, T. and G. J. Morales, Interaction of a shear Alfvén wave with a filamentary density perturbation in a low- β plasma, submitted to *Physics of Plasmas*, November, 1999.
- [Earle, et al., 1989] Earle, G. D., M. C. Kelley, G. Ganguli, Large velocity shears and associated electrostatic waves and turbulence in the auroral F region, *J. Geophys. Res.*, 94, 15,321, 1989.
- [Erlandson and Zanetti, 1998] Erlandson, R. E. and L. J. Zanetti, A statistical study of auroral electromagnetic ion cyclotron waves, *J. Geophys. Res.*, 103, 4627, 1998.

- [Ergun, et al., 1998] Ergun, R. E., C. W. Carlson, J. P. McFadden, F. S. Mozer, G. T. Delory, W. Peria, C. C. Chaston, M. Temerin, R. Elphic, R. Strangeway, R. Pfaff, C. A. Cattell, D. Klumpar, E. Shelley, W. Peterson, E. Moebius, L. Kistler, FAST observations of electric field structures in the auroral zone, *Geophys. Res. Lett.*, *25*, 2925, 1998.
- [Evans, 1974] Evans, D. S., Precipitating electron fluxes formed by a magnetic field aligned potential difference, *J. Geophys. Res.*, *79*, 2853, 1974.
- [Ganguli, et al., 1985] Ganguli, G., Y. C. Lee, P. J. Palmadesso, Electrostatic ion-cyclotron instability caused by a nonuniform electric field perpendicular to the external magnetic field, *Phys. Fluids*, *28*, 761, 1985.
- [Ganguli, et al., 1988] Ganguli, G., Y. C. Lee, P. J. Palmadesso, Electron-ion hybrid mode due to transverse velocity shear, *Phys. Fluids*, *31*, 2753, 1988.
- [Ganguli, et al., 1994] Ganguli, G., M. J. Keskinen, H. Romero, R. Heelis, T. Moore, C. Pollock, Coupling of microprocesses and macroprocesses due to velocity shear: An application to the low-altitude ionosphere, *J. Geophys. Res.*, *99*, 8873, 1994.
- [Gary, et al., 1995] Gary, J. B., R. A. Heelis, J. P. Thayer, Summary of field-aligned Poynting flux observations from DE2, *Geophys. Res. Lett.*, *22*, 1861, 1995.
- [Gavrishchaka, et al., 1996] Gavrishchaka, V., M. E. Koepke, G. Ganguli, Dispersive properties of a magnetized plasma with a field-aligned drift and inhomogeneous transverse flow, *Phys. Plasmas*, *3*, 3091, 1996.
- [Gavrishchaka, et al., 1997] Gavrishchaka, V. V., M. E. Koepke, G. I. Ganguli, Ion cyclotron modes in a two-ion-component plasma with transverse-velocity shear, *J. Geophys. Res.*, *102*, 11,653, 1997.
- [Haerendel, et al., 1993] Haerendel, G., S. Buchert, C. La Hoz, B. Raaf, E. Rieger, On the proper motion of auroral arcs, *J. Geophys. Res.*, *98*, 6087, 1993.
- [Hallinan, 1981] Hallinan, T., The distribution of vorticity in auroral arcs, *Physics of Auroral Arc Formation*, Geophys. Monograph Series, *25*, Akasofu and Kan, Ed., AGU publications, 1981.
- [Hallinan and Davis, 1970] Hallinan, T. J. and T. N. Davis, Small-scale auroral arc distortions, *Planet. Space Sci.*, *18*, 1735, 1970.

- [Hudson and Mozer, 1978] Hudson, M. K. and F. S. Mozer, Electrostatic shocks, double layers, and anomalous resistivity in the magnetosphere, *Geophys. Res. Lett.*, *5*, 131, 1978.
- [Ivchenko, et al., 1999] Ivchenko, N., G. Marklund, K. Lynch, D. Pietrowski, R. Torbert, F. Primdahl, A. Ranta, Quasi-periodic oscillations observed at the edge of an auroral arc by Auroral Turbulence 2, *Geophys. Res. Lett.*, *26*, 3365, 1999.
- [Kagan, et al., 1996] Kagan, L. M., M. C. Kelley, R. A. Doc, Ionospheric electron heating by structured electric fields: Theory and experiment, *J. Geophys. Res.*, *101*, 10,893, 1996.
- [Kelley, 1989] Kelley, M. C., The Earth's Ionosphere: Plasma Physics and Electrodynamics, Academic Press, San Diego, 1989.
- [Kelley and Carlson, 1977] Kelley, M. C. and C. W. Carlson, Observations of intense velocity shear and associated electrostatic waves near an auroral arc, *J. Geophys. Res.*, *82*, 2343, 1977.
- [Keskinen, et al., 1988] Keskinen, M. J., H. G. Mitchell, J. A. Fedder, P. Satyanarayana, S. T. Zalesak, J. D. Huba, Nonlinear evolution of the Kelvin-Helmholtz instability in the high-latitude ionosphere, *J. Geophys. Res.*, *93*, 137, 1988.
- [Kimball and Hallinan, 1998] Kimball, J. and T. J. Hallinan, A morphological study of black vortex streets, *J. Geophys. Res.*, *103*, 14,683, 1998.
- [Kindel and Kennel, 1971] Kindel, J. M. and C. F. Kennel, Topside current instabilities, *J. Geophys. Res.*, *76*, 3055, 1971.
- [Kinney, et al., 1999] Kinney, R. M., F. V. Coroniti, J. C. McWilliams, P. L. Pritchett, Mechanisms for discrete auroral breakup by nonlinear Alfvén wave interaction, *J. Geophys. Res.*, *104*, 19,931, 1999.
- [Kintner, 1976] Kintner, P. M., Observations of velocity shear driven plasma turbulence, *J. Geophys. Res.*, *81*, 5114, 1976.
- [Kintner and Seyler, 1995] Kintner, P. M. and C. E. Seyler, The status of observations and theory of high latitude ionospheric and magnetospheric plasma turbulence, *Space Science Reviews*, *41*, 91, 1985.
- [Kivelson and Russell, 1995] Kivelson, M. G. and C. T. Russell, Introduction to Space Physics, Cambridge University Press, New York, 1995.
- [Klumpar, 1979] Klumpar, D. M., Transversely accelerated ions: an ionospheric source of hot magnetospheric ions, *J. Geophys. Res.*, *84*, 4229, 1979.

- [Lynch, et al., 1999] Lynch, K. A., D. Pietrowski, R. B. Torbert, N. Ivchenko, G. Marklund, F. Primdahl, Multiple-point electron measurements in a nightside auroral arc: Auroral Turbulence II particle observations, *Geophys. Res. Lett.*, *26*, 3361, 1999.
- [Lyons, 1980] Lyons, L. R., Generation of large-scale regions of auroral currents, electric potentials, and precipitation by the divergence of the convection electric field, *J. Geophys. Res.*, *85*, 17, 1980.
- [Lysak, 1990] Lysak, R. L., Electrodynamic coupling of the magnetosphere and ionosphere, *Space Sci. Rev.*, *52*, 33, 1990.
- [Lysak, 1991] Lysak, R. L., Feedback instability of the ionospheric resonant cavity, *J. Geophys. Res.*, *96*, 1553, 1991.
- [McAdams, et al., 1997] McAdams, K., et al., Initial findings from high frequency wave receivers on the Auroral Turbulence II and PHAZE II sounding rockets, published in the *abstracts of the AGU meeting*, Fall, 1997.
- [Marklund, 1984] Marklund, G., Auroral arc classification scheme based on the observed arc-associated electric field pattern, *Planet. Space Sci.*, *32*, 193, 1984.
- [Marklund, et al., 1998] Marklund, G. T., T. Karlsson, L. G. Blomberg, P.-A. Lindqvist, C.-G. Fälthammar, M. L. Johnson, J. S. Murphree, L. Andersson, L. Eliasson, H. J. Opgenoorth, L. J. Zanetti, Observations of the electric field fine structure associated with the westward traveling surge and large-scale auroral spirals, *J. Geophys. Res.*, *103*, 4125, 1998.
- [Miura, 1987] Miura, A., Simulation of Kelvin-Helmholtz instability at the magnetospheric boundary, *J. Geophys. Res.*, *92*, 3195, 1987.
- [Moore, et al., 1996] Moore, T. E., M. O. Chandler, C. J. Pollock, D. L. Rea-soner, R. L. Arnoldy, B. Austin, P. M. Kintner, J. Bonnell, Plasma heating and flow in an auroral arc, *J. Geophys. Res.*, *101*, 5279, 1996.
- [Mozer, 1973] Mozer, F. S., Analysis of techniques for measuring dc and ac electric fields in the magnetosphere, *Space Sci. Rev.*, *14*, 272, 1973.
- [Mozer, 1981] Mozer, F. S., The low altitude electric field structure of discrete auroral arcs, *Physics of Auroral Arc Formation*, Geophys. Monograph Series, *25*, S.-I. Akasofu and J. R. Kan, Ed., AGU publications, 1981.

- [Mozer, et al., 1979] Mozer, F. S., C. A. Cattell, M. Temerin, R. B. Torbert, S. Von Glinski, M. Woldorff, J. Wygant, The dc and ac electric field, plasma density, plasma temperature, and field-aligned current experiments on the S3-3 satellite, *J. Geophys. Res.*, *84*, 5875, 1979.
- [Peñano and Ganguli, 1999] Peñano, J. R. and G. Ganguli. Ionospheric source for low-frequency broadband electromagnetic signatures, *Phys. Rev. Lett.*, *83*, 1343, 1999.
- [Peñano and Ganguli, 1999b] Peñano, J. R. and G. Ganguli, Generation of ELF electromagnetic waves in the ionosphere by localized transverse dc electric fields: subcyclotron frequency, submitted to *J. Geophys. Res.*, 1999.
- [Perkins and Doles, 1975] Perkins, F. W. and J. H. Doles, Velocity shear and the $\mathbf{E} \times \mathbf{B}$ instability, *J. Geophys. Res.*, *80*, 211, 1975.
- [Primdahl, 1997] Primdahl, F., Sounding rocket payload kinematics, Sounding Rocket Magnetometer Data Analysis Workshop, CU. 17-18 Nov., 1997.
- [Pritchett, 1993] Pritchett, P. L., Simulation of collisionless electrostatic velocity-shear-driven instabilities, *Phys. Fluids B*, *5*, 3770, 1993.
- [Reiff, 1984] Reiff, P., Models of auroral-zone conductances, *Magnetospheric Currents*, Geophys. Monograph Series, **28**, T. A. Potemra, Ed., AGU publications, 1984.
- [Rönmark, 1983] Rönmark, K., Computation of the dielectric tensor of a Maxwellian plasma, *Plasma Physics*, *25*, 699, 1983.
- [Sharp, et al., 1977] Sharp, R. D., R. G. Johnson, E. G. Shelley, Observation of an ionospheric acceleration mechanism producing energetic (keV) ions primarily normal to the geomagnetic field direction, *J. Geophys. Res.*, *82*, 3324, 1977.
- [Stenbaek-Nielsen and Hallinan, 1979] Stenbaek-Nielsen, H. C. and T. J. Hallinan, Pulsating aurora: evidence for noncollisional thermalization of precipitating electrons, *J. Geophys. Res.*, *84*, 3257, 1979.
- [Swift, et al., 1976] Swift, D. W., H. C. Stenbaek-Nielsen, T. J. Hallinan, An equipotential model for auroral arcs, *J. Geophys. Res.*, *81*, 3931, 1976.
- [Temerin, et al., 1981] Temerin, M., M. H. Boehm, F. S. Mozer, Paired electrostatic shocks, *Geophys. Res. Lett.*, *8*, 799, 1981.

- [Tetreault, 1991] Tetreault, D., Theory of electric fields in the auroral acceleration region, *J. Geophys. Res.*, *96*, 3549, 1991.
- [Torbert, 1990] Torbert, R. B., Auroral Turbulence Project Initiation Conference Presentation, Jan. 19, 1990.
- [Trondsen and Cogger, 1997] Trondsen, T. S. and L. L. Cogger, High-resolution television observations of black aurora, *J. Geophys. Res.*, *102*, 363, 1997.
- [Walker, et al., 1997] Walker, D. N., W. E. Amatucci, G. Ganguli, J. A. Antoniadis, J. H. Bowles, D. Duncan, V. Gavrishchaka, M. Koepke, Perpendicular ion heating by velocity-shear-driven waves, *Geophys. Res. Lett.*, *24*, 1187, 1997.
- [Wahlund, et al., 1998] Wahlund, J.-E., A. I. Eriksson, B. Holback, M. H. Boehm, J. Bonnell, P. M. Kintner, C. E. Seyler, J. H. Clemmons, L. Eliasson, D. J. Knudsen, P. Norqvist, L. J. Zanetti, Broadband ELF plasma emission during auroral energization 1. Slow ion acoustic waves, *J. Geophys. Res.*, *103*, 4343, 1998.
- [Yamamoto, et al., 1994] Yamamoto, T., M. Ozaki, S. Inoue, K. Makita, C.-I. Meng, Convective generation of "giant" undulations on the evening diffuse auroral boundary, *J. Geophys. Res.*, *99*, 19,499, 1994.
- [Yau, et al., 1983] Yau, A. W., B. A. Whalen, A. G. McNamara, P. J. Kellogg, W. Bernstein, Particle and wave observations of low-altitude ionospheric ion acceleration events, *J. Geophys. Res.*, *88*, 341, 1983.

Appendices

Appendix A

Electric Field Despinning and Rotation

In order to get the electric field data in a form that is easily manipulated and useful, the raw data from the potential spheres need to be calibrated, despun, and oriented in a known coordinate system. The next sections outline this process from obtaining the raw data to viewing the electric field in the perp- \vec{B} plane.

A.1 Raw Data

In order to calculate an electric field, data from two opposing spheres must be read in:

$$E = \frac{V_2 - V_1}{d} \quad (\text{A.1.1})$$

where V is the potential measured by the sphere and d is the distance between the two spheres. The raw data come in the form of two ten-bit words for each potential sphere, a high and a low bit word. The high bit is multiplied by 2^{10} and added to the low bit to obtain the correct raw data values. In telemetry, an offset of 524288, or $\frac{2^{20}}{2}$, is added to ensure all positive numbers during transmission, and this value is subtracted from the data values.

A.2 Gains, Offsets, and Despinning

A.2.1 Gains and Offsets

Now that the raw data has been converted from two ten bit, positive words to one word with the correct sign, the proper gains and offsets must be applied. The offset subtracted already is a numerical offset: that is, regardless of the minimum value, 524288 was added to all values. There may also be an electronic offset as well, caused by a floating zero point during the flight. Therefore, another offset must be calculated and applied to the data set.

The data are worked through an FFT and all frequencies above the spin frequency (approximately 1 Hz) are filtered out. This is to remove any wave signatures or other high frequency signals so that the main component remaining is the spin signature. Then, the result is boxcar averaged to determine the time-dependent dc offset of the data. This is the secondary offset that, when subtracted from the data, will yield a signal that is perfectly oscillatory about zero.

The offset taken care of, our attention is now turned toward the appropriate gains and numerical conversions into useful units. Calibration data from Cornell University showed that the actual gains of the spheres themselves were less than one percent different from the nominal value, so there were no apparent gain errors associated with the spheres themselves. The nominal range of the potential spheres is ± 4.096 V, so this value is multiplied into our data array. Also, to convert the number from telemetry values, 2^{19} must be divided out to yield the correct range of numerical values. Next, when the telemetry system was originally created, it was set for a dynamic range of ± 2.5 V which was deemed too small a range for this particular experiment, so a gain of 1.64 was added to the signal, which is at this point

divided out. Now, the data is in an almost complete state. In order to now obtain the electric field, the sphere separation, d , must be divided out. The data are now in the appropriate form : electric field data in units of $\frac{V}{m}$, oscillating about zero with the correct numerical values. This process of data conversion is summed up in Equations A.2.1 and A.2.2 .

$$\begin{aligned} \text{Offset Data} &= (\text{low bit} + 2^{10} \times \text{high bit}) - 524288 \\ &- (\text{high pass FFT}((\text{low bit} + 2^{10} \times \text{high bit}) - 524288)) \quad (\text{A.2.1}) \end{aligned}$$

$$E (V/m) = \frac{(\text{Offset Data}) \times 4.096}{2^{19} \times 1.64 \times 3} \quad (\text{A.2.2})$$

The final step in obtaining the full electric field value is obtaining the spin axis component. If we consider two pairs of opposed spheres, we can calculate the electric field in a plane perpendicular to the spin axis of the payload. These two dimensions are referenced in the spinning frame of the payload, with the y-axis along the launch lug, and the x axis in the direction such that when crossed into the y axis will yield the z axis along the payload spin axis. In order to get the spin axis component of the electric field so we have a three dimensional field value, we utilize the magnetic field. Once the magnetic field is read in and appropriately converted into the proper units, amplitudes, and spacecraft coordinates, we make the assumption that $\vec{E} \cdot \vec{B} = 0$. Having the x, y, and z components of the magnetic field, and the x and y components of the electric field, it is a simple matter to obtain the third electric field component and thus have the entire three dimensional electric and magnetic field vector. At this point, the $\vec{v} \times \vec{B}$ electric field is still in the data, and needs to be removed. We will do this after the data are in a more convenient coordinate system.

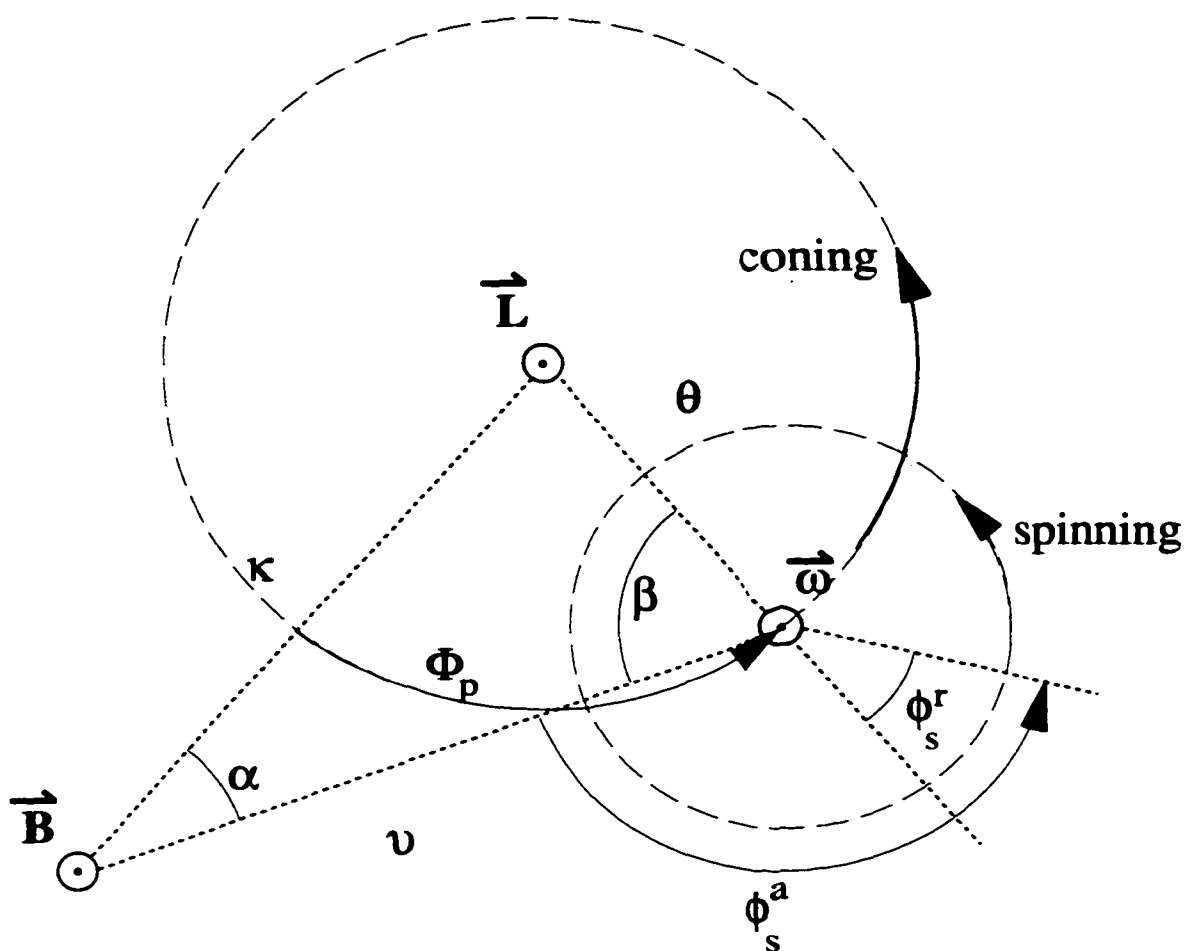


Figure A-1: The \vec{B} , \vec{L} , $\vec{\omega}_s$ spherical triangle.

A.2.2 Despinning

At this stage, the data need to be despun to remove the payload spinning and coning signatures. Rather than fitting the data to sine waves, we choose to use the magnetometer data to despin the data. This procedure was developed by F. Primdahl [Primdahl, 1997], and is based on Figure A-1. When a payload undergoes free body motion, it can be characterized by its spinning and coning about the body spin axis and angular momentum vector, and about the magnetic field. In Figure A-1, the magnetic field (\vec{B}), the angular

momentum (\vec{L}), and the angular frequency ($\vec{\omega}_s$) are shown coming out of the page. κ is the angle between \vec{L} and \vec{B} , ν is the angle between \vec{B} and $\vec{\omega}_s$, and θ is the angle between \vec{L} and $\vec{\omega}_s$. The observed spin phase angle of the payload is given by

$$\phi_s^a = (180^\circ - \beta) + \phi_s^r \quad (\text{A.2.3})$$

which is in turn modulated by the coning phase, Φ_p , through

$$\tan(180^\circ - \beta) = \frac{\sin\Phi_p/\cos\theta}{\cos\Phi_p - \tan\theta/\tan\kappa} \quad (\text{A.2.4})$$

The magnetic field components in the frame of the spinning and coning payload are then given by

$$B_1 = B\{(\cos\theta \sin\kappa \cos\Phi_p - \sin\theta \cos\kappa)\cos\phi_s^r - \sin\kappa \sin\Phi_p \sin\phi_s^r\} \quad (\text{A.2.5})$$

$$B_2 = B\{-(\cos\theta \sin\kappa \cos\Phi_p - \sin\theta \cos\kappa)\sin\phi_s^r - \sin\kappa \sin\Phi_p \cos\phi_s^r\} \quad (\text{A.2.6})$$

$$B_3 = B\{\sin\theta \sin\kappa \cos\Phi_p + \cos\theta \cos\kappa\} \quad (\text{A.2.7})$$

The magnetometers will yield values for the three components in the frame of the payload, and from them θ , κ , Φ_p , and ϕ_s^r can be obtained. These values can then be used to rotate the electric field data into an $-\vec{B}$, $\perp\vec{B}$ away from \vec{L} , $-\vec{B} \times (\perp\vec{B}$ away from \vec{B}) coordinate system, which we address in the next section.

A.3 Rotation Into Specified Coordinate Systems

We now have the electric field data with the correct gains and offsets applied, and we know from the magnetometer data the values of θ , κ , Φ_p , and ϕ_s^r as functions of time. We can

now rotate the electric field data from the payload inertial frame to an $-\vec{B}$, $\perp\vec{B}$ away from \vec{L} , $-\vec{B} \times (\perp\vec{B}$ away from $\vec{L})$ coordinate system. The first rotation is about the spin axis, z , by ϕ_s^r to remove the spin phase.

$$\begin{pmatrix} e_x' \\ e_y' \\ e_z' \end{pmatrix} = \begin{pmatrix} e_x \\ e_y \\ e_z \end{pmatrix} \begin{pmatrix} \cos(-\phi_s^r) & -\sin(-\phi_s^r) & 0 \\ \sin(-\phi_s^r) & \cos(-\phi_s^r) & 0 \\ 0 & 0 & 1 \end{pmatrix} \quad (\text{A.3.1})$$

Next, we perform a rotation about the y' axis by an amount θ to get an axis along \vec{L} instead of along $\vec{\omega}_s$.

$$\begin{pmatrix} e_x'' \\ e_y'' \\ e_z'' \end{pmatrix} = \begin{pmatrix} e_x' \\ e_y' \\ e_z' \end{pmatrix} \begin{pmatrix} \cos(-\theta) & 0 & -\sin(-\theta) \\ 0 & 1 & 0 \\ \sin(-\theta) & 0 & \cos(-\theta) \end{pmatrix} \quad (\text{A.3.2})$$

The next rotation is by Φ_p about the z'' axis to get an axis directed away from \vec{L} .

$$\begin{pmatrix} e_x''' \\ e_y''' \\ e_z''' \end{pmatrix} = \begin{pmatrix} e_x'' \\ e_y'' \\ e_z'' \end{pmatrix} \begin{pmatrix} \cos(-\Phi_p) & -\sin(-\Phi_p) & 0 \\ \sin(-\Phi_p) & \cos(-\Phi_p) & 0 \\ 0 & 0 & 1 \end{pmatrix} \quad (\text{A.3.3})$$

The final rotation is about the y''' axis by κ to get one axis along $-\vec{B}$, and keep another $\perp\vec{B}$ away from \vec{L} .

$$\begin{pmatrix} e_{-\vec{B}} \\ e_{\perp\vec{B}\text{awayfrom}\vec{L}} \\ e_{-\vec{B} \times \perp\vec{B}\text{awayfrom}\vec{L}} \end{pmatrix} = \begin{pmatrix} e_x''' \\ e_y''' \\ e_z''' \end{pmatrix} \begin{pmatrix} \cos\kappa & 0 & -\sin\kappa \\ 0 & 1 & 0 \\ \sin\kappa & 0 & \cos\kappa \end{pmatrix} \quad (\text{A.3.4})$$

component	symbol	value
North outward	L_{No}	-0.383464
North northward	L_{Nno}	0.919511
North eastward	L_{Ne}	-0.08634
East outward	L_{Eo}	0.14495
East northward	L_{Eno}	0.93009
East eastward	L_{Ee}	0.337510

Table A.1: Components of $\frac{\vec{L}}{L}$ for subpayloads

Now, with knowledge about the ambient magnetic field, we can rotate the electric field data again to another, more useful frame : $-\vec{B}$, $\perp\vec{B}$ plane, where the $\perp\vec{B}$ plane is referenced relative to geographic coordinates. The magnetometer data used are referenced in a frame of components of \vec{L} northward, eastward, and outward. The values for the subpayloads of these components of a unit vector in the \vec{L} direction are determined using the magnetometers and are shown in Table A.1.

The data would be more easily manipulated in a north, east, up coordinate system, where up would be anti-parallel to \vec{B} . This means that we can rotate \vec{L} about the east direction by taking into account the curvature of the Earth at varying latitudes throughout the flight. The rotation is performed by the following:

$$\begin{pmatrix} L_n \\ L_e \\ L_u \end{pmatrix} = \begin{pmatrix} L_{no} \\ L_e \\ L_o \end{pmatrix} \begin{pmatrix} \cos(\text{latitude}) & 0 & -\sin(\text{latitude}) \\ 0 & 1 & 0 \\ \sin(\text{latitude}) & 0 & \cos(\text{latitude}) \end{pmatrix} \quad (\text{A.3.5})$$

which holds for both subpayloads. We now know the direction of \vec{L} in a north, east, up coordinate system, and we have the electric field data in an $-\vec{B}$, $\perp\vec{B}$ away from \vec{L} , $-\vec{B} \times (\perp\vec{B}$ away from \vec{L}) coordinate system. We also have magnetometer data in a right-handed north,

west, up coordinate system, which is a simple rotation from north, east, up. We now wish to rotate into a $\perp \vec{B}$ geographic system. The z axis will be $-\vec{B}$ and we are free to choose the directions of x and y in the plane that is $\perp \vec{B}$. We choose x to be $\perp \vec{B}$ with no westward component. This means that the x axis will be mostly northward with a small upward component. We assign unit vectors of this new coordinate system with respect to the old coordinate system:

$$\hat{e}_3 = \frac{B_n}{B} \hat{n} + \frac{B_w}{B} \hat{w} + \frac{B_u}{B} \hat{u} \quad (\text{A.3.6})$$

$$\hat{e}_1 = \frac{B_u}{B} \hat{n} - \frac{B_n}{B} \hat{u} \quad (\text{A.3.7})$$

$$\hat{e}_2 = -\frac{B_w B_n}{B^2} \hat{n} + \frac{(1 - B_w^2)}{B^2} \hat{w} - \frac{B_w B_u}{B^2} \hat{u} \quad (\text{A.3.8})$$

where E3 is along $-\vec{B}$, E1 is along the x axis, E2 is along the y axis, B_n , B_e , and B_u are the north, west, and up components of the magnetic field, and B is the magnitude of the magnetic field.

To determine the angle east of north of \vec{L} , we need to compute α through

$$\alpha = \text{atan}\left(\frac{L_2}{L_1}\right) \quad (\text{A.3.9})$$

$$L_2 = \vec{L} \cdot \hat{e}_2 \quad (\text{A.3.10})$$

$$L_1 = \vec{L} \cdot \hat{e}_1 \quad (\text{A.3.11})$$

which transforms the old \vec{L} into the new coordinate system. We now rotate the data through this angle α to determine the true orientation of the spin axis in the $\perp\vec{B}$ plane so that our x axis is northward and slightly upward, as per Equation A.3.7, z is \parallel to $-\vec{B}$, and y is the third component, with a direction shown in Equation A.3.8.

At this stage, we can subtract the $\vec{v}\times\vec{B}$ drift. Radar tracking of the Main payload from Poker Flat gives the velocity of the payload in north, west, up coordinates. The differences in velocities between the three payloads due to their ejection velocities are orders of magnitude smaller than the main northward velocity component. Therefore, the radar tracking data from the Main payload was used as the velocity vector for all three payloads. Since \vec{B} is also in a north, west, up system, it is trivial to calculate $\vec{v}\times\vec{B}$ and subtract it from the electric field vector. We now have the electric field data in a $\perp\vec{B}$, well-defined coordinate system. From here, it is easy to rotate into arc aligned coordinates, by simply rotating the data by the angle the arc makes with the northward direction, which can be determined by viewing the all-sky images.

Appendix B

Payload Shadow Model

B.1 Model Framework

Field aligned precipitating electrons in an auroral arc are blocked by a payload traveling through the region where the arc exists and as a result a shadow forms under the spacecraft. This shadow region is devoid of the hot field aligned electrons found elsewhere near the payload. This region of space that is positively charged with respect to the surrounding plasma can influence the measurement of electric fields. Below we present the model used to understand the shadow effects on the electric field data presented in the main text.

The model is based on the Figure B-1. Vertically up in the diagram is anti-parallel to the magnetic field direction. The axes are marked on the figure, with the z axis out of the page. The payload is shown broken into three sections of length. Assuming the payload is in a region of electron precipitation, each length casts a shadow of a width that is dependent upon its radius. The length of the shadow is determined by using the velocity of the payload through the arc, the length of the payload projected into the perp- \vec{B} plane, and the velocity of the precipitating electrons. The time it takes for the payload to pass over a specific region of space will equal the time taken by the last unshielded electrons to reach the bottom of the shadow, or,

$$t = \frac{l \sin(\theta)}{v_p} = \frac{L}{v_e} \quad (\text{B.1.1})$$

where l is the length of the payload, θ is the angle that the payload spin axis makes with

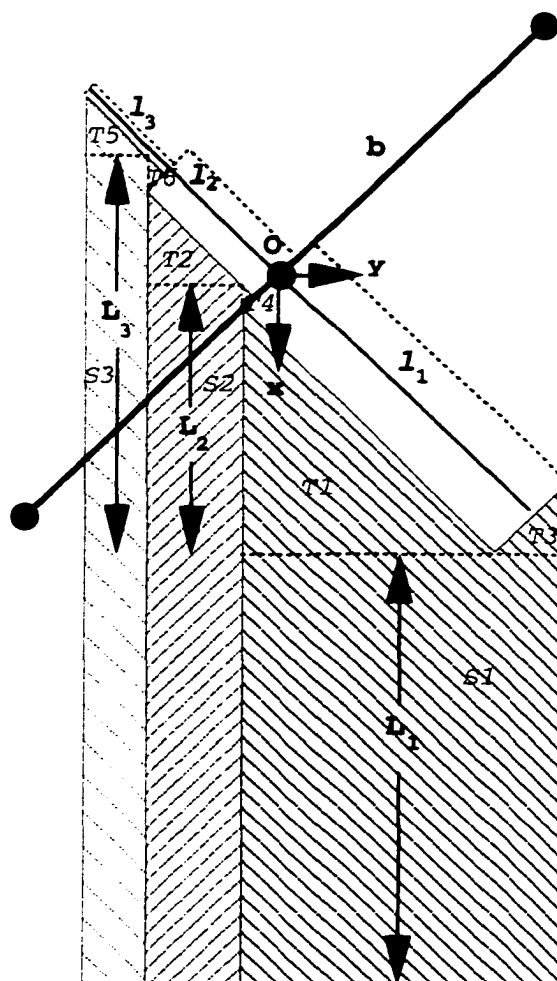


Figure B-1: Schematic of the payload and shadow. The magnetic field is parallel to the x-axis in the figure.

the magnetic field, v_p is the payload velocity, L is the length of the shadow, and v_e is the speed of the precipitating electrons. It should be noted that the lengths of the shadows in the figure are not drawn to scale, as they are on the order of 10^5 meters, whereas the dimensions of the shadow in the $\text{perp-}\vec{B}$ plane are on the order of 1 m. These shadows are assumed to be three dimensional slabs of charge, with a positive charge density created by the lack of precipitating electrons with respect to surrounding regions.

The problem now becomes one of determining the potential at the location of the sphere

at the end of the boom and allowing the sphere to rotate around the origin upon the booms. We can simply use the integral form of Poisson's equation,

$$V = k \int \frac{dq}{r} \quad (\text{B.1.2})$$

where V is the potential,

$$k = \frac{1}{4\pi\epsilon_0} \quad (\text{B.1.3})$$

in MKS units, dq is the infinitesimal charge and r is the scalar distance from the infinitesimal charge element to the potential sphere. We choose the origin of our coordinate system to be at the dividing point between the payload section of length l_1 and l_2 , and along the spin axis of the payload. We do not need to concern ourselves with the potential measured by the spheres due to induced or surface charges on the spacecraft itself, as the potential difference between the two spheres, the real quantity of interest, will cancel out any potential from payload charging due to the symmetry of the problem.

We now solve for the slabs of charge that reside below the payloads. The slabs are broken into regions of both square and triangular volumes to ease in the numeric computation of Poisson's integral. Each section of shadow volume has the same associated charge density. This charge density, ρ , is equal to the unit charge times the beam number density of precipitating electrons that would have filled in the region were the payload absent. The spatial extent of each shadow segment in the perp- \vec{B} plane is dependent upon the physical geometry of the payload. Table B.1 lists the payload dimensions useful in determining shadow extent.

These payload dimensions will yield the limits of integration for the volumes in the integration. We now look more closely at the integration and limits of the problem. We

symbol	quantity	length (m)
r_1	radius of lower section	0.219
r_2	radius of middle section	0.190
r_3	radius of upper section	0.0508
l_1	length of upper section	1.18
l_2	length of middle section	0.550
l_3	length of middle section	0.432

Table B.1: Payload Dimensions.

can rewrite Poisson's equation, using our now defined coordinate system, as

$$V = \rho k \int \int \int \frac{\partial x \partial y \partial z}{\sqrt{(x - x_0)^2 + (y - y_0)^2 + (z - z_0)^2}} \quad (\text{B.1.4})$$

where ρ is the charge density, and x_0, y_0 , and z_0 are the coordinates of the potential sphere.

The limits of the integration are obtained through geometry and are listed in Table B.2.

The integrations are performed with the above integrand and limits using iterated Gaussian quadrature. Each volume is computed separately and the results are added together. The position of the potential sphere is varied after each integration is completed to mimic the sphere spinning in space. The positions are based on the tip angle of the payload axis in relation to the magnetic field, θ , which for the East payload was 25° and for the North was 47° .

B.2 Model Approximations

The limits of the integration should be solely based on the payload dimensions since the Debye length for this data set is on the order of 10 cm. However, it has been seen on prior rocket flights [Arnoldy, 1999] that the actual in-situ Debye length can be very different from the theoretical value. In order to create a shadow model consistent with the data, the extent

Volume	x_{min} (m)	x_{max} (m)
S1	$l_1 \cos\theta + r_1 \sin\theta$	$l_1 \cos\theta + r_1 \sin\theta + L$
S2	$r_1 \sin\theta - \frac{r_1 - r_2}{\sin\theta}$	$r_1 \sin\theta - \frac{r_1 - r_2}{\sin\theta} + L$
S3	$-l_2 \cos\theta + r_2 \sin\theta - \frac{r_2 - r_3}{\sin\theta}$	$-l_2 \cos\theta + r_2 \sin\theta - \frac{r_2 - r_3}{\sin\theta} + L$
T1	$r_1 \sin\theta$	$l_1 \cos\theta + r_1 \sin\theta$
T2	$-l_2 \cos\theta + r_2 \sin\theta$	$r_1 \sin\theta - \frac{r_1 - r_2}{\sin\theta}$
T3	$l_1 \cos\theta - r_1 \sin\theta$	$l_1 \cos\theta + r_1 \sin\theta$
T4a	$r_1 \sin\theta - \frac{r_1 - r_2}{\sin\theta}$	$r_2 \sin\theta$
T4b	$r_2 \sin\theta$	$r_1 \sin\theta$
T5	$-(l_2 + l_3) \cos\theta + r_3 \sin\theta$	$-l_2 \cos\theta + r_2 \sin\theta - \frac{r_2 - r_3}{\sin\theta}$
T6a	$-l_2 \cos\theta + r_2 \sin\theta - \frac{r_2 - r_3}{\sin\theta}$	$-l_2 \cos\theta - r_3 \sin\theta$
T6b	$-l_2 \cos\theta - r_3 \sin\theta$	$-l_2 \cos\theta + r_2 \sin\theta$

Volume	y_{min} (m)	y_{max} (m)	z_{min} (m)	z_{max} (m)
S1	$-r_1 \cos\theta$	$l_1 \sin\theta + r_1 \cos\theta$	$-r_1$	r_1
S2	$-l_2 \sin\theta - r_2 \cos\theta$	$-r_1 \cos\theta$	$-r_2$	r_2
S3	$-(l_2 + l_3) \sin\theta - r_3 \cos\theta$	$-l_2 \sin\theta - r_2 \cos\theta$	$-r_3$	r_3
T1	$-r_1 \cos\theta$	$x \tan\theta$	$-r_1$	r_1
T2	$-l_2 \sin\theta - r_2 \cos\theta$	$x \tan\theta$	$-r_2$	r_2
T3	$l_1 \sin\theta - r_1 \cos\theta$	$\frac{x}{\tan\theta}$	$-r_1$	r_1
T4a	$-r_1 \cos\theta$	$-x \tan\theta$	$-r_2$	r_2
T4b	$-r_1 \cos\theta$	$-\frac{x}{\tan\theta}$	$-r_2$	r_2
T5	$-(l_2 + l_3) \sin\theta - r_3 \cos\theta$	$x \tan\theta$	$-r_3$	r_3
T6a	$-l_2 \sin\theta - r_2 \cos\theta$	$x \tan\theta$	$-r_3$	r_3
T6b	$-l_2 \sin\theta - r_2 \cos\theta$	$\frac{x}{\tan\theta}$	$-r_3$	r_3

Table B.2: Integration Limits.

of the shadow was increased to create an increased shadow field that will more accurately reflect actual shadow effects. This was done to both payloads to maintain consistency. Table B.3 shows the amplitude of the shadow field in mV/m for a fixed beam density of $5 \times 10^6 \text{ m}^3$ for different multipliers of the y and z shadow dimensions. Given a multiplier in the y and z dimensions of 2.6, the shadow reaches a maximum value over four times the magnitude solely based on geometrical limitations. Equally important is the fact that for this multiplier, the East payload spheres are not directly in the shadow field at any time, while the North payload spheres do enter the shadow region for a significant amount of

Y mult	1.0	1.1	1.2	1.3	1.4	1.5	1.6	1.7	1.8	1.9
Z mult										
1.0	8.23									
1.1		9.60								
1.2			11.1							
1.3				12.7						
1.4					14.4					
1.5						16.2				
1.6							18.0			
1.7								19.9		
1.8									21.7	
1.9										23.6
Y mult	2.0	2.1	2.2	2.3	2.4	2.5	2.6	2.7	2.8	2.9
Z mult										
2.0	25.5									
2.1		27.4								
2.2			29.3							
2.3				31.2						
2.4					33.1					
2.5						35.1				
2.6							37.0			
2.7								39.0		
2.8									40.9	
2.9										42.9

Table B.3: Maximum Electric Potential Difference as a Function of Shadow Dimensions (mV/m) with $n = 5 \times 10^6$ for the North Payload.

time. While physically being in the shadow would cause severe steepening of the waveform as measured by the spinning sphere, there are effects observed even when the sphere is very near the charge region. Therefore, since the data show very little shadow effects on the East payload, while showing large effects on the North, a balance needs to be struck between enlarging the shadow dimensions to get increased effect and keeping the dimensions small enough such that the East payload data would not have spikes introduced to it. With this in mind, the 2.5 multiplier was chosen as the best value to attain this balance.

It was also found that due to the r^{-1} dependence of the integrand, the shadow length, L , was relatively independent of payload axis angle θ . As a matter of fact, the length of the shadow can be reduced to 1700 m, a factor of 100 less than the length given by Equation B.1.1, with less than a 1% change in the calculated shadow potential. In order to decrease significantly the calculation time and increase the resolution of the Gaussian quadrature method, the shadow lengths for both payloads were set at 1700 m.

Next, we consider the beam density used as a multiplicative factor in the integrand in Equation B.1.4. In order to calculate the charge density in the shadow region, the particle data was used to calculate the electron distribution function comprising the beam:

$$f_e = \frac{m^2}{2E^2} \frac{dJ_E}{dEd\Omega} \quad (\text{B.2.1})$$

$$CR = \frac{2}{m^2} f E^2 H \quad (\text{B.2.2})$$

$$H = \frac{dE}{E} A d\Omega \quad (\text{B.2.3})$$

It is evident from the measured electron data that some of the electrons in the beam were above the upper limit energy threshold of the detectors (see Figure 3-14). When considering the electric field data, it is seen that the regions of strongest effect of the shadow correlates with regions where the peak in the electron beam is above this threshold. At these times, the beam density inferred by the particle data (which is used to determine the charge density that makes up the shadow region) is not an accurate representation of the true environment. The process outlined in Appendix C shows the process used to determine the amount of excluded particles. The peak energy of the beam particles was approximated to maximize the effect of the shadow field, while at the same time limiting the peak energy

to 18 keV. This limit was chosen to keep the peak energy realistic in consideration with typical maximum auroral energies of aurora of similar intensity and duration.

B.3 Model Results

We now present the results obtained from the modeling effort. Figures B-2 and B-3 show the modeled resulting potential difference signal measured by two opposing electric field spheres for the North payload (tipped 47° with respect to \vec{B}) and the East payload (tipped 25° with respect to \vec{B}). The time scale corresponds to the actual rocket flight time when the payloads enter the large stable arc at roughly T+300 seconds, and exit at T+400 seconds, and takes into account the measured electron precipitation. Note that the vertical scale of Figure B-3 has less than half the dynamic range of Figure B-2. The differences in shapes of the two graphs illustrate the differences in electron energy fluxes as actually observed by the two payloads. The sudden jumps represent changes in electron precipitation. These are modeled, using the method in Appendix C, as simple step functions of the electron beam peak energy from one energy step of the detector to another. Despite these differences in shape it is clear from the two payload models that the North payload sees a higher potential difference than the East payload, at times as much as three times the East payload. These differences in magnitude are evident even without accounting for slight differences in measured particle precipitation.

Figures B-4 and B-5 show enlargements of the previous figures. In addition, a perfect sinusoid, of roughly equal magnitude to each shadow potential difference signal, is overplotted for comparison. It is evident that the North payload spheres, which are closer to the actual shadow region for a longer period of time, measure a signal that is significantly

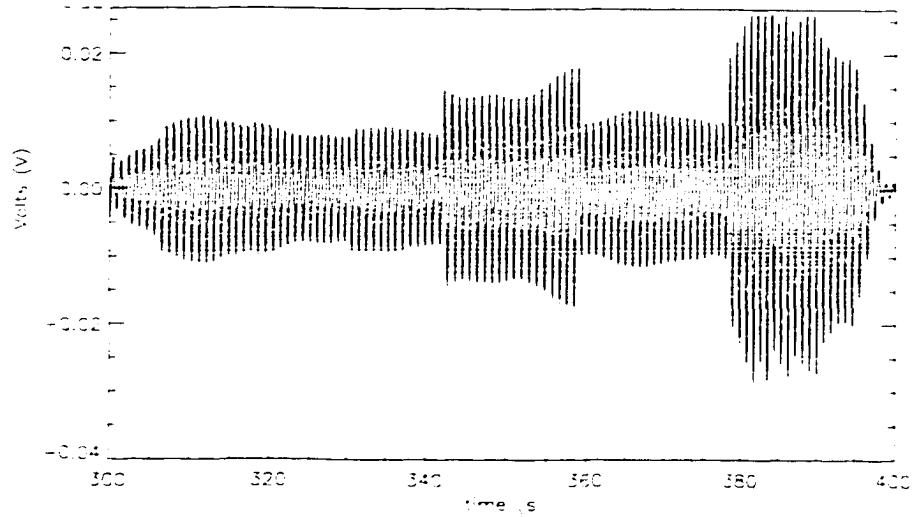


Figure B-2: Potential difference resulting from shadow region as would measured by the North payload.

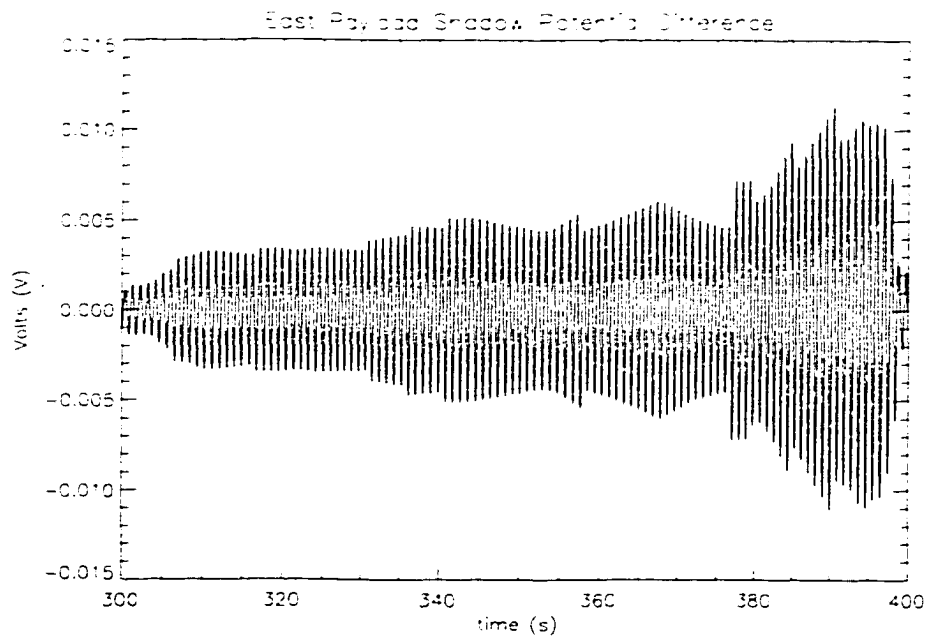


Figure B-3: Potential difference resulting from shadow region as would measured by the East payload.

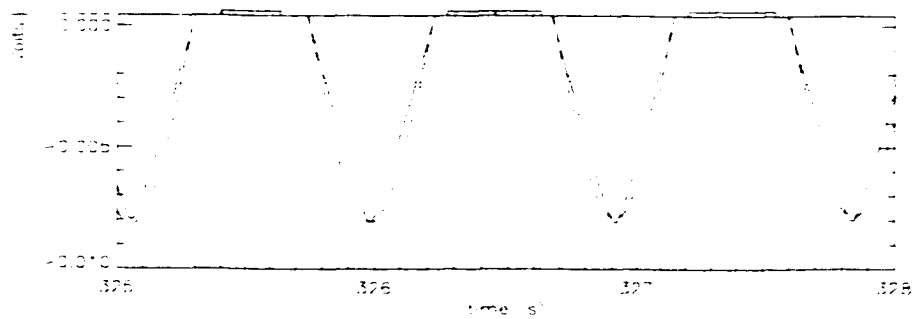


Figure B-4: Potential difference of North payload shadow region. The dashed line shows a perfect sinusoidal signal.

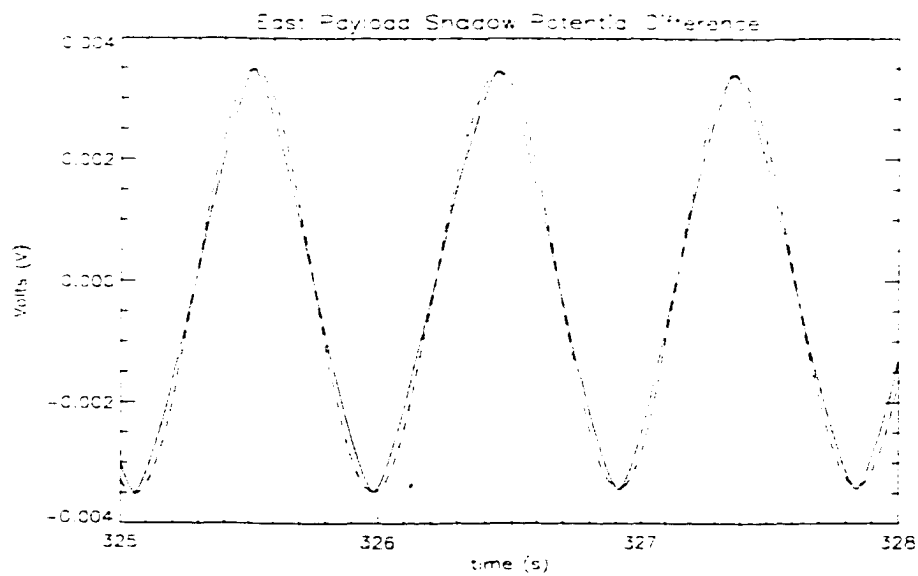


Figure B-5: Potential difference of East payload shadow region. The dashed line shows a perfect sinusoidal signal.

less sinusoidal than the East payload. The non-sinusoidal nature of the shadow potential difference is what ultimately may cause the bumps and spikes in the observed data set. Let us consider the effects of adding this signal, due to the shadow potential, to a perfect sinusoid, which one would expect the spheres to measure as the payload passed through a region of dc electric field.

An ambient, dc electric field would have some arbitrary direction and magnitude. In the frame of a spinning spacecraft, the direction of the electric field would be observed, as a function of time, as a phase. Therefore, the resulting signal of the shadow region can be added to the potential due to a dc electric field with arbitrary amplitude and phase, with respect to the shadow signal. In Figure B-6, we show this addition for a case where the amplitude of the potential due to the ambient electric field is equal in magnitude to the potential due to the shadow region, over a time scale that would correspond to ten seconds of flight time. The different panels in Figure B-6 represent different phases of the ambient electric field, or equivalently, different orientations of the ambient field with respect to the payload. Here we note that in Panel (a), the addition of the signals in phase gives a resultant signal that has the largest amplitude and is nearest to sinusoidal. Panel (b) shows the ambient potential signal leading the shadow signal by 45° . Here, the resulting signal looks like a breaking water wave on a beach, concave on one side and convex on the other. If the ambient signal leads by 90° , as in Panel (c), there are remnants of the breaking wave feature, but the signal is reduced in amplitude, and looks abnormally compressed. Panel (d) shows the good evidence of a "spike on bump" feature. This comes as a result of the ambient signal leading the shadow by 140° . It is important to note that only a non-sinusoidal signal, such as that from the shadow potential, added to the ambient sinusoidal signal can

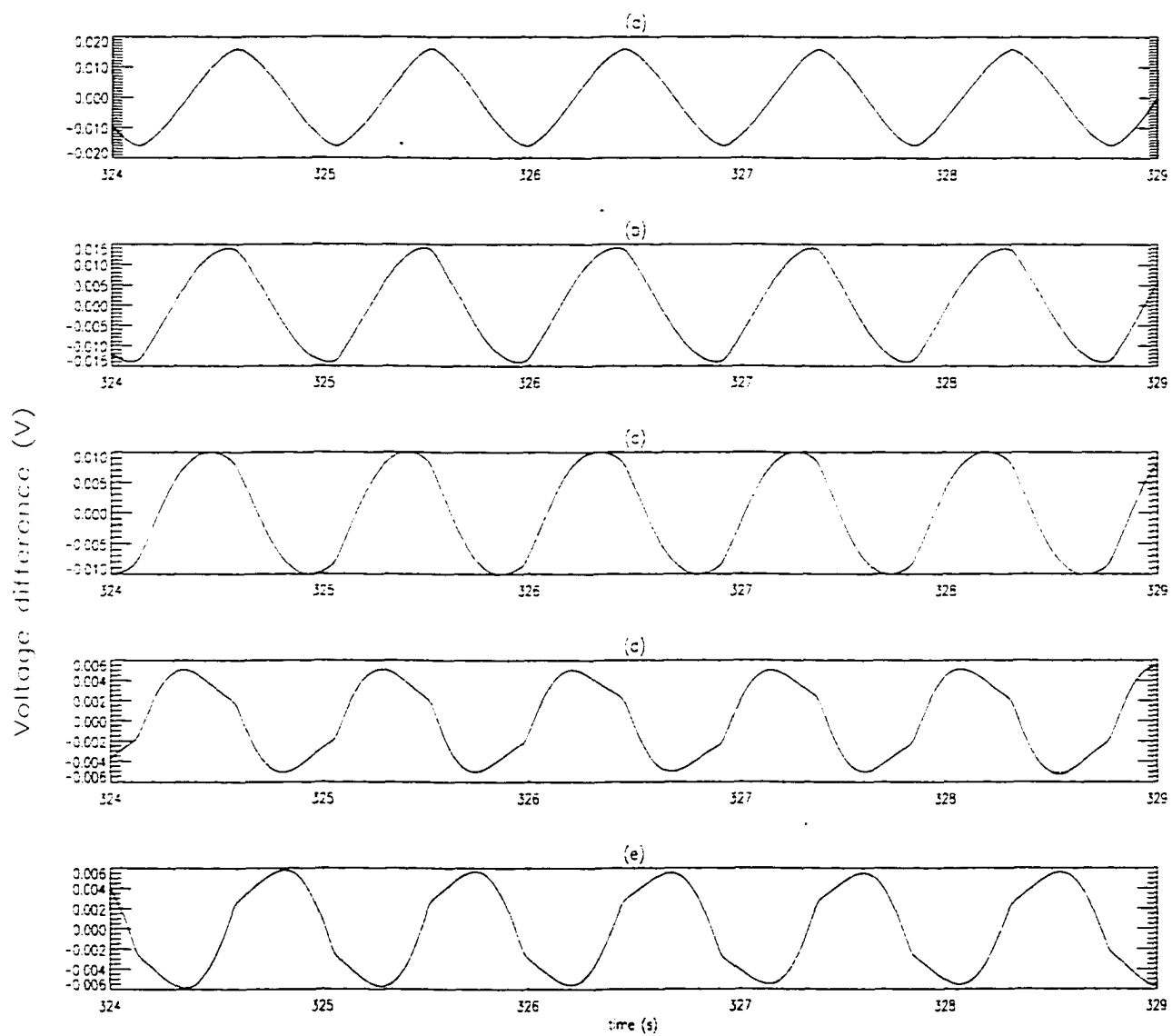


Figure B-6: Addition of shadow potential with the equal magnitude potential due to an ambient electric field with a phase of (a) 0°, (b) 45°, (c) 90°, (d) 140°, (e) 225°.

produce features such as the ones seen here. Two sine waves of arbitrary amplitude and phase can only produce another sine wave. Panel (e) is shown to demonstrate that at phase differences greater than 180° (here is shown 225°) that the mirror image of the first few signatures appear.

To see how this compares to the actual data, we present Figure B-7, which shows the raw electric field from the North payload, that has not been despun or offset in any way, as a function of flight time. Each panel spans ten seconds, to make quick comparisons with Figure B-6. Note that the y axis in Panel (c) is a factor of ten less than the previous two panels. In Panel (a), near T+382 is obvious evidence of the breaking wave feature seen in the model data. Panel (b) clearly shows the spiking on the peaks of the potential signature from T+388 to T+396. Panel (c) shows the return of a sinusoidal signature when there is no electron precipitation.

Figure B-8 shows the same time period for the East payload. There is some evidence of the breaking wave signature in Panel (a) at T+382, but no significant spiking in Panel (b). Panel (c) shows again the lack of odd features when there is no electron precipitation. Comparisons to the model show the expected difference for two payloads with different spin axis angles with respect to the magnetic field, and thus different shadow dimensions. The North payload sees significant spiking and breaking wave features, and has a greater spin axis angle with respect to \vec{B} , whereas the East payload spin axis is tipped less and sees less of the same features. The model predictions as shown in Figures B-4 and B-5 reflect these same differences between the different payloads.

However, it is important to note that when comparing Figure B-7 with Figure B-6, that Figure B-6 was generated using a model potential signature that was equal in magnitude

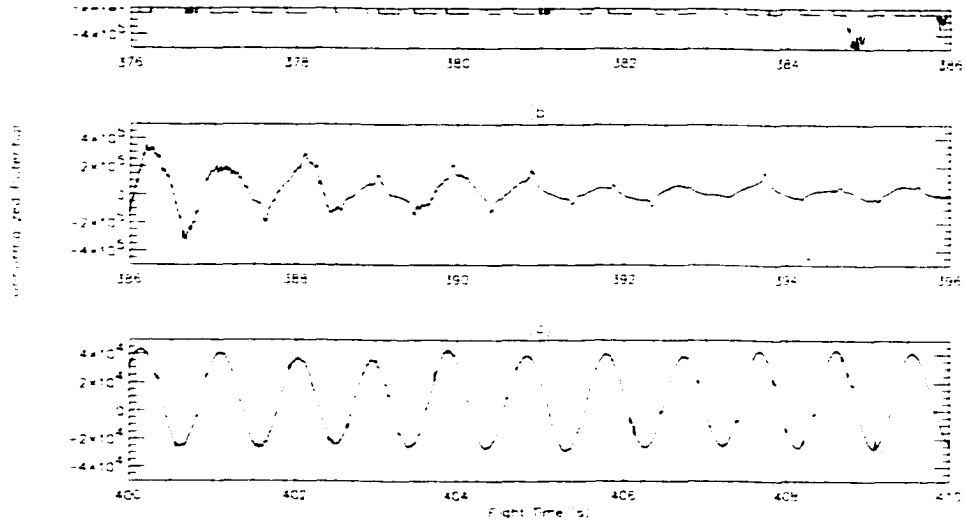


Figure B-7: Raw electric potential difference as a function of flight time for the North payload.

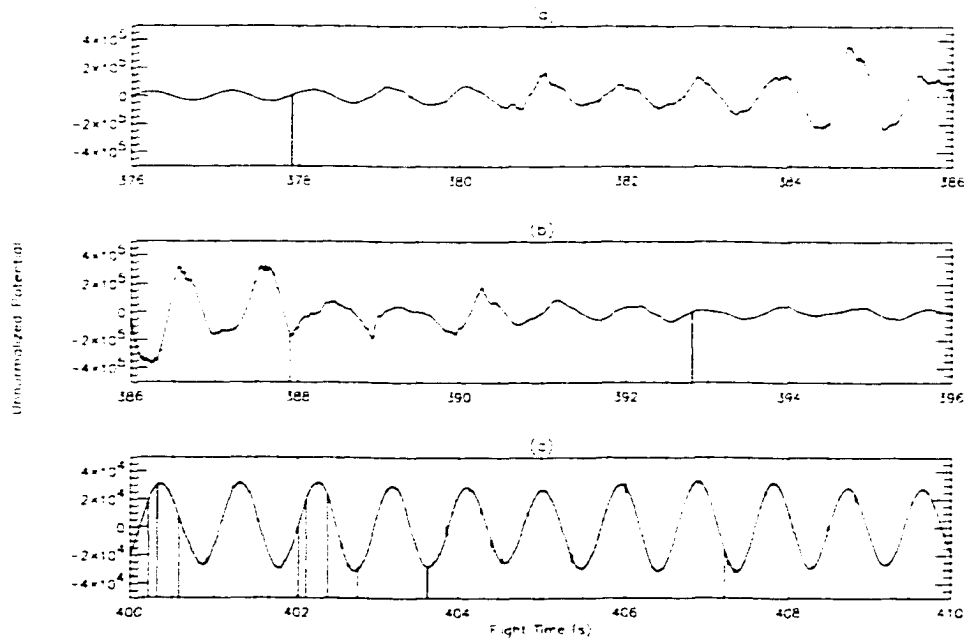


Figure B-8: Raw electric potential difference as a function of flight time for the East payload.

to the ambient electric potential. Due to the extremely high electric potentials observed in the flight, this is rarely the case. In particular, for the times shown in Panels (a) and (b) in Figure B-7, the total potential measured by the North payload is on the order of volts, whereas the model potential for the same time, based on observed particle data, is tens of millivolts.

We have shown a model of a region of positive space charge, relative to the surrounding plasma, due to the payload shadowing of an electron beam. The presence of this region, coupled with an ambient electric field, can produce odd non-sinusoidal signatures in the potential as measured by opposing electric potential spheres on the spinning payload. These features are also seen in the actual rocket data, and their relative importance and frequency on each payload is consistent with the model predictions for different payload spin axis alignment to the magnetic field. The fact that there is good qualitative agreement, but poor quantitative agreement could be a result of inaccurate Debye interpretations or the simplicity of the static, polygon shadow description. Despite that, the good qualitative agreement between the model and measured data is reason to believe the shadowing of a space region by a payload traveling through an auroral arc structure can heavily influence the measurement of potentials from that payload, and efforts such as biasing the potential spheres is necessary to obtain a more unadulterated measurement of the electric fields.

Appendix C

Number Density Calculations

C.1 Calculation of Number Density

The number density of a measured electron beam can be determined from Equation B.2.1 when considering measured particle data. However, due to the Maxwellian distribution of particles, some particles will be unaccounted for due to the upper energy limit threshold on the particle detectors. This underestimation is emphasized when the peak of the beam nears or surpasses the maximum detectable energy range. Therefore, to compute the actual number density, one must take into account the missing portions.

From *Baumjohann and Treumann (1996)*, if one considers an auroral beam, the distribution function of a Maxwellian that is streaming along the magnetic field can be given by

$$f(v_{\parallel}, v_{\perp}) = \frac{n}{T_{\perp} T_{\parallel}^{1/2}} \left(\frac{m}{2\pi k_B} \right)^{3/2} \exp\left(-\frac{mv_{\perp}^2}{2k_B T_{\perp}} - \frac{m(v_{\parallel} - v_{0\parallel})^2}{2k_B T_{\parallel}} \right) \quad (\text{C.1.1})$$

where m is the particle mass, $k_B T$ is the average thermal energy, and parallel and perpendicular are defined with respect to the magnetic field.

Using the distribution function, we easily can get the number density from

$$n = \int f(\vec{v}) d^3v \quad (\text{C.1.2})$$

by integrating over the vector components of the velocity.

We can likewise perform the integration over the parallel and perpendicular velocities

through

$$n = \int_{v_{\perp}=0}^{v_{\perp}max} \int_{v_{\parallel}=0}^{v_{\parallel}max} 2\pi v_{\perp} f(v_{\parallel}, v_{\perp}) dv_{\perp} dv_{\parallel} \quad (\text{C.1.3})$$

Here, the integral is multiplied by 2π rather than the usual 4π because the streaming beam in the parallel direction virtually guarantees, for large enough $v_{0\parallel}$, that the integral will completely cover the distribution function in dv_{\parallel} , but only will give $\frac{1}{2}$ the value in the dv_{\perp} integral due to the symmetry v_{\perp} about zero.

C.2 Estimated Densities

Since the distribution function is a function of number density, then integrating C.1.3 from zero to a maximum velocity of c should yield a value of one. However, our real detectors cannot measure particle energies from zero to 530 keV, which is roughly the energy of an electron with speed c . Since we only measure electrons from 9 eV to 14.2 keV, the lower limit of the dv integrals must be set to 1.78×10^6 , while the upper limit of the dv integral must be 7.06×10^7 m/s. Table C.1 shows the portion of the number density calculated from Equation C.1.3. The number density is the value of the integral with n divided out. A given peak beam energy has an associated $v_{0\parallel}$, and the peak beam energies chosen correspond to the energy level steps of the high voltage supplies providing potentials to the electron detector hemispheres. It is evident that as the peak in the beam approaches the energy thresholds of the detectors, the determination of n from the electron data could underestimate the number density by a factor of two or more. This is the information used to estimate the number density for the data presented herein, by inspecting the electron data and determining the peak in the beam energy. The potential values for the shadow in

Beam Peak (eV)	e ⁻ Velocity (km/s)	Portion of n	$\frac{1}{\text{measured portion}}$
23187.70	90249	0.193675	5.163
18145.66	79837	0.339322	2.947
14199.99	70625	0.492306	2.031
11112.28	62477	0.626637	1.596
8695.978	55268	0.729204	1.371
6805.068	48891	0.798142	1.253
5325.357	43250	0.837725	1.194
4167.388	38260	0.854226	1.171
3261.213	33846	0.853786	1.171
2552.080	29941	0.841618	1.188
1997.144	26486	0.821850	1.217
1562.876	23430	0.797617	1.253
1223.038	20727	0.771209	1.297
957.0948	18336	0.744234	1.344
748.9799	16220	0.717763	1.393

Table C.1: Portion of the number density measured as a function of peak beam energy for particle detectors.

different regions are then multiplied by the inverse of the portion of n calculated above to obtain the corrected value of the charge density in the shadow regions.